Modelling the black and brown carbon absorption and their radiative impact: the June 2023 intense Canadian boreal wildfires case study

Paolo Tuccella, Ludovico Di Antonio, Andrea Di Muzio, Colaiuda Valentina, Laurent Menut, Giovanni Pitari, Edoardo Raparelli

Modelling the black and brown carbon absorption and their radiative impact: the June 2023 intense Canadian boreal wildfires case study

Paolo Tuccella[1], Ludovico Di Antonio[2], Andrea Di Muzio[1], Colaiuda Valentina[3], Laurent MENUT[4], Giovanni Pitari[1], and Edoardo Raparelli[5]

[1]Università degli Studi dell'Aquila
[2]Laboratoire, Atmosphères, Observations Spatiales (LATMOS)/IPSL, Sorbonne Université, UVSQ, CNRS
[3]Abruzzo Region Civil Protection Agency
[4]Laboratoire de Meteorologie Dynamique
[5]University of L'Aquila

October 22, 2024

Abstract

Black carbon (BC) and brown carbon (BrC) are light-absorbing aerosols with significant climate impacts, but their absorption properties and direct radiative effect (DRE) remain uncertain. We simulated BC and BrC absorption during the intense Canadian boreal wildfires in June 2023 using an enhanced version of CHIMERE model. The study focused on a domain extending from North America to Eastern Europe, including a significant portion of the Arctic up to 85°N.

The enhanced model includes an updated treatment for the BC absorption enhancement and a BrC ageing scheme accounting for both browning and blanching through oxidation. When compared to observations, the updated model accurately captured aerosol optical depth (AOD) at multiple wavelengths, both near the wildfires and during transoceanic transport to Europe. Improvements were observed in the simulation of absorbing aerosol optical depth (AAOD) compared to the control model.

The all-sky regional direct radiative effect (DRE) for June 2023 attributed to the intense Canadian wildfires, was reduced from -2.1 W/m^2 in the control model to -1.9 W/m^2 (-2.0/-1.8 W/m^2, ±5%), in the enhanced model, indicating an additional warming effect of +0.2 W/m^2 (about +10%) due to advanced schemes used for the BC and BrC absorption.

The results indicate the importance of an accurate simulation of aerosol absorption in regional climate predictions, especially during large-scale biomass burning events. They also suggest that traditional models could overestimate the cooling effect of boreal wildfires, highlighting the need for improvement of aerosol parameterization to better predict the DRE and develop effective mitigation strategies.

Modelling the black and brown carbon absorption and their radiative impact: the June 2023 intense Canadian boreal wildfires case study

Paolo Tuccella[1,2], Ludovico Di Antonio[3,4], Andrea Di Muzio[1], Valentina Colaiuda[5], Laurent Menut[6], Giovanni Pitari[1], Edoardo Raparelli[1,2]

[1]Departement of Physical and Chemical Sciences, University of L'Aquila, 67010 L'Aquila, Italy.
[2]Center of Excellence in Telesensing of Environment and Model Prediction of Severe Events (CETEMPS), University of L'Aquila, Italy.
[3]Univ. Paris Est Creteil, Université Paris Cité, CNRS, LISA, F-94010 Créteil, France.
[4]Laboratoire, Atmosphères, Observations Spatiales (LATMOS)/IPSL, Sorbonne Université, UVSQ, CNRS, Paris, France
[5]Abruzzo Region Civil Protection Agency, L'Aquila, Italy.
[6]LMD/IPSL, École Polytechnique, Institut Polytechnique de Paris, ENS, PSL Research University, Sorbonne Université, CNRS, Palaiseau, France

Correspondence to Paolo Tuccella: paolo.tuccella@univaq.it

Key Points

- Enhanced modelling of black and brown carbon improved the simulation of aerosol absorption during the 2023 Canadian wildfires.
- Advanced modelling of black and brown carbon reduced the direct radiative effect of the wildfires by 10%, from -2.1 to -1.9 W/m².
- Accurate aerosol absorption representation is crucial for predicting the regional climate impact of large-scale biomass burning events.

Abstract

Black carbon (BC) and brown carbon (BrC) are light-absorbing aerosols with significant climate impacts, but their absorption properties and direct radiative effect (DRE) remain uncertain. We simulated BC and BrC absorption during the intense Canadian boreal wildfires in June 2023 using an enhanced version of CHIMERE model. The study focused on a domain extending from North America to Eastern Europe, including a significant portion of the Arctic up to 85°N.

The enhanced model includes an updated treatment for the BC absorption enhancement and a BrC ageing scheme accounting for both browning and blanching through oxidation. When compared to observations, the updated model accurately captured aerosol optical depth (AOD) at multiple wavelengths, both near the wildfires and during transoceanic transport to Europe. Improvements were observed in the simulation of absorbing aerosol optical depth (AAOD) compared to the control model.

The all-sky regional direct radiative effect (DRE) for June 2023 attributed to the intense Canadian wildfires, was reduced from -2.1 W/m² in the control model to -1.9 W/m² (-2.0/-1.8 W/m², ±5%), in the enhanced model, indicating an additional warming effect of +0.2 W/m² (about +10%) due to advanced schemes used for the BC and BrC absorption.

The results indicate the importance of an accurate simulation of aerosol absorption in regional climate predictions, especially during large-scale biomass burning events. They also suggest that traditional models could overestimate the cooling effect of boreal wildfires, highlighting the need for improvement of aerosol parameterization to better predict the DRE and develop effective mitigation strategies.

Plain Language Summary

Black carbon (BC) and brown carbon (BrC) are atmospheric particles that absorb sunlight and contribute to climate warming. BC is emitted from the incomplete combustion of fossil fuels, biomass, and biofuels, while BrC is primarily produced by wood burning. However, their exact climate impact remains uncertain. In this study, we used an improved version of the CHIMERE model to simulate BC and BrC absorption during the intense Canadian wildfires in June 2023. The model covered a vast area from North America to Eastern Europe, including parts of the Arctic.

We refined the model to more accurately calculate the BC light absorption and the BrC absorption changes over time (either increasing or decreasing). Comparing the model results with satellite and ground-based data, we found that the updated model more precisely captured the absorption spatial variability, particularly in regions affected by wildfire smoke.

The study showed that models lacking proper BC and BrC treatment may overestimate the cooling effect of wildfires. Our improved model reduced the estimated cooling from the 2023 Canadian wildfires by about 10%, emphasizing the importance of accurate modelling to predict the climate impacts of these increasingly frequent events driven by global warming.

1 Introduction

Black carbon (BC) and brown carbon (BrC) are recognized by the scientific community as light-absorbing aerosol particles influencing the climate through the direct (Haywood and Boucher, 2000) and semidirect (Hansen et al., 1997) effects, by darkening the surface after their deposition on the snow/ice pack (Flanner et al., 2007; Bond et al., 2013, Lin et al., 2014; Tuccella et al., 2021; Brown et al., 2022), and acting as cloud condensation nuclei for clouds they may modify the cloud optical properties and precipitation pattern through the indirect aerosol effects (Andreae et al., 2008). The effects of BC and BrC on the global and regional climate are uncertain (IPCC, 2021).

BC is formed through the incomplete combustion of fossil fuels (FF), biomass (BB), and biofuels (BF) (Bond et al., 2013). Soot particles exhibit a strong capacity to absorb incoming solar radiation (Bond et al., 2013). Current estimates suggest BC as the third most important contributor to global warming after carbon dioxide (CO_2) and methane (CH_4) (Bond et al., 2013; Gustafsson and Ramanathan, 2016; IPCC, 2021).

BC absorption is influenced by its mixing state (Curci et al., 2019; Tuccella et al., 2020). Mixing state refers to the distribution of chemical and physical properties within an aerosol population (Riemer et al., 2019). In an externally mixed state, different aerosol components exist as separate particles with distinct compositions. Conversely, internally mixed particles within an aerosol population consist of a homogeneous mixture of chemical species. In the real atmosphere, purely internal or external mixing states are not common (Bondy et al., 2018) and the mixing state continuously evolves due to processes governing the aerosol lifecycle. Freshly emitted BC particles usually have a fractal structure and are externally mixed with non-BC species. After emission, ageing processes lead to the formation of internally mixed particles, characterized by a core-shell structure where the BC core is coated by a shell composed of organic and inorganic compounds. The presence of the shell increases amplifies the BC absorption through the so called “lensing effect” (Jacobson, 2000, 2001; Lesins et al., 2002).

The absorption enhancement (E_{abs}) of coated BC is typically calculated with a Mie code for the core-shell structure (e.g., Toon and Ackerman, 1981). Several studies have demonstrated that this model is an oversimplification, since it does not consider the complex morphology of BC particles, with implications for absorption calculation (Adachi et al., 2010; Wang et al., 2021; Romshoo et al., 2022). In particular, the core-shell model overestimates the BC absorption enhancement (Adachi et al., 2010; Liu et al., 2017; Fierce et al., 2020; Wang et al., 2023). While some studies have observed a substantial increase in light absorption, others have reported a considerably lower E_{abs} compared to laboratory and modeling simulations (Cappa et al., 2012; Lack et al., 2012; Liu et al., 2017). Liu et al. (2017) demonstrated that E_{abs} is influenced by the mass ratio of non-BC to BC. Specifically, BC emitted from urban traffic, characterized by lower non-BC to BC mass ratios, is often better represented as externally mixed with no absorption enhancement. Moreover, the discrepancies of between observed and modelled differences have been also attributed to the particle-to-particle heterogeneity in the environment (Fierce et al., 2020; Zhao et al., 2021; Zeng et al., 2024). This highlights the importance of incorporating mixing state-dependent absorption parameterizations in atmospheric models to accurately predict the radiative effects of BC.

Brown carbon (BrC) is defined as the subset of organic aerosol that exhibits strong absorption (OA) (Andreae et al., 2006; Laskin et al., 2015) of shortwave radiation with wavelengths less than 400 nm (Lukacs et al., 2007; Alexander et al., 2008; Chen et al., 2010; Arola et al., 2011; Kirchstetter et al., 2012, Moise et al. 2015). BrC is mainly produced by BF combustion, BB, and ageing of secondary organic aerosol (SOA) (Bones et al., 2010; Hecobian et al., 2010; Arola et al., 2011; Updyke et al., 2012; Lambe et al., 2013; Lee et al., 2014; Laskin et al., 2015; Guang et al., 2016), while other sources are related to cloud chemistry (Zhang et al., 2017). The representation of OA optical properties in climate models has evolved over the past decade. From being considered as scattering particles, the BrC absorption is now included in many global (Wang et al., 2014; Lin et al., 2014; Saleh et al., 2015; Jo et al., 2016; Wang et al., 2018; Brown et al., 2018; Tuccella et al., 2020, 2021; Zhang et al., 2020; Drugé et al., 2022; DeLessio et al., 2024) and regional modelling studies (Methymaki et al., 2023; Kononalov et al., 2024).

Primary BrC absorption is not constant over time but varies with ageing processes that OA undergoes. Experimental results have suggested that BrC optical properties may be modified through aqueous-phase photochemical reactions, potentially leading to both photo-enhancement and photobleaching (Zhao et al., 2015). The increase of BrC absorption is called "browning" and it is primarily driven by heterogeneous oxidation reactions with hydroxyl (OH) and nitrate (NO_3) radicals, as well as aqueous oxidation (Cheng et al., 2020; Schnitzler et al., 2020; Hems et al., 2020). Following browning, BrC undergoes bleaching, a process attributed to oxidation by OH and ozone (O_3) (Hems et al., 2021).

While photobleaching is frequently incorporated into models simulating brown carbon (Wang et al., 2018; Brown et al., 2018; Zhang et al., 2020; Drugé et al., 2022), browning is often overlooked. To our knowledge, only DeLessio et al. (2024) have accounted for photo-enhancement in their study. The same authors concluded that accurate representation of the diurnal variability in OA absorption necessitates the inclusion of the browning process in the atmospheric models.

Many studies have demonstrated that wildfires impact the climate system (Randerson et al., 2006; Li et al., 2017; Walker et al., 2018; Eckdahl et al., 2022; Linares and Ni-Meister, 2024). At the same time, the frequency of wildfire events is increasing due to climate warming. The relationship between climate change and wildfire frequency has been studied since the early 1990s (van Bellen et al., 2010). The Arctic is warming at more than twice the global average rate (Meredith et al., 2019), which contributes to the rise of wildfire activity in boreal regions of Alaska and western Canada (Gillett, 2004; Veraverbeke et al., 2017). Moreover, the Northern Hemisphere has experienced extreme wildfire seasons, as for example the 2023 Canadian events (Byrne et al., 2024), leading to significant aerosol emissions, with notable impacts on aerosol properties even in Europe (Filonchyk and Peterson, 2024). Additionally, in the future, anthropogenic aerosol mitigation could be a significant driver in enhancing boreal forest fires (Allen et al., 2024).

Boreal forest fires are important sources of BC and OA, which may exert significant regional climate feedback at regional scale (Konovalov et al., 2024a; 2024b). Accurate prediction of BC and OA absorption properties is essential for estimating the climatic impact of boreal wildfires.

This study provides a comprehensive assessment of BC and BrC absorption during the 2023 Canadian boreal wildfires using an enhanced parametrisation within the CHIMERE model. The results underscore the critical role of aerosol absorption modelling for an accurate prediction of the regional

direct radiative effect (DRE), associated to large-scale wildfire events. In Section 2, we detailed the model description and setup, where we included a treatment for improving the BC absorption and a treatment for BrC absorption, including an update parameterization for BC E_{abs} and a treatment for BrC absorption, accounting for both browning and blanching processes. In Section 3, the simulated optical properties have been evaluated against satellite and ground-based observations. Finally, in Section 4, we discussed the DRE of the June 2023 Canadian smoke aerosol.

2 Methods

2.1 CHIMERE model description and setup

In this study, we have used the 2021 version of the CHIMERE model (Menut et al., 2021) to simulate the absorption of BC and BrC, coupled online with the meteorological Weather Research and Forecasting (WRF) model. This online configuration is capable to simulate both direct (Briant et al., 2017) and indirect aerosol effects (Tuccella et al., 2019). The WRF model is a mesoscale meteorological model including several parameterizations for atmospheric processes (https://www.mmm.ucar.edu/models/wrf, last access: 09 October 2024). CHIMERE is a chemical and transport model suitable for studies ranging from hemispheric to urban scales (Mailler et al., 2017). It contains multiple numerical schemes for simulating the gas-phase and aerosol processes. WRF and CHIMERE are coupled with the external coupler OASIS3-MCT (Craig et al., 2017). The information between models is exchanged with a regular frequency defined by the user (Briant et al., 2017).

We simulated the entire month of June 2023, after a one-month of spin-up for chemistry. WRF-CHIMERE was configured on the domain shown in Figure 1. This domains spans from North America to Eastern Europe, in latitude it extends from Tropics up to North Pole. The horizontal resolution was of 78 km, with 190 x 127 grid points. We used 33 vertical levels extending from surface up to 50 hPa for WRF, and 30 levels up to 200 hPa for CHIMERE. The coupling time (i.e., exchange frequency) between WRF and CHIMERE was fixed at 20 minutes.

Main parameterizations adopted for WRF are the YSU for planetary boundary layer (Hong et al.,2006), NOAH as land surface model (Chen and Dudhia, 2001), RRTMG for shortwave and longwave radiation (Iacono et al., 2008), Thompson for cloud microphysics (Thompson et al., 2008), and Grell-Freitas scheme for cumulus convection (Grell and Freitas, 2014). In CHIMERE, gas-phase reactions were calculated with the MELCHIOR2 model (Derognat et al., 2003), which includes 40 gaseous species and 120 photochemical reactions. Photolytic rates were parameterized with the FAST-JX model (Wild et al., 2000), as detailed in Mailler et al. (2016, 2017). Aerosol treatment is based on a sectional approach (Bessagnet et al., 2008; Mailler et al., 2017). Herein, we have used 10 dimensional bins ranging from 0.01 up to 40 µm. Aerosol model includes the main inorganic species (sulphate, nitrate, ammonium), water, black carbon, primary organic matter (OM), unspeciated particles, secondary organic aerosols (SOA), sea salt, and soil dust. We simulated anthropogenic and biogenic SOA with a single-step oxidation scheme, according to Bessagnet et al. (2008). Thermodynamic equilibrium of inorganic aerosols was simulated by using the ISORROPIA model (Nenen, 1998). Dry deposition of gases and aerosols were calculated with the schemes proposed by Wesely (1989) and Zhang et al. (2001), respectively. Wet deposition calculation followed the methods of Wang et al. (2014), as detailed in Mailler et al. (2017).

Aerosol optical properties in CHIMERE are calculated under the assumption of external mixing state, as outlined in Mailler et al. (2017), at 200, 400, 600, and 999 nm. Extinction efficiency, single scattering albedo (SSA), and asymmetry parameter are initially determined for each aerosol particles across each dimensional bin, and then are summed. These optical parameters are calculated assuming the aerosol particles as spherical using the Mie theory (Mie, 1908), solved through the spher.f code (Mischenko et al., 2002). Most of the aerosol complex refractive indices adopted in CHIMERE are based

on the ADIENT project (Mailler et al., 2016), with exception of BrC and BC. These latter are discussed in Section 2.2 and 2.3.

Anthropogenic emissions of trace gases and particles were taken from global inventory CAMS (Soulie et al., 2024) for the year 2022. Biomass burning emission fluxes were obtained from the CAMS dataset as described by Kaiser et al. (2012). Both inventories are at horizontal resolution of 0.1° x 0.1° and were re-gridded onto model grid according to Menut et al. (2021). Forest fire emissions from CAMS relative to June 2023 are displayed in Figure 2. Vertical injection profile of fire emissions adopted in CHIMERE is described in Menut et al. (2018). The injection height is calculated as in Sofiev et al. (2012) and corrected according to Veira et al. (2015), in case of huge fire. After the estimation of injection height, the shape of injection profile was calculated with the so called $2K_z$-like shape, where the emissions profile presents two maxima, one close to surface and one around injection height. Soil dust emissions were computed by using the scheme developed by Alfaro and Gomes (2001), with optimizations introduced by Menut et al. (2005). Sea salt emissions were estimated in accordance with Monahan (1986). NO_x emissions by lightning were included using the scheme of Price and Rind (1993), as detailed by Menut et al. (2020). Biogenic emissions were considered in our simulations employing the MEGAN model (Guenther et al., 2012).

Initial and boundary conditions for WRF were obtained from 6-hourly NCEP operational analyses at resolution a of 1° x 1°. Grid nudging toward NCEP analysis data of wind, temperature, and water vapor was applied in WRF on the model vertical levels above the planetary boundary layer. Sea ice extent and sea surface temperature were taken from NCEP data and were updated every six hours. CHIMERE was driven by the boundary conditions derived from the 2010-2017 gas and aerosol climatology based on the LMDZ-INCA global model (Folberth et al., 2006).

2.2 BC treatment

Within CHIMERE, the aerosol optical properties are calculated assuming an external mixing approach, which does not account for the BC absorption enhancement due to the lensing effect associated with the core-shell morphology of coated BC. Consequently, we have implemented within CHIMERE a scheme to account for this effect, drawing on the work of Liu et al. (2017). The authors demonstrated that E_{abs} depends on the mass ratio (M_r) of BC, given by ratio between the mass of non-BC aerosols and mass of soot particles. When $M_r<1$, BC is external mixed and absorption enhancement is not observed ($E_{abs}=1$), whereas for $M_r>3$, BC is internally mixed, and absorption is correctly calculated by core-shell model. When M_r is between 1 and 3, BC a transitional regime is observed, being neither external nor internal mixed. Therefore, for small M_r typical of fresh traffic sources (less than 1.5), E_{abs} is small (Schwarz et al., 2008). In fact, an E_{abs} of 1.1 has been reported in urban regions of California (Cappa et al., 2012) and China (Lan et al., 2013). When M_r is larger (greater than 3), as for example in biomass burning emissions, E_{abs} is in the range of 1.3-1.9 (Lack et al., 2012; Rathod et al., 2021; Kompalli et al., 2023).

Therefore, E_{abs} has been parameterized with a hybrid optical model, where no E_{abs} occurs when $M_r<1$ and is linearly interpolated to the upper threshold of $M_r=3$, where E_{abs} is accurately predicted by core-shell model (Liu et al., 2017):

$$E_{abs} = E_{abs_{cs}} F_{in} + (1 - F_{in})$$

$$F_{in} = 0.57 M_r - 074 \quad \text{for} \quad 1 < M_r < 3$$

where $E_{abs_{cs}}$ is the absorption enhancement calculated by core-shell model and F_{in} is the internally mixed fraction of BC. F_{in} is equal to 0 for M_r<1 and 1 for M_r>3. $E_{abs_{cs}}$ should be estimated with a core-shell algorithm; however, in this study, we used a constant value of 1.5. We have chosen this value because it is representative of the mean of E_{abs} estimations (Kong et al., 2024), which coincides with the average value recommended by Bond and Bergstrom (2006). It should be noted that the 90% confidence interval of E_{abs} distribution function reported by Kong et al. (2024) ranges from 1.15 (5%) to 2.18 (95%). This highlights that BC absorption simulation may depend on the value of $E_{abs_{cs}}$adopted. Finally, the refractive index assigned to BC was 1.95–0.79i, as recommended by Bond and Bergstrom (2006).

2.3 BrC treatment

The CHIMERE model treats OM as a scattering aerosol particle. Therefore, we have implemented a scheme to consider the BrC absorption within CHIMERE simulations. To our knowledge, currently there are not emission inventories of BrC. Previously, different methods have been employed to estimate the primary BrC emissions. For example, Jo et al. (2016) derived BrC emissions fluxes using a relationship between the modified combustion efficiency and absorbing Ångström exponent. Other studies, such as Feng et al. (2013) and Wang et al. (2014), have assumed that a fraction of emitted OA was BrC. Additionally, emissions have been also inferred from BC-to-OA ratio (Park et al., 2010; Saleh et al., 2015; Zhang et al., 2020). Alternatively, other researchers have treated all OA as radiation-absorbing particles, assigning to them specific optical properties (Wang et al., 2018). In our investigation, we have used this latter approach, as detailed below.

BB-BrC emissions were taken directly from BB-CAMS inventory (see Section 2.1). By contrast, BF-BrC anthropogenic emissions have been estimated from emission fluxes from domestic, industrial, waste management, and agricultural sectors. Specifically, a fraction of these emissions was considered as absorbing OA. This portion was derived based on the ratio of BF emissions to the total anthropogenic (FF+BF) OA emissions, as reported in the inventory of Bond et al. (2007), and then applied to OM emissions from CAMS, after being treated as described in Section 2.1.

In this investigation, we utilized the BrC optical properties as suggested by Wang et al. (2018), which were obtained constraining the MAC of biomass burning BrC with measurements from aircraft campaigns conducted in the continental United States. Additionally, the same authors demonstrated that their optical properties were applicable to reproduce the BB-BrC absorption observed over Europe. Consequently, we have adopted the MAC values from Wang et al. (2018), since our study is focusing on North America and Europe. Additionally, in our prior investigations, we were able to calculate BrC absorption at global scale in the atmosphere (Tuccella et al., 2020) and within snow (Tuccella et al., 2021),

using this set of optical properties. MACs at 365, 440, and 550 nm were 1.19, 0.76, and 0.39 m2/g for BF-BrC, and 1.33, 0.77, and 0.35 m2/g for freshly emitted BB-BrC, respectively.

Photochemical ageing of BB-OA is crucial in simulating BrC absorption, since it induces blanching of BrC through photochemistry processes. Several methodologies have been adopted to simulate the BB-BrC ageing. One of these consists in the passage from hydrophobic to hydrophilic, with hydrophilic component exhibiting a lower absorption compared to its hydrophobic counterpart (e.g., Tuccella et al., 2020; Zhang et al., 2020; Brugé et al., 2022). The transition is usually done with a characteristic time scale. Alternatively, some studies have adopted a blanching scheme wherein the absorption was tracked and attenuated based on OH concentration and a characteristic half-life time scale (Wang et al., 2018; Brown et al., 2018). However, the most recent advancement in BB-BrC ageing modelling has been introduced by DeLessio et al. (2024). This consists in considering the heterogeneous oxidation of BB-BrC by hydroxyl radical (OH), nitrate radical (NO3), and ozone (O3), according to the results of Hems et al. (2021). This innovative approach has been adopted and integrated in our investigation.

Specifically, following DeLessio et al. (2024), the ageing processes was divided in two distinct steps. In the first, freshly emitted BB-BrC undergoes an absorption enhancement, a phenomenon known as “browning”. In the second phase, the “browner” BrC is subjected to blanching process, during which the absorption is lower than that of freshly emitted BrC. Transfer mass from freshly emitted BrC to more absorbing BrC is succeeded by whitening, involving mass transfer from browner to less absorbing BrC. The mass transfer was quantified with second order rate constant for each reaction of BB-BrC with OH, NO3, and O3. During the nighttime, freshly emitted BB-BrC is oxidized by NO3 to form more absorbing OA, which then becomes less absorbing through subsequent oxidation with O3. During daylight hours, freshly BB-BrC is oxidized by OH to form more absorbing brown carbon. This browner BrC is then blanched through oxidation with OH and O3. Rate constants used were the same of DeLessio et al. (2024), derived from the initial first reaction rate for BrC processing defined by Hems et al. (2021), with oxidant concentrations assumed by same authors.

The MACs at 365, 440, and 550 nm of less absorbing BB-BrC were set at 0.37, 0.23, and 0.10 m2/g, respectively (Wang et al., 2018). These values reflect the average absorption of biomass burning BrC and are recommended for applications in models where absorption is not tracked. They should be used to account for absorption reduction when the whitening is not explicitly simulated (Wang et al., 2018). We note that the MACs adopted for less absorbing BB-BrC were slightly less 30% of those of freshly emitted OA. However, this value is very close to the minimum threshold of ¼, imposed by the same authors (Wang et al., 2018), below which the absorption may not drop, when it is tracked to account for BrC blanching. In addition, this value is also close to threshold of 20% based on laboratory studies (Fleming et al., 2020; Hems et al., 2021). As in DeLessio et al. (2024), we assigned to browner biomass burning BrC a MAC that is 150% larger of that attributed to freshly emitted OA.

In this work, we have also assumed that both biogenic and anthropogenic SOA are absorbing. We attributed to SOA-BrC the same set of optical properties of Wang et al. (2014), that for a typical size distribution of organic aerosols result in a MAC of 0.3 m^2/g at 440 nm.

The approach for implementing the BrC in CHIMERE illustrated above presents some limitations. These are related to ageing processes that were missed in our implementation. First, our model does not account for the blanching effect due to in-cloud water processing, which should reduce the browner BrC lifetime of about 3 hours (Hems et al., 2021). Second, we have not included in the model the blanching that SOA-BrC could undergo with ageing (Lee et al., 2014; Liu et al., 2016; Kasthuriarachchi et al., 2020). Another source of uncertain is the absorption attributed to the browner BB-BrC, which was assumed to be 150% higher than that of fresh emitted BrC. It should be noted that this value represents the middle range of the values observed in laboratory studies (Zhong and Jang, 2014; Hems et al., 2021). Therefore, this assumption could affect the BrC absorption close to BB sources, where browner BrC is present. Additionally, we have assigned to SOA-BrC compounds the same value for the imaginary part of the refractive index. In fact, the absorption of secondary BrC could be dependent on the specific SOA species. For example, the absorption of SOAs formed from photochemical oxidation of toluene appears to strongly depend on initial NO_x concentration (Lin et al., 2015, Liu et al., 2015, Moise et al., 2015, Dingle et al., 2019).

2.4 Numerical simulations

We performed a series of model simulation to evaluate the model development described above. The list of our runs is reported in Table 1. The first simulation has been conducted with the default version of CHIMERE, which does not include the BC absorption enhancement and BrC effects. This reference simulation (control, CTRL) was used to evaluate the aerosol transport and basic skill of the model in reproducing the AOD distribution.

The second simulation included only the scheme for BC_{Eabs} and was aimed to evaluate how this parameterization improves the aerosol absorption simulation in CHIMERE (BC_{Eabs}). The third run was takes into account both black carbon E_{abs} and BrC absorption. This simulation was labelled as "BEST" as it includes all the parameterizations introduced to enhance CHIMERE and because it represents a central estimate of absorption compared to the perturbed runs described below.

Other two simulations have been conducted to estimate the sensitivity of BC and BrC absorption to aerosol optical properties uncertainties. Consequently, we created a high absorption scenario (H-ABS) and a low absorption scenario (L-ABS), perturbing the BEST run. In the first case, we have not considered the BB-BrC ageing assigning it the MAC of freshly emitted BB-OA. Furthermore, $E_{abs_{cs}}$ was set to 1.9, representing the 90th percentile of E_{abs} distribution (Kong et al., 2024). By contrast, in the L-ABS scenario, we assigned to BB-BrC the MAC of blanched OA and $E_{abs_{cs}}$ was set to the 10th percentile of E_{abs} distribution reported in Kong et al. (2024), which is equal to 1.2. Consequently, by considering these two extreme cases of absorption, we have evaluated the range error in simulating the carbonaceous aerosols absorption, associated to uncertainties of BC absorption enhancement and BrC ageing parameterizations.

All simulations were conducted without the direct and indirect aerosol effects, since they may introduce feedback mechanisms that could influence atmospheric dynamics and subsequently affect the evaluation of model updates. Furthermore, the primary objective of this study is to assess the direct radiative effect of the 2023 Canadian wildfire episode and to investigate the implications of model

development on its estimation. The activation of direct and indirect effects could further alter the radiation budget through modifications in cloud coverage and properties. However, this is a subject that deserves future investigation.

2.5 Evaluation strategy

Numerical simulations have been compared with aerosol optical properties retrieved from ground-based and satellite instruments. Before the comparison, the CHIMERE output was regridded onto a regular grid with a horizontal resolution of 0.7° x 0.7°. The regular domain is presented in Figure 3.

Ground-based observations were taken from the version 3 of Aerosol Robotic Network (AERONET) Sun photometers (Holben et al., 2001; Sinyuk et al., 2020). AERONET is a global network providing observations of spectral columnar aerosol optical properties, such as AOD, AAOD, and single scattering albedo (SSA), at 440, 675, 870, and 1020 nm. AERONET disseminates data according to different quality check criteria: the cloud-screened L1.5, and cloud-screened and quality-assured L2.0 (Dubovik et al., 2002). In the latter, SSA is provided only when AOD levels at 440 nm exceeds 0.4. Consequently, only 18% of L2.0 data available in June 2023 was AAOD. Thus, following the methodology used in our previous studies (Curci et al., 2019; Tuccella et al., 2020), based on the work of Wang et al. (2016), we have complemented the L2 AAOD data with the L1.5.

Figure 3 displays the AERONET sites available during our study period, along with the fraction of AOD data coverage for each site. For our analysis, we included only the stations with at least 75% of data availability. Figure 3 also illustrates the average AOD at 440 nm measured at these sites during June 2023. Based on these AOD values, we identified three regions that were most interested by Canadian forest fires, which are outlined with blue rectangles in Figure 3. The first region (R1) included the AERONET stations located in Canada, representative of the measurement sites directly affected by the boreal fire sources. The second region (R2) covered the Western USA, where the observation stations were affected by smoke transported downwind the fire sources. Finally, the third region (R3) was represented by Western Europe, where AERONET sun photometers were subjected to transoceanic transport of Canadian boreal wildfire aerosols. In these three regions, we conducted a thorough and detailed analysis of the model performances. The AERONET stations used for AAOD evaluation are also displayed in Figure 3. In our analysis, we included only the stations with at least 55% of data availability, due to the reduced availability of AAOD data compared to AOD.

The simulated monthly spatial AOD pattern at 550 nm was compared with the Moderate Resolution Imaging Spectroradiometer (MODIS) AQUA data (Levy et al. 2015). In this work, we used the “AOD_550_Dark_Target_Deep_Blue_Combined” merged product from the “MYD04_L2” Level 2 (at 10 km spatial resolution at nadir), which combines the Deep Blue (Hsu et al., 2004) and Dark Target (Remer et al., 2005; 2020) MODIS algorithms, to disseminate the AOD global coverage. This merged product provides only high quality-assured (QA) pixels. The QA flag in the MODIS product is defined as an integer number, which in the selected combined AOD product is represented by:

- QA>3 over land and QA>0 over ocean for the Dark Target
- QA 2 and 3 for the Deep Blue

The MODIS satellite data were resampled at the spatial resolution to match the spatial resolution of the CHIMERE regular grid. For each grid cell, observed AOD was calculated as a weighted average, considering the quality-assurance flags from the MODIS retrievals. A minimum threshold of 30% of data with a QA score greater than 3 was required for each regridded pixel. The same approach was applied to average the satellite overpass times, extracting the nearest hour to align with the numerical simulation.

The simulated monthly spatial AOD and AAOD patterns at 354 nm were also compared with the Ozone Monitoring Instrument (OMI) Aura Near UV OMAERUV satellite product. Despite the coarse spatial resolution of 13x24 km^2 of the OMI satellite footprint, the OMAERUV algorithm provides aerosol spectral optical properties at 354 and 388 nm (Torres et al., 2007; 2013).

To compare the CHIMERE simulations with OMI data, only quality-assured data (i.e., quality flag = 0) were used, considering pixels with a solar zenith angle <70° and non-missing UV aerosol index values. The OMI satellite data were further resampled to match the spatial resolution of the CHIMERE regular grid. For each grid cell, the AOD/AAOD values were calculated as the average of all satellite pixels falling within the simulation grid.

Model accuracy in reproducing observations was evaluated using a set of statistical indices. These included the Pearson correlation coefficient, normalized mean bias (NMB), root mean square error (RMSE), Nash-Sutcliffe efficiency (NSE), Taylor score (TS), and standard deviation error (STDE). Definitions and explanations of these indices are reported in Section S1 of the Supplementary Material.

3 Model evaluation

3.1 Aerosol optical depth simulation

In this section, we assessed the model performance of the reference run (CTRL) in reproducing the AOD, since it is a key indicator of model skill in reproducing aerosol load, which in turn depends on different processes, such as emission, transport and deposition. Statistical indices obtained from the model comparison with observed AOD are reported in Table 2.

Figure 4 shows the comparison between monthly average of AOD at 550 nm predicted and observed from the MODIS satellite. CHIMERE satisfactorily reproduced the AOD patterns. In particular, the model captured the southeastern aerosol transport, downwind of the Canadian wildfires, toward East Coast of North America and the subsequent outflow on the Atlantic Ocean. The model successfully captured the eastward long-range transport across the ocean and the plume advection over Western Europe. However, the simulated AOD is generally underestimated compared to satellite observations. A more quantitative comparison indicates that CHIMERE reproduced the MODIS monthly data with a correlation of 0.77, an average NMB of –14%, NSE of 0.57, and TS of 0.79.

Figure 5 displays the comparison between monthly average AOD at 354 nm predicted by CHIMERE and observed by OMI. CHIMERE captured the AOD distribution retrieved by satellite, especially in Canada close to the boreal fire, Eastern North America, and Atlantic Ocean. The estimated correlation coefficient was 0.65, while the AOD was underpredicted by 30%. A closer inspection to Figure 5 reveals that this bias originates in Western USA, where the model underestimates the observations by a factor of 3-4. In general, the CHIMERE performance in reproducing OMI AOD appeared poorer compared to MODIS. The possible reason of this bias will be discussed later.

The comparison of the simulated daily AOD at 440 nm compared to the AERONET at all sites showed a NMB of -24%, while the correlation, NSE and TS were 0.55 and 0.88. Figure 6 depicts the comparison of modelled and observed daily averaged time series of AOD at 440 nm at the R1, R2, and R3 regions. Additionally, the figure also reports the scatter plots between predicted and observed daily AOD values. The model captured the mean daily observed AOD behaviour in R1, R2, and R3. The CHIMERE model was able to reproduce the AOD main peaks at the Canadian AERONET sites (R1) in the first half of June, although it did not accurately capture the peaks on June 23 and 25-26. At the same time, the peaks of early, mid, and end June on eastern USA downwind from Canadian sources (R2) were captured, as well as the late June peak on western Europe (R3) due to the long-range smoke transport from North America.

Furthermore, the correlation coefficient and TS exceeded 0.70 and 0.80 for all three regions, respectively. The NMB was about -20% in R2 and R3, while in R1, it was -35%. The largest bias in R1 could be mainly attributed to the model resolution used in this study that could affect the right position of the wildfire sources. The largest bias in R1 could be mainly attributed to the model resolution deployed in this study that could impact the right position of the wildfire sources. However, it should be noted that even at higher resolution, small errors in simulated wind speed and direction may significantly impact the plume position prediction downwind of the sources (Tuccella et al., 2017). Additionally, the assessment

of model performance in R1 may be affected by the limited number (see Figure 3) of AERONET stations available in this region.

The same analysis has been conducted for the comparison of modelled AOD at 675 nm with AERONET measurements. Figure S1 shows the daily averaged times series and daily scatter plots of predicted versus observed AOD at this wavelength. The statistical indices obtained from this comparison are presented in Table S1. At this wavelength, CHIMERE simulated the average time series of AOD in a similar way as well as discussed at 440 nm. The correlation coefficient with observed daily values was 0.78, 0.73 and 0.70 in R1, R2, and R3, respectively.

In summary, the outcomes of the statistical analysis obtained from the comparison of the simulated AOD with the AERONET and satellite data are comparable to that of current regional atmospheric models (Curci et al., 2015; Palacios-Peña et al., 2019). Overall, our model exhibited an underestimation of AOD, which was quantifiable in average between 15-30%. This bias has been found in other studies conducted with CHIMERE, even with finer resolutions with respect to the one used in this study (e.g., Menut et al., 2023). Several factors may contribute to a potential bias in the simulated AOD, among those the assumption on particle mixing state (Curci et al., 2015), the simulated aerosol size distribution (Esteve et al., 2014) and the aerosol chemical composition as well as the adopted schemes to represent the organic aerosol fraction (Balzarini et al., 2015). Regarding the dependency on the chemical composition, Konovalov et al. (2023) showed that the parameterization for the secondary organic aerosols used in this study tends to underestimate the SOA mass during wildfire episodes, with consequent bias on the aerosol load. This aspect could be improved by using more realistic SOA schemes available in CHIMERE (such as the Volatility Set Basis scheme), but these are computational expensive for the aim of this investigation, since they would have required many additional variables resulting from the splitting of primary OA sources for BrC simulation. Another important source of bias in this study is the uncertainty of BB emission inventories. Aerosol simulations and their climatic impact are sensitive to specific BB emission inventory (Liu et al., 2018; Ramnarine et al., 2019; Carter et al., 2020). This uncertainty may be larger at high latitudes, where the fire sources in this study are located, due to the increased cloud cover in these regions, which may decrease the accuracy of BB emission estimates (Hua et al., 2024).

Additionally, in this discussion, it is essential to consider the uncertainties in the AOD measurements, especially the error associated with satellite data. AERONET has an uncertainty of 0.01-0.02 (Holben et al., 2001), while the error of MODIS is $0.05 \pm 0.20 \cdot \mathrm{AOD}$ and $0.03 \pm 0.05 \cdot \mathrm{AOD}$ over land and ocean, respectively (Tanré et al., 1997; Kaufman et al., 1997). The average error expected in OMI AOD is of the order of 30% (Torres et al., 2002). We compared AOD retrieved by MODIS and OMI with AERONET data. The comparison of MODIS AOD is shown in Figure S2. The analysis indicates that MODIS tends to overestimate AOD at AERONET stations, with a monthly average bias of 18%. Figure S3 shows the comparison of OMI AOD with AERONET data, revealing that OMI overestimates AOD by 40%. This bias is particularly evident in the western United States, where we identified the most substantial discrepancies between CHIMERE and OMI data.

3.2 Aerosol absorption simulation

In this section, we evaluated the performance of the new absorption scheme implemented within the CHIMERE model and detailed in Sections 2.2 and 2.3. Indeed, we compared the simulated AAOD for the reference simulation (CTRL), the BC_{Eabs}, and the BEST simulations with the OMI and AERONET AAOD data.

Figure 7 shows the monthly average of AAOD at 354 nm for June 2023, as observed by OMI and predicted by the CHIMERE in the CTRL run, BC_{Eabs}, and BEST simulations. The statistical indices derived from this comparison are reported in Table 3. The correlation coefficient for all the three simulations ranged between 0.50 and 0.54. However, the default model (CTRL), which assumes an external mixing state, failed to reproduce the AAOD observed pattern, exhibiting a bias of -78%. The increase in absorption due to BC_{Eabs} was moderate and primarily localized near the biomass burning sources, where the mass ratio (M_r) reaches its highest values. The overall bias of BC_{Eabs} is reduced by 3% compared to CTRL. A significant improvement in aerosol absorption was observed in BEST simulations. The inclusion of the BrC treatment enabled the model to reproduce the spatial pattern of AAOD much more closely to that observed by OMI. This improvement was also reflected in the statistical indices with the Taylor score increasing more than twofold from CTRL (0.34) to BEST (0.73). Despite this progress, the mean bias still was -55%. The largest biases in BEST simulations were found in Western USA and North Africa. The latter could be related to the errors in simulating the aerosol dust absorption; however, uncertainties in OMI retrievals must also be considered. We will explore this issue in more detail at the end of this section.

Figure 8 shows the comparison of daily AAOD averaged time series at 440 and 675 nm simulated in the CTRL, BC_{Eabs}, and BEST against observations from AERONET sites in the R1, R2, and R3 regions. Generally, the AAOD simulated in CTRL was underestimated, particularly during peak events related to the Canadian forest fires across all three regions. Including the BC absorption enhancement (BC_{Eabs}), a moderate improvement in AAOD simulation was observed at 440 nm Conversely, at 675 nm, the inclusion of BC E_{abs} resulted in a more accurate prediction of AAOD peaks both near the fire sources (R1) and downwind (R2), as well as in late June over western Europe (R3), attributed to transoceanic smoke transport from North America. This improvement is attributable to the dominance of BC at this wavelength, since BrC primarily absorbs solar radiation in the UV range. Consequently, at 675 nm the BC_{Eabs} and BEST simulations were identical, and the results obtained at this wavelength may be considered an evaluation of BC E_{abs} parameterization.

Figure 9 displays the scatter plots of the daily AAOD at 440 nm simulated in CTRL, BC_{Eabs}, and BEST models with the AAOD measurements from the AERONET sites in R1, R2, and R3. The summary of the statistical indices is reported in Figure 10. In general, the correlation coefficient remained constant across the simulations (about 0.70, 0.64, and 0.53 in R1, R2, and R3, respectively). This indicates that all three the models were able to capture the temporal variations of absorption. It should be noted that correlation, as well as NSE and TS, decreased moving away from the fire sources, most likely because in R1 the AAOD simulation was most affected by BB emissions, while far from boreal wildfires the mixing with other sources may alter the relative contribution of the absorbing and scattering aerosols, lowering the performance indices. At the same time, RMSE and STDE decreased moving downwind of the fires.

The bias represented the most varying metric. The CTRL simulation underpredicted the AAOD by 18% in R1, while it became negligible after including BC enhancement in the model. The addition of the BrC absorption (BEST), lead to a positive bias of +30%. This result could be attributed to the presence of "browner" BB-BrC, whose absorption could be overestimated, given the high uncertain of its MAC. Moreover, as highlighted also in Section 3.1 for the AOD, model evaluation in R1 may be affected by the limited number of AERONET observations available in this area. Similar results in terms of bias are obtained for the R2 and R3. The CTRL simulation underestimated the absorption by about 40%, while in BC_{Eabs} the bias was reduced to about -25%, becoming slightly positive in BEST.

The same analysis has been performed for AAOD at 675 nm. The results of the comparison are reported in Figures S4 and S5. As for AAOD at 440 nm, the correlation coefficient was constant across model simulations and decreased moving away from boreal wildfires. Its values were about 0.75, 0.65, and 0.45 in R1, R2, and R3 respectively. The same behavior was exhibited by NSE and TS. Conversely RMSE and STDE improved downwind the BB sources. Also in this case, the metric that showed the most variations among simulations was the bias. In R1, NMB was negligible in CTRL, but it increased at +25% in BC_{Eabs}. CTRL underestimated the AAOD at 675 nm by 18% and 26% in R2 and R3, respectively. Adding the BC absorption enhancement, the bias became negligible in R2 and reduced to -9% in R3.

In summary, the evaluation demonstrated that the new absorption scheme implemented in CHIMERE overall enhances the model skill in reproducing the observed AAOD patterns. The uncertainties of absorption treatment used in this work are mostly related to the missing of some blanching effects due to in-cloud processes of primary BrC and SOA ageing. Additionally, assumptions regarding the MAC of browner BB-BrC could introduce further uncertainty. Furthermore, the uncertainties could also arise from the simplified parameterization of E_{abs}. In our model, the absorption enhancement predicted by core-shell model ($E_{abs_{cs}}$) is maintained at the fixed value of 1.5, which may not accurately capture the variability observed under different atmospheric conditions.

Moreover, uncertainties associated with AERONET and OMI data could affect the model comparison with observations. In our analysis, we complemented the L2.0 of AERONET for AAOD with L1.5 measurements, as AAOD in the L2 dataset was provided only for AOD at 440 nm larger than 0.4. The uncertainty of single scattering albedo (SSA), used to derive AAOD, is site dependent. Generally, the uncertainty related to SSA retrieval varies with AOD, ranging from approximately ±0.03 for AOD at 440 nm greater than 0.5 to ±0.05–0.07 for AOD less than 0.2 (Sinyuk et al., 2020). Furthermore, this uncertainty increases with larger wavelengths. Concerning the uncertainty of OMI retrieval, the comparison of OMI AAOD with AERONET data is displayed in Figure S6. OMI shows an average positive bias of 66% with respect to AERONET. The most considerable discrepancies between AERONET and OMI data are found in the western United States, where we noted the most important error in CHIMERE AAOD prediction with respect to OMI data.

4 Direct radiative effect

In this section, we have assessed the impact of new treatment of BC and OA absorption on the AAOD simulation and its implication for the DRE. This analysis was conducted over the regular CHIMERE domain.

Figure 11 shows the total and BB aerosols average AAOD at 550 nm for June 2023, as calculated in CTRL and BEST simulations. The domain averages of AAOD are reported in Table 4. The total average AAOD was 0.0068 in CTRL simulation, while in the enhanced model (BEST) it increased to 0.0089 (+31%). In the Canadian wildfire source regions, AAOD in the BEST simulation increased by 35-40% relative to the CTRL run, with some areas showing a rise of up to 45% (Figure S7). The relative increase in AAOD could reach up to 50% in regions where BB aerosols are mixed with BF sources, such as in the southeastern USA. Over the Atlantic Ocean and the Arctic, the relative increase was 30-35%. A 35-40% increase was also observed over Eastern Europe, largely due to BF emissions of OA. AAOD due to BB was 0.0047 in the CTRL run and increased to 0.0066 (+40%) in BEST simulation. According to our model, BB contributes approximately 74% to the total aerosol absorption within the considered domain. The maximum uncertainty in domain-average AAOD from the enhanced model was evaluated by comparing the BEST run with extreme absorption scenarios (L-ABS and H-ABS tests), resulting in an uncertainty range of -10/+24% for total AAOD and -14/+30% for BB AAOD.

DRE at the top of the atmosphere (TOA) has been calculated offline with a simplified formalization provided by Seinfeld and Pandis (2016). The details of this formulation are reported in Section S2 of the Supplementary Material.

Figure 12 displays the average BB all-sky DRE for June 2023, as calculated in CTRL and BEST simulations. Table 5 reports the domain averages of clear and all-sky top of the atmosphere (TOA) DRE. The uncertainty associated with the DRE from the enhanced model was evaluated using the same approach as for AAOD.

In the default model, the all-sky DRE related to the intense Canadian wildfire event was -2.1 W/m², with the strongest cooling effects observed over oceans and land, reaching -30/-20 W/m² near the BB sources in Canada. By contrast, warming effects were observed over snow-covered land and sea ice, with a warming of up to 10-15 W/m² in Arctic regions downwind of the BB sources.

In the BEST model, the all-sky DRE was reduced to -1.9 W/m² (-2.0/-1.8 W/m², ±5%), indicating an additional monthly average warming of +0.2 W/m² (+10%) in the enhanced model simulation of the Canadian wildfire climatic impact. This supplemental warming was most pronounced over snow/ice-covered regions, with a DRE reduction up to 2.5-3.0 W/m² in North America downwind of the fires and up to 2.0-2.5 W/m² in southern Greenland. The cooling effect in BEST was also reduced by up to 1.5 W/m² in Canada near the source regions and by few tens of W/m² over the Atlantic Ocean and Europe.

Finally, it is insightful to examine the variation in DRE between the default and enhanced models, normalized to the change in AAOD at 550 nm between the two simulations. The resulting normalized BB all-sky ΔDRE was 105 W/m^2/AAOD. This value suggests a significant DRE sensitivity to AAOD change in the model.

These results emphasize that accurate prediction of BC and BrC sunlight absorption is crucial for understanding the impact of intense boreal wildfires on regional climate. Our findings suggest that models lacking proper treatment of carbonaceous aerosol absorption may overestimate the cooling effect of boreal wildfires. Therefore, improving aerosol absorption parameterizations is crucial, along with incorporating the feedback between climate and aerosol smoke from boreal fires, both in near-future climate predictions and the development of effective mitigation strategies. Recent study of Allen et al. (2024) suggest that anthropogenic aerosol mitigation strategies will likely increase boreal forest fires, but the full impact of resulting emissions on the climate system remains uncertain. Without adequate treatment of BC and BrC absorption, the climatic effect of these emissions could be significantly misrepresented.

5 Conclusions

Black carbon (BC) and brown carbon (BrC) are light-absorbing aerosols which play a key role in the climatic system. Boreal wildfires are significant sources of these particles. Boreal wildfire events are increasing due to climate change. Accurate modelling of BC and BrC absorption is essential for predicting the direct radiative effect (DRE) of these events. In this study, we modelled the BC and BrC absorption during the severe Canadian wildfires of June 2023 using an enhanced CHIMERE model and assessed the impact of these improvements on the DRE of the wildfires.

The CHIMERE model was configured on a large domain spanning from North America to Eastern Europe, including the high latitude up to 75°N. We implemented in the model a parameterization for BC absorption enhancement (E_{abs}), which depends on the mixing state of BC particles, through the mass ratio of non-BC to BC aerosols, according to the work of Liu et al. (2017). We also implemented an advanced scheme for BrC absorption, which accounts for "browning" and "blanching" processes due to photochemical ageing, following the approach of DeLessio et al. (2024). A series of simulations were conducted to assess the impact of BC E_{abs} and BrC on aerosol absorption prediction. Model performance was evaluated through a statistical comparison with aerosol optical depth (AOD) and absorbing aerosol optical depth (AAOD) data from satellite instruments (MODIS and OMI) and ground-based AERONET stations, focusing on regions impacted by Canadian wildfires.

The model captured the spatial patterns of AOD, particularly the long-range transport of aerosols from Canadian wildfires toward the East Coast of North America and across the Atlantic to Europe. The model generally underestimated AOD compared to satellite observations, with biases ranging from 15-30%. Correlation coefficients for the comparison with MODIS and OMI AOD were 0.77 and 0.65, respectively, while comparisons with AERONET showed a correlation of 0.79 and a bias of -24%.

The default model (CTRL) underestimated AAOD retrieved by OMI, particularly near biomass burning sources, with a bias of up to -78%. A moderate improvement was observed by including in model the BC absorption enhancement (BC_{Eabs}), but the most substantial advancements were achieved in the BEST simulations, which included both E_{abs} and BrC treatment, improving spatial patterns and statistical indices. The model comparison with AAOD measurements at 440 and 675 nm from AERONET exhibited a correlation of about 0.75 near the wildfire sources, which tends to decrease moving downwind from these sources. In general, the CTRL run underestimated the observed AAOD, while a significant improvement of the model was obtained in the BEST simulation.

The enhanced model (BEST) increased the monthly domain average AAOD at 550 nm by 31% compared to the CTRL, with the most significant changes observed near the Canadian wildfires and areas where biomass burning aerosols mixed with fossil fuel sources. Canadian smoke aerosols contributed approximately to 74% of total aerosol absorption.

The all-sky TOA DRE associated with the Canadian wildfires of June 2023 was estimated to be -2.1 W/m² in the CTRL run. In the best simulation, this value was reduced to -1.9 W/m², indicating an additional warming of +0.2 W/m² (+10%), attributable to the enhanced treatment of BC and BrC absorption. The increased in DRE calculated in BEST was more pronounced in the regions covered by snow and ice, such as the Arctic and Southern Greenland. Furthermore, the normalized all-sky DRE

change resulting from the increase in AAOD obtained in BEST simulation was +105 W/m²/AAOD, highlighting the critical role of aerosol absorption in radiative balance during the intense boreal wildfire events.

The main uncertainties in this study are linked to the absorption scheme implemented in CHIMERE, which does not account for the blanching due to in cloud-processes of primary BrC and SOA ageing. Moreover, the complex part of refractive index adopted for browner BrC could introduce an additional uncertainty factor. Another source of uncertainty is related to the assumption of a constant E_{abs} resulting from the core-shell morphology of BC. To evaluate the impact of these uncertainties, we perturbed the BEST simulation with low and high absorption scenarios. The results indicate an error of ±5% in the DRE estimate attributed to Canadian wildfires.

Overall, the findings of this investigation demonstrate the importance of an accurate simulation of BC and BrC absorption to properly assess the regional climatic impact of intense boreal wildfire. The lack of this factor in the models may results in an overestimation of the radiative cooling effect of boreal fires. Consequently, improving the parameterizations of carbonaceous aerosol absorption is essential for reliable near-future climatic predictions and effectively evaluation of the efficiency of the aerosol mitigation strategies.

Code/Data availability: CHIMERE simulations and model code are available at this link https://osf.io/dnygq/. This is a temporary link for peer review only and will be made public at acceptance. AERONET data are freely available at the following website https://aeronet.gsfc.nasa.gov/new_web/data.html. MODIS and OMI data may be downloaded at https://disc.gsfc.nasa.gov/.

Author Contributions: PT and LDA conceptualized the study and developed the methodology. PT and LM developed the model. PT performed the model simulations with contribution from LDA. PT, LDA and ADM performed the formal analysis. PT, LDA and VC prepared and wrote the original draft. PT, LDA, ADM, VC, LM, ER, and GP reviewed the original draft.

Competing interests: The authors declare that they have no conflict of interest.

Funding: This work was not supported by any external funding.

References

Adachi, K., Chung, S. H., and Buseck. P. R. (2010). Shapes of soot aerosol particles and implications for their effects on climate. *J. Geophys. Res.*, 115, D15206, https//doi.org/10.1029/2009JD012868.

Akagi, S. K., Craven, J. S., Taylor, J. W., McMeeking, G. R., Yokelson, R. J., Burling, I. R., Urbanski, S. P., Wold, C. E., Seinfeld, J. H., Coe, H., Alvarado, M. J., and Weise, D. R. (2012). Evolution of trace gases and particles emitted by a chaparral fire in California. *Atmos. Chem. Phys.*, 12, 1397–1421, https//doi.org/10.5194/acp-12-1397-2012.

Alfaro, S. C., and Gomes, L. (2001). Modeling mineral aerosol production by wind erosion: Emission intensities and aerosol size distribution in source areas. *J. Geophys. Res*., 106, 18075–18084, https//doi.org/10.1029/2000JD900339.

Alexander, D. T. L., Crozier, P. A., and Anderson, J. R. (2008). Brown carbon spheres in East Asian outflow and their optical properties. *J. Geophys. Res.*, 321, 833–836, https//doi.org/10.1126/science.1155296.

Allen, R. J., et al. (2024). Are Northern Hemisphere boreal forest fires more sensitive to future aerosol mitigation than to greenhouse gas–driven warming?. *Sci. Adv*., 10, DOI:10.1126/sciadv.adl4007.

Andreae, M. O., and Gelencsér, A. (2006). Black carbon or brown carbon? The nature of light-absorbing carbonaceous aerosols. *Atmos. Chem. Phys.*, 6, 3131–3148, https//doi.org/10.5194/acp-6-3131-2006.

Arola, A., Stu G., Kazadzis, S., Dey, S., and Tripathi, S. N. (2011). Inferring absorbing organic carbon content from AERONET data. *Atmos. Chem. Phys.*, 11, 215–225, https//doi.org/10.5194/acp-11-215-2011.

Balzarini, A., Pirovano, G., Honzak, L., Žabkar, R., Curci, G., Forkel, R., Hirtl, M., San José, R., Tuccella, P., and Grell, G.A. (2015). WRF-Chem model sensitivity to chemical mechanisms choice in reconstructing aerosol optical properties. *Atmos. Environ.*, 115, 604-619, https//doi.org/10.1016/j.atmosenv.2014.12.033.

Bessagnet, B., Hodzic, A., Vautard, R., Beekmann, M., Cheinet, S., Honoré, C., Liousse, C., and Rouil, L. (2004). Aerosol modeling with CHIMERE—Preliminary evaluation at the continental scale. *Atmos. Environ.*, 38, 2803–2817, https//doi.org/10.1016/j.atmosenv.2004.02.034.

Bessagnet, B., Menut, L., Curci, G., Hodzic, A., Guillaume, C., Liousse, C., Moukhtar, S., Pun, B., Seigneur, C., and Schulz, M. (2008). Regional modeling of carbonaceous aerosols over Europe-Focus on secondary organic aerosols. *J. Atmos. Chem.*, 61, 175–202, https//doi.org/10.1007/s10874-009-9129-2.

Bond, T. C., and Bergstrom R. W. (2006). Light absorption by carbonaceous particles: an investigative review. *Aerosol. Sci. Tech.*, 40, 27–67, https//doi.org/10.1080/02786820500421521.

Bond, T. C., Bhardwaj, E., Dong, R., Jogani, R., Jung, S. K., Roden, C., Streets, D. G., and Trautmann, D. G. (2007). Historical emissions of black and organic carbon aerosol from energy-related combustion, *Global Biogeochem.*, 21, 1850–2000, https//doi.org/10.1029/2006GB002840.

Bond, T. C., Doherty, S. J., Fahey, D. W., Forster, P. M., Berntsen, T., De Angelo B. J., Flanner, M.G., Ghan, S., Kärcher, B., Koch, D., Kinne, S., Kondo, Y., Quinn, P. K., Sarofim, M. C., Schultz, M. C., Schulz, M., Venkataraman, C., Zhang, H., Zhang, S., Bellouin, N., Guttikunda, S. K., Hopke, P. K., Jacobson, M. Z., Kaiser, J. W., Klimont, Z., Lohmann, U., Schwarz, J. P., Shindell, D., Storelvmo, D., Warren, S. G., and Zender, C. S. (2013). Bounding the role of black carbon in the climate system: A scientific assessment. *J. Geophys. Res.-Atmos.*, 118, 5380–5552, https//doi.org/10.1002/jgrd.50171.

Bondy, A., Bonanno, D., Moffet, R., Wang, B., Laskin, A., and Ault, A. (2018). The diverse chemical mixing state of aerosol 430 particles in the southeastern United States. *Atmospheric Chemistry and Physics*, 18, 12595-12612, 10.5194/acp-18- 12595-2018.

Bones, D. L., Henricksen, D. K., Mang, S. A., Gonsior, M., Bateman, A. P., Nguyen, T. B., Cooper, W. J., and Nizkorodov, S. A. (2010). Appearance of strong absorbers and fluorophores in limonene-O3 secondary organic aerosol due to NH4+ mediated chemical aging over long time scales. *J. Geophys. Res.*, 115, https//doi.org/10.1029/2009JD012864.

Briant, R., Tuccella, P., Deroubaix, A., Khvorostyanov, D., Menut, L., Mailler, S., and Turquety, S. (2017). Aerosol–radiation interaction modelling using online coupling between the WRF 3.7.1 meteorological model and the CHIMERE 2016 chemistry-transport model, through the OASIS3-MCT coupler. *Geosci. Model Dev*., 10, 927–944, https//doi.org/10.5194/gmd-10-927-2017.

Brown, H., Liu, X., Feng, Y., Jiang, Y., Wu, M., Lu, Z., Wu, C., Murphy, S., and Pokhrel, R. (2018). Radiative effect and climate impacts of brown carbon with the Community Atmosphere Model (CAM5), *Atmos. Chem. Phys.*, 18, 17745–17768, https//doi.org/10.5194/acp-18-17745-2018.

Brown, H., Wang, H., Flanner, M., Liu, X., Singh, B., Zhang, R., Yang, Y., and Wu M. (2022). Brown carbon fuel and emission source attributions to global snow darkening effect. J. Adv. *Model Earth Sy.*, 14, e2021MS002768, https//doi.org/10.1029/2021MS002768.

Byrne, B., Liu, J., Bowman, K.W. et al. (2024). Carbon emissions from the 2023 Canadian wildfires. *Nature*, https://doi.org/10.1038/s41586-024-07878-z.

Cappa, C. D., Onasch, T. B., Massoli, P., Worsnop D. R., Bates, T. S., Cross, E. S., Davidovits, P., Hakala, J., and Hayden, K. L. (2012). Radiative Absorption Enhancements Due to the Mixing State of Atmospheric Black Carbon, *Science*, 337, 1078–1081, https//doi.org/10.1126/science.1223447.

Carter, T. S., Heald, C. L., Jimenez, J. L., Campuzano-Jost, P., Kondo, Y., Moteki, N., Schwarz, J. P., Wiedinmyer, C., Darmenov, A. S., and da Silva, A. M. (2020). How emissions uncertainty influences the distribution and radiative impacts of smoke from fires in North America. *Atmos. Chem. Phys.*, 20, 2073-2097, https//doi.org/10.5194/acp-20-2073-2020.

Chen, F., and Dudhia, J. (2001). Coupling an Advanced Land Surface-Hydrology Model with the Penn State-NCAR MM5, Modeling System. Part I: Model Implementation and Sensitivity. *Mon. Weather Rev*., 129, 569–585, https//doi.org/10.1175/1520-0493(2001)129<0569:CAALSH>2.0.CO;2.

Chen, Y., and Bond, T. C. (2010). Light absorption by organic carbon from wood combustion. *Atmos. Chem. Phys.*, 10, 1773–1787, https//doi.org/10.5194/acp-10-1773-2010.

Cheng, Z., Atwi, K. M., Yu, Z., Avery, A., Fortner, E. C., Williams, L., Majluf, F., Krechmer, J. E., Lambe, A. T., and Saleh, R. (2020). Evolution of the light-absorption properties of combustion brown carbon aerosols following reaction with nitrate radicals, *Aerosol Sci. Tech.*, 54, 849–863, https://doi.org/10.1080/02786826.2020.1726867.

Clarke, A. D., Shinozuka, Y., Kapustin, V. N., Howell, S., Huebert, B., Doherty, S., Anderson, T., Covert, D., Anderson, J., Hua, X., Moore II, K. G., McNaughton, R., Carmichael, G., and Weber, R. (2004). Size distributions and mixtures of dust and black carbon aerosol in Asian outflow: physiochemistry and optical properties. *J. Geophys. Res*., 109, D15S09, https//doi.org/10.1029/2003JD004378.

Craig, A., Valcke, S., and Coquart, L. (2017). Development and performance of a new version of the OASIS coupler, OASIS3-MCT_3.0, *Geosci. Model Dev.*, 10, 3297–3308, https//doi.org/10.5194/gmd-10-3297-2017.

Curci, G., Hogrefe, C., Bianconi, R., Im, U., Balzarini, A., Baro, R., Brunner, D., Forkel, R., Giordano, L., Hirtl, M., Honzak, L., Jimenez-Guerrero, P., Knote, C., Langer, M., Makar, P. A., Pirovano, G., Perez, J. L., San Jose, R., Syrakov, D., Tuccella, P., Werhahn, J., Wolke, R., Zabkar, R., Zhang, J., and Galmarini, S. (2015). Uncertainties of simulated aerosol optical properties induced by assumptions on aerosol physical and chemical properties: an AQMEII-2 perspective. *Atmos. Environ.*, 115, 541–552, https//doi.org/10.1016/j.atmosenv.2014.09.009.

Curci, G., Alyuz, U., Barò, R., Bianconi, R., Bieser, J., Christensen, J. H., Colette, A., Farrow, A., Francis, X., Jiménez-Guerrero, P., Im, U., Liu, P., Manders, A., Palacios-Peña, L., Prank, M., Pozzoli, L., Sokhi, R., Solazzo, E., Tuccella, P., Unal, A., Vivanco, M. G., Hogrefe, C., and Galmarini, S. (2019). Modelling black carbon absorption of solar radiation: combining external and internal mixing assumptions, *Atmos. Chem. Phys.*, 19, 181–204, https//doi.org/10.5194/acp-19-181-2019.

DeLessio, M. A., Tsigaridis, K., Bauer, S. E., Chowdhary, J., and Schuster, G. L. (2024). Modeling atmospheric brown carbon in the GISS ModelE Earth system model, *Atmos. Chem. Phys*., 24, 6275–6304, https//doi.org/10.5194/acp-24-6275-2024.

Derognat, C., Beekmann, M., Baeumle, M., Martin, D., and Schmidt, H. (2003). Effect of biogenic volatile organic compound emissions on tropospheric chemistry during the Atmospheric Pollution Over the Paris Area (ESQUIF) campaign in the Ile-de-France region. *J. Geophys. Res.*, 108, https//doi.org/10.1029/2001JD001421.

Dingle, J. H., Zimmerman, S., Frie, A. L., Min, J., Jung, H., and Bahreini, R. (2019). Complex refractive index, single scattering albedo, and mass absorption coefficient of secondary organic aerosols generated from oxidation of biogenic and anthropogenic precursors. *Aerosol Sci. Technol.*, 53, 449–463, https://doi.org/10.1080/02786826.2019.1571680,.

Drugé, T., Nabat, P., Mallet, M., Michou, M., Rémy, S., and Dubovik, O. (2022). Modeling radiative and climatic effects of brown carbon aerosols with the ARPEGE-Climat global climate model. *Atmos. Chem. Phys.*, 22, 12167–12205, https//doi.org/10.5194/acp-22-12167-2022.

Dubovik, O., Holben, B., Eck, T. F., Smirnov, A., Kaufman, Y. J., and King, M. D. (2002). Variability of absorption and optical properties of key aerosol types observed in worldwide locations, *J. Atmos. Sci.*, 59, 590–608, doi:10.1175/1520-0469(2002)059<0590:VOAAOP>2.0.CO;2.

Esteve, A.R., Highwood, E. J., Morgan, W. T., Allen, G., Coe, H., Grainger, R. G., Brown, P., and Szpek, K. (2014). A study on the sensitivities of simulated aerosol optical properties to composition and size distribution using airborne measurements, *Atmos. Envir*on., 89, 517-524, https//doi.org/10.1016/j.atmosenv.2014.02.063.

Eckdahl, J. A., Kristensen, J. A., and Metcalfe, D. B. (2022). Climatic variation drives loss and restructuring of carbon and nitrogen in boreal forest wildfire. *Biogeoscie*nces, 19, 2487–2506, https://doi.org/10.5194/bg-19-2487-2022,.

Feng, Y., Ramanathan, V., Kotamarthi, V. R. (2013). Brown carbon: A significant atmospheric absorber of solar radiation? *Atmos. Chem. Phys.*, 13, 8607–8621, https//doi.org/10.5194/acp-13-8607-2013.

Fierce, L., Onasch, T. B., Cappa, D. C., Claudio, M., Swarup, C., Janarjan, B., Davidovits, P., Fischer, D. Al., Helgestad, T., Lambe, A. T., Sedlacek, A. J., Smith, G. D., and Wolff, L. (2020). Radiative absorption enhancements by black carbon controlled by particle-to-particle heterogeneity in composition. *P. Natl. Acad. Sci. USA*, 117(10), 5196-5203, https//doi.org/10.1073/pnas.1919723117.

Filonchyk, M. and Peterson, M. P. (2024). Changes in aerosol properties at the El Arenosillo site in Southern Europe as a result of the 2023 Canadian forest. *Environmental Research*, 260, https://doi.org/10.1016/j.envres.2024.119629.

Fleming, L. T., Lin, P., Roberts, J. M., Selimovic, V., Yokelson, R., Laskin, J., Laskin, A., and Nizkorodov, S. A. (2020). Molecular composition and photochemical lifetimes of brown carbon chromophores in biomass burning organic aerosol. *Atmos. Chem. Phys*., 20, 1105–1129, https//doi.org/10.5194/acp-20-1105-2020.

Flanner, M. G., Zender, C. S., Randerson, J. T., and Rasch, P. J. (2007). Present-day climate forcing and response from black carbon in snow. *J. Geophys. Res*., 112, D11202, https//doi.org/10.1029/2006JD008003.

Flanner, M. G., Zender, C. S., Hess, P. G., Mahowald, N. M., Painter, T. H., Ramanathan, V., and Rasch, P. J. (2009). Springtime warming and reduced snow cover from carbonaceous particles. *Atmos. Chem. Phys.*, 9, 2481–2497, https//doi.org/10.5194/acp-9-2481-2009.

Folberth, G. A., Hauglustaine, D. A., Lathière, J., and Brocheton, F. (2006). Interactive chemistry in the Laboratoire de Météorologie Dynamique general circulation model: model description and impact analysis of biogenic hydrocarbons on tropospheric chemistry, *Atmos. Chem. Phys.*, 6, 2273–2319, https//doi.org/10.5194/acp-6-2273-2006.

Forrister, H., Liu, J., Scheuer, E., Dibb, J., Ziemba, L., Thornhill, K. L., Anderson, B., Diskin, G., Perring, A. E., Schwarz J. P., Campuzano-Jost, P., Day, D. A., Palm, B. B., Jimenez J. L., Nenes, A., and Weber, J. (2015). Evolution of brown carbon in wildfire plumes. *Geophys. Res. Lett.*, 42, https//doi.org/10.1002/2015GL063897.

Gillett, N.P. (2004). Detecting the effect of climate change on Canadian forest fires. *Geophysical Research Letters*, 31 (18), doi:10.1029/2004gl020876.

Grell, G. A. and Freitas, S. R.: A scale and aerosol aware stochastic convective parameterization for weather and air quality modeling, Atmos. Chem. Phys., 14, 5233–5250, https//doi.org/10.5194/acp-14- 5233-2014, 2014.

Guenther, A., Karl, T., Harley, P., Wiedinmyer, C., Palmer, P. I., and Geron, C. (2006). Estimates of global terrestrial isoprene emissions using MEGAN (Model of Emissions of Gases and Aerosols from Nature), *Atmos. Chem. Phys.*, 6, 3181–3210, https//doi.org/10.5194/acp-6-3181-2006.

Guenther, A. B., Jiang, X., Heald, C. L., Sakulyanontvittaya, T., Duhl, T., Emmons, L. K., and Wang, X. (2012). The Model of Emissions of Gases and Aerosols from Nature version 2.1 (MEGAN2.1): an extended and updated framework for modeling biogenic emissions. *Geosci. Model Dev*., 5, 1471–1492, https//doi.org/10.5194/gmd-5-1471-2012.

Gustafsson, O., and Ramanathan, V. (2016). Convergence on climate warming by black carbon aerosols. *P. Natl. Acad. S*ci. *USA*, 113, 4243–4245, https//doi.org/10.1073/pnas.1603570113.

Hansen, J., and Nazarenko, L. (2004). Soot climate forcing via snow and ice albedos. *PNAS*, 101 (2), 423-428, https//doi.org/10.1073/pnas.2237157100.

Hua, W., Lou, S., Huang, X., Xue, L., Ding, K., Wang, Z., and Ding, A. (2024). Diagnosing uncertainties in global biomass burning emission inventories and their impact on modeled air pollutants, *Atmos. Chem. Phys.*, https//doi.org/10.5194/acp-24-6787-2024.

Hecobian, A., Zhang, X., Zheng, M., Frank, N., Edgerton, E. S., and Weber, R. J. (2010). Water-Soluble Organic Aerosol material and the light-absorption characteristics of aqueous extracts measured over the Southeastern United States. Atmos. *Chem. Phys*., 10, 5965–5977, https//doi.org/10.5194/acp-10-5965-2010.

Hems, R. F., Schnitzler, E. G., Bastawrous, M., Soong, R., Simpson, A. J., and Abbatt, J. P. D. (2020). Aqueous Photoreactions of Wood Smoke Brown Carbon. *ACS Earth Space Chem.*, 4, 1149–1160, https://doi.org/10.1021/acsearthspacechem.0c00117.

Hems, R. F., Schnitzler, E. G., Liu-Kang, C., Cappa, C. D., and Abbatt, J. P. D. (2021). Aging of Atmospheric Brown Carbon Aerosol. *ACS Earth Space Chem*., 5, 722–748, https//doi.org/10.1021/acsearthspacechem.0c00346e.

Holben, B. N., Tanré, D., Smirnov, A., Eck, T. F., Slutsker, I., Abuhassan, N., Newcomb, W. W., Schafer, J. S., Chatenet, B., Lavenu, F., Kaufman, Y. J., Vande Castle, J., Setzer, A., Markham, B., Clark, D., Frouin, R., Halthore, R., Karneli, A., O'Neill N. T., Pietras, C., Pinker, R. T., Voss, K., and Zibordi, G. (2001). An emerging ground-based aerosol climatology: Aerosol Optical Depth from AERONET. *J. Geophys. Res*., 106(D11), 12067–12097. https//doi.org/10.1029/2001JD900014.

Hong, S.-Y., Noh, S.-Y., and Dudhia, J. (2006). A new vertical diffusion package with an explicit treatment of entrainment processes. *Mon. Weather Rev*., 134, 2318–2341, https//doi.org/10.1175/MWR3199.1.

Iacono, M. J., Delamere, J. S., Mlawer, E. J., Shephard, W., Clough, S. A., and Collins, W. D. (2008). Radiative forcing by long-lived greenhouse gases: Calculations with the AER radiative transfer models, *J. Geophys. Res.*, 113, https//doi.org/10.1029/2008JD009944.

IPCC (2021). *Climate Change 2021. Physical Science Basis. Contribution of Working Group I to the Sixth Assessment Report of the Intergovernmental Panel on Climate Change*, Cambridge UK and New York, NY, USA: Cambridge University Press.

Jacobson, M. Z. (2000). A physically-based treatment of elemental carbon optics: Implications for global direct forcing of aerosols. *Geophysical Research Letters*, 27, 217–220. https://doi.org/10.1029/1999GL010968

Jacobson, M. Z. (2001). Global direct radiative forcing due to multicomponent anthropogenic and natural aerosols. *Journal of Geophysical Research*, 106, 1551–1568.

Jo, D. S., Park, R. J., Lee, S., Kim, S.-W., and Zhang, X. (2016). A global simulation of brown carbon: implications for photochemistry and direct radiative effect, *Atmos. Chem. Phys.*, 16, 3413–3432, https//doi.org/10.5194/acp-16-3413-2016.

Kaiser, J. W., Heil, A., Andreae, M. O., Benedetti, A., Chubarova, N., Jones, L., Morcrette, J.-J., Razinger, M., Schultz, M. G., Suttie, M., and van der Werf, G. R. (2012). Biomass burning emissions estimated with a global fire assimilation system based on observed fire radiative power. *Biogeosciences*, 9, 527–554, https//doi.org/10.5194/bg-9-527-2012.

Kasthuriarachchi, N. Y., Rivellini, L.-H., Adam, M. G., and Lee, A. K. Y. (2020). Light Absorbing Properties of Primary and Secondary Brown Carbon in a Tropical Urban Environment. *Envir. Sci. Tech*., 54(17), 10808-10819, https//doi.org/10.1021/acs.est.0c02414.

Kaufman, Y. J., Tanré, D., Remer, L. A., Vermote, E. F., Chu, A., and Holben, B. N. (1997). Operational remote sensing of tropospheric aerosol over land from EOS moderate resolution imaging spectroradiometer. *J. Geophys. Res*., 102(D14), 17051–17067, https//doi.org/10.1029/96JD03988.

Kirchstetter, T. W., and Thatcher, T. L. (2012). Contribution of organic carbon to wood smoke particulate matter absorption of solar radiation, *Atmos. Chem. Phys.*, 12, 6067–6072, https//doi.org/10.5194/acp-12-6067-2012.

Kompalli, S. K., Babu, S. S., Ajith, T.C., Moorthy, K. K., Satheesh, S. K., Boopathy, R., Das, T., Liu, D., Allan, J., and Coe, H. (2023). Aging of biomass burning emissions in the Indo-Gangetic Plain outflow: Implications for black carbon light-absorption enhancement, *Atmos. Res*., 294, 106949, https//doi.org/10.1016/j.atmosres.2023.106949.

Kong, Y., Zhi, G., Jin, W., Zhang, Y., Shen, Y., Li, Z., Sun, J., and Ren, Y. (2024). A review of quantification methods for light absorption enhancement of black carbon aerosol, *Sci. Tot. Env.*, 924, 171539, https//doi.org/10.1016/j.scitotenv.2024.171539.

Konovalov, I. B., Golovushkin, N. A., Beekmann, M., Siour, G., Zhuravleva, T. B., Nasrtdinov, I. M., and Kuznetsova, I. N. (2023). On the importance of the model representation of organic aerosol in simulations of the direct radiative effect of Siberian biomass burning aerosol in the eastern Arctic, *Atmos. Envir.*, 309, 119910, https//doi.org/10.1016/j.atmosenv.2023.119910.

Konovalov, I. B., Golovushkin, N. A., and Beekmann, M. (2024a). Wildfire-smoke-precipitation interactions in Siberia: Insights from a regional model study. *Sci. Tot. Env.*, 951, 175518, https//doi.org/10.1016/j.scitotenv.2024.175518.

Konovalov, I.B., Golovushkin, N. A. (2024b). Model Analysis of Origination of Semidirect Radiative Effect of Siberian Biomass Burning Aerosol in the Arctic. *Atmos. Ocean. Opt.,* 37, 382–393, https://doi.org/10.1134/S1024856024700477

Kuhns, H., Knipping, E. M., and Vukovich, J. M. (2005). Development of a United States–Mexico Emissions Inventory for the Big Bend Regional Aerosol and Visibility Observational (BRAVO) Study, *J. Air Waste Manage. Assoc.*, 55, 677–692, https//doi.org/10.1080/10473289.2005.10464648.

Lack, D. A., Langridge, J. M., Bahreini, R., Cappa, C. D., Middlebrook, A. M., and Schwarz, J. P. (2012). Brown carbon and internal mixing in biomass burning particles. *P. Natl. Acad. Sci. USA*, 109, 14802–14807, https//doi.org/10.1073/pnas.1206575109.

Lambe, A. T., Cappa, C. D., Massoli, P., Onasch, T. B., Forestieri, S. D.. Martin, A. T., Cummings, M. J., Croasdale, D. R., Brune, W. H., Worshop, D. R., and Davidovits, P. (2013). Relationship between oxidation level and optical properties of secondary organic aerosol, *Environ. Sci. Technol*., 47, 6349–6357, https//doi.org/10.1021/es401043j.

Lan, Z. J., Huang, X. F., Yu, K.Y., Sun, T.L., Zeng, L.W., Hu, M. (2013). Light absorption of black carbon aerosol and its enhancement by mixing state in an urban atmosphere in South China. *Atmos. Environ.*, 69, 118-123, doi.org/10.1016/j.atmosenv.2012.12.009.

Laskin, A., Laskin, J., and Nizkorodov, S. A. (2015). Chemistry of Atmospheric Brown Carbon, *Chem. Rev.*, 115, 4335–4382, https//doi.org/10.1021/cr5006167.

Lee, H. J., Aiona, P. K., Laskin, A., Laskin, J., and Nizkorodov, S. A. (2014). Effect of Solar Radiation on the Optical Properties and Molecular Composition of Laboratory Proxies of Atmospheric Brown Carbon, *Envir. Scie. Tech.*, 48, 10217-10226, https//doi.org/10.1021/es502515r.

Lesins, G., Chylek, P., and Lohmann, U. (2002). A study of internal and external mixing scenarios and its effect on aerosol optical properties and direct radiative forcing, *J. Geophys. Res*., 107, 4094, https//doi.org/10.1029/2001JD000973.

Levy, R., Hsu, C., et al. (2015). MODIS Atmosphere L2 Aerosol Product. NASA MODIS Adaptive Processing System, Goddard Space Flight Center, USA: doi:10.5067/MODIS/MYD04_L2.061.

Li, F., Lawrence, D. M., and Bond-Lamberty, B. (2017). Impact of fire on global land surface air temperature and energy budget for the 20th century due to changes within ecosystems. *Environ. Res. Lett.*, 12, 044014, https//doi.org/:10.1088/1748-9326/aa6685.

Lin, G., Penner, J. E., Flanner, M. G., Sillman, S., Xu, L., and Zhou, C. (2014). Radiative forcing of organic aerosol in the atmosphere and on snow: Effects of SOA and brown carbon, J. *Geophys. Res.*, 119, 7453–7476, https//doi.org/10.1002/2013JD021186.

Lin, P., Liu, J., Shilling, J. E., Kathmann, S. M., Laskin, J., and Laskin, A. (2015). Molecular characterization of brown carbon (BrC) chromophores in secondary organic aerosol generated from photo-oxidation of toluene, *Phys. Chem. Chem. Phys*., 17, 23312-23325, https//doi.org/10.1039/C5CP02563J.

Linares, M., and Ni-Meister, W. (2024). Impact of Wildfires on Land Surface Cold Season Climate in the Northern High-Latitudes: A Study on Changes in Vegetation, Snow Dynamics, Albedo, and Radiative Forcing. *Remote Sens.*, 16, 1461, https://doi.org/10.3390/rs16081461.

Liu, P. F., Abdelmalki, N., Hung, H.-M., Wang, Y., Brune, W. H., and Martin, S. T. (2015). Ultraviolet and visible complex refractive indices of secondary organic material produced by photooxidation of the aromatic compounds toluene and m-xylene, *Atmospheric Chem. Phys.*, 15, 1435–1446, https://doi.org/10.5194/acp-15-1435-2015.

Liu, J., Lin, P., Laskin, A., Laskin, J., Kathmann, S. M., Wise, M., Caylor, R., Imholt, F., Selimovic, V., and Shilling, J. E. (2016). Optical properties and aging of light-absorbing secondary organic aerosol, *Atmos. Chem. Phys*., 16, 12815–12827, https//doi.org/10.5194/acp-16-12815-2016.

Liu, D., Whitehead, J., Alfarra, M., reyes-Villegas, E., Spracklen, D. V., Reddington, C. L., Kong, S., Williams, P. I., Ting Y.-C., Haslett, S., Taylor, J. W., Flynn, M. J., Morgan, W. T., McFiggans, G., Coe, H, and Allan, J. D. (2017). Black-carbon absorption enhancement in the atmosphere determined by particle mixing state, *Nature Geosci.*, 10, 184–188, https//doi.org/10.1038/ngeo2901.

Liu, Y., Zhang, K., Qian, Y., Wang, Y., Zou, Y., Song, Y., Wan, H., Liu, X., and Yang, X.-Q. (2018). Investigation of short-term effective radiative forcing of fire aerosols over North America using nudged hindcast ensembles, *Atmos. Chem. Phys*., 18, 31-47, https//doi.org/10.5194/acp-18-31-2018

Lukács, H., Gelencsér, A., Hammer, S., Puxbaum, H., Pio, C., Legrand, M., Kasper-Giebl, A., Handler, M., Limbeck, A., and Simpson, A. (2007). Seasonal trends and possible sources of brown carbon based on 2-year aerosol measurements at six sites in Europe, *J. Geophys. Res*., 112, D23S18, https//doi.org/10.1029/2006JD008151, 2007.

Mailler, S., Menut, L., di Sarra, A. G., Becagli, S., Di Iorio, T., Bessagnet, B., Briant, R., Formenti, P., Doussin, J.-F., Gómez-Amo, J. L., Mallet, M., Rea, G., Siour, G., Sferlazzo, D. M., Traversi, R., Udisti, R., and

Turquety, S. (2016). On the radiative impact of aerosols on photolysis rates: comparison of simulations and observations in the Lampedusa island during the ChArMEx/ADRIMED campaign, *Atmos. Chem. Phys*., 16, 1219–1244, https//doi.org/10.5194/acp-16-1219-2016.

Mailler, S., Menut, L., Khvorostyanov, D., Valari, M., Couvidat, F., Siour, G., Turquety, S., Briant, R., Tuccella, P., Bessagnet, B., Colette, A., Létinois, L., Markakis, K., and Meleux, F. (2017). CHIMERE-2017: from urban to hemispheric chemistry-transport modeling, *Geosci. Model Dev.*, 10, 2397–2423, https//doi.org/10.5194/gmd-10-2397-2017.

Menut, L., Schmechtig, C., and Marticorena, B. (2005). Sensitivity of the sandblasting fluxes calculations to the soil size distribution accuracy, *J. Atmos. Ocean. Technol.*, 22, 1875–1884, https//doi.org/10.1175/JTECH1825.1.

Menut, L., Flamant, C., Turquety, S., Deroubaix, A., Chazette, P., and Meynadier, R. (2018). Impact of biomass burning on pollutant surface concentrations in megacities of the Gulf of Guinea, *Atmos. Chem. Phys.*, 18, 2687–2707, https//doi.org/10.5194/acp18-2687-2018.

Menut L., Bessagnet, B., Mailler, S., Pennel, R., Siour, G. (2020). Impact of lightning NOx emissions on atmospheric composition and meteorology in Africa and Europe, *Atmospheres*, 11, 1128; https//doi.org/10.3390/atmos11101128.

Menut, L., Bessagnet, B., Briant, R., Cholakian, A., Couvidat, F., Mailler, S., Pennel, R., Siour, G., Tuccella, P., Turquety, S., and Valari, M. (2021). The CHIMERE v2020r1 online chemistry-transport model, *Geosci. Model Dev*., 14, 6781–6811, doi:10.5194/gmd-14-6781-2021.

Menut, L., Cholakian, A., Siour, G., Lapere, R., Pennel, R., Mailler, S., and Bessagnet, B. (2023). Impact of Landes forest fires on air quality in France during the 2022 summer, *Atmos. Chem. Phys*., 23, 7281–7296, https//doi.org/10.5194/acp-23-7281-2023.

Meredith, M., et al. (2019). Polar Regions. In: *IPCC Special Report on the Ocean and Cryosphere in a Changing Climate* [H.-O. Pörtner, D.C. Roberts, V. Masson-Delmotte, P. Zhai, M. Tignor, E. Poloczanska, K. Mintenbeck, A. Alegría, M. Nicolai, A. Okem, J. Petzold, B. Rama, N.M. Weye.

Methymaki, G., Bossioli, E., Boucouvala, D., Nenes, A., and Tombrou, M. (2023). Brown carbon absorption in the Mediterranean basin from local and long-range transported biomass burning air masses. *Atmos. Environ*., 306, 119822, https//doi.org/10.1016/j.atmosenv.2023.119822.

Mie, G. (1908). Beiträge zur Optik trüber Medien, speziell kolloidaler Metallösungen, *Ann. Phys*., 330, 377–445, https://doi.org/10.1002/andp.19083300302.

Mischenko, M., Travis, L. D., and Lacis, A. A. (2002). *Scattering, absorption and emission of light by small particles*, Cambridge, UK: Cambridge University Press.

Nenes, A., Pilinis, C., and Pandis, S. (1998). ISORROPIA: A new thermodynamic model for inorganic multicomponent atmospheric aerosols, *Aquatic Geochem*., 4, 123–152, https//doi.org/10.1023/A:1009604003981.

Moise, T., Flores, J. M., and Rudich, Y. (2025). Optical Properties of Secondary Organic Aerosols and Their Changes by Chemical Processes, *Chem. Rev.*, 115, 4400–4439, https://doi.org/10.1021/cr5005259.

Park, R. J., Jacob, D. J., Chin, M., and Martin, R. V. (2003). Sources of carbonaceous aerosols over the United States and implications for natural visibility, *J. Geophys. Res*., 108, 4355, https://doi.org/10.1029/2002JD003190.

Palacios-Peña, L., Jiménez-Guerrero, P., Baró, R., Balzarini, A., Bianconi, R., Curci, G., Landi, T. C., Pirovano, G., Prank, M., Riccio, A., Tuccella, P., and Galmarini, S. (2019). Aerosol optical properties over Europe: an evaluation of the AQMEII Phase 3 simulations against satellite observations, *Atmos. Chem. Phys.*, 19, 2965–2990, https://doi.org/10.5194/acp-19-2965-2019.

Potter, S., Copperdock, S., Veraverbeke, S., Walker, X., Mack, M.C., Goetz, S. J., Baltzer, J., Bourgeau-Chevez, L., Burrel, A., Dieleman, C., French, N., Hantson, S., Hoy, E. E., Jenkins, L., Johnstone, J. F., Kane, E. S., Natali, S. M., Randerson, J. T., Turetsky, M. R., Whitman, E. Wiggins, E., and Rogers, B. M. (2023). Burned area and carbon emissions across northwestern boreal North America from 2001–2019. *Biogeosciences*, 20(13), 2785-2804, https://doi.org/:10.5194/bg-20-2785-2023.

Price, C., and Rind, D. (1993). What determines the cloud-to-ground lightning fraction in thunderstorms?, *Geophys. Res. Lett.*, 20, 463– 466, https://doi.org/10.1029/93GL00226.

Park, R. J., Kim, M. J., Jeong, J. I, Youn, D., and Kim, S. (2010). A contribution of brown carbon aerosol to the aerosol light absorption and its radiative forcing in East Asia. *Atmos. Environ*., 44, 1414–1421, https://doi.org/10.1016/j.atmosenv.2010.01.042.

Ramnarine, E., Kodros, J. K., Hodshire, A. L., Lonsdale, C. R., Alvarado, M. J., and Pierce, J. R. (2019). Effects of near-source coagulation of biomass burning aerosols on global predictions of aerosol size distributions and implications for aerosol radiative effects. *Atmos. Chem. Phys*., 19, 6561-6577, https://doi.org/10.5194/acp-19-6561-2019.

Randerson, J. T. et al. (2006). The Impact of Boreal Forest Fire on Climate Warming. *Science*, 314, 1130-1132, DOI:10.1126/science.1132075.

Rathod, T. D., Sahu, S. K., Tiwari, M., Bhangare, R.C., and Ajmal, P.Y. (2021). Light absorption enhancement due to mixing in black carbon and organic carbon generated during biomass burning. *Atmos. Pollut. Res*., 12, 101236, https://doi.org/10.1016/j.apr.2021.101236.

Riemer, N., Ault, A. P., West, M., Craig, R. L., & Curtis, J. H. (2019). Aerosol mixing state: Measurements, modeling, and impacts. *Reviews of Geophysics*, 57, 187–249. https://doi.org/10.1029/2018RG000615.

Romshoo, B., Pöhlker, M., Wiedensohler, A., Pfeifer, S., Saturno, J., Nowak, A., Ciupek, K., Quincey, P., Vasilatou, K., Ess, M. N., Gini, M., Eleftheriadis, K., Robins, C., Gaie-Levrel, F., and Müller, T. (2022). Importance of size representation and morphology in modelling optical properties of black carbon: comparison between laboratory measurements and model simulations, *Atmos. Meas. Tech*., 15, 6965–6989, https://doi.org/10.5194/amt-15-6965-2022.

Saleh, R., Robinson, E. S., Tkacik, D. S., Ahern, A. T., Liu, S., Aiken, A. C., Sullivan, R., C., Presto, A. A., Dubey, M. K., Yokelson, R. J., Donahue, N. M., and Robinson, A. L. (2014). Brownness of organics in aerosols from biomass burning linked to their black carbon content, *Nat. Geosci.*, 7, 647–650, https://doi.org/10.1038/ngeo2220.

Saleh, R., Marks, M., Heo, J., Adams, P. J., Donahue, N. M., and Robinson, A. L. (2015). Contribution of brown carbon and lensing to the direct radiative effect of carbonaceous aerosols from biomass and biofuel burning emissions, *J. Geophys. Res.-Atmos*., 120, 10285–10296, https://doi.org/10.1002/2015JD023697.

Schnitzler, E. G., Liu, T., Hems, R. F., and Abbatt, J. P. D. (2020). Emerging investigator series: heterogeneous OH oxidation of primary brown carbon aerosol: effects of relative humidity and volatility. *Environ. Sci.-Proc. Imp.*, 22, 2162–2171, https://doi.org/10.1039/D0EM00311E.

Schwarz, J. P., Gao, R. S., Spackman, J. R., Watts, L. A., Thomson, D. S., Fahey, D. W., Ryerson, T. B., Peischl, J., Holloway, J. S., Trainer, M., Frost, G. J., Baynard, T., Lack, D. A., de Gouw, J. A., Warneke, C., and Del Negro, L. A. (2008). Measurement of the mixing state, mass, and optical size of individual black carbon particles in urban and biomass burning emissions, *Geophys. Res. Lett.*, 35, L13810, https://doi.org/10.1029/2008GL033968.

Seinfeld, J. N., and Pandis, S. N. (2016). *Atmospheric Chemistry and Physics: From Air Pollution to Climate Change*. 3th Edition, New York, US: John Wiley & Sons.

Sinyuk, A., Holben, B. N., Eck, T. F., Giles, D. M., Slutsker, I., Korkin, S., Schafer, J. S., Smirnov, A., Sorokin, M., and Lyapustin, A. (2020). The AERONET Version 3 aerosol retrieval algorithm, associated uncertainties and comparisons to Version 2, *Atmos. Meas. Tech.*, 13, 3375–3411, https://doi.org/10.5194/amt-13-3375-2020.

Sofiev, M., Ermakova, T., and Vankevich, R. (2012). Evaluation of the smoke-injection height from wild-land fires using remote-sensing data. *Atmos. Chem. Phys.*, 12, 1995–2006, https://doi.org/10.5194/acp-12-1995-2012.

Soulie, A., Granier, C., Darras, S., Zilbermann, N., Doumbia, T., Guevara, M., Jalkanen, J.-P., Keita, S., Liousse, C., Crippa, M., Guizzardi, D., Hoesly, R., and Smith, S. J. (2024). Global anthropogenic emissions (CAMS-GLOB-ANT) for the Copernicus Atmosphere Monitoring Service simulations of air quality forecasts and reanalyses, *Earth Syst. Sci. Data*, 16, 2261–2279, https://doi.org/10.5194/essd-16-2261-2024.

Tanré, D., Kaufman, Y. J., Herman, M., and Mattoo, S. (1997). Remote sensing of aerosol properties over oceans using the MODIS/EOS spectral radiances. *J. Geophys. Res*., 102(D14), 16971–16988, https://doi.org/10.1029/96JD03437.

Thompson, G., Field, P. R., Rasmussen, R. M., and Hall, W. D. (2008). Explicit Forecasts of Winter Precipitation Using an Improved Bulk Microphysics Scheme. Part II: Implementation of a New Snow Parameterization. *Mon. Weather Rev.*, 136(12), 5095-5115, https://doi.org/10.1175/2008MWR2387.1.

Toon, O. B., and Ackerman, T. P. (1981) Algorithms for the calculation of scattering by stratified spheres. *Appl. Opt*., 20, 3657–3660, https://doi.org/10.1364/AO.20.003657.

Torres, O., Decae, R., Veefkind, J. P., and de Leeuw, G. (2002). *OMI aerosol retrieval algorithm, in OMI Algorithm Theoretical Basis Document: Clouds, Aerosols, and Surface UV Irradiance, vol. 3, version 2* (ATBD-OMI-03, pp. 47–71) NASA Goddard Space Flight Cent., Greenbelt, Md. (Available at https://eospso.nasa.gov/sites/default/files/atbd/ATBD-OMI-03.pdf)

Torres, O., A. Tanskanen, B. Veihelmann, C. Ahn, R. Braak, P. K. Bhartia, P. Veefkind, and P. Levelt (2007). Aerosols and surface UV products from Ozone Monitoring Instrument observations: An overview. *J. Geophys. Res.*, 112, D24S47, doi:10.1029/2007JD008809.

Torres, O., Ahn, C., and Chen, Z. (2013). Improvements to the OMI near-UV aerosol algorithm using A-train CALIOP and AIRS observations, *Atmos. Meas. Tech.*, 6, 3257–3270, https://doi.org/10.5194/amt-6-3257-2013.

Tuccella, P., Thomas, J. L., Law, K. S., Raut, J.-C., Marelle, L., Roiger, A., Weinzierl, B., Denier van der Gon, H. A. C., Schlager, H., and Onishi, T. (2017). Air pollution impacts due to petroleum extraction in the Norwegian Sea during the ACCESS aircraft campaign, *Elem. Sci. Anth.*, 5, 25, https://doi.org/10.1525/elementa.124.

Tuccella, P., Menut, L., Briant, R., Deroubaix, A., Khvorostyanov, D., Mailler, S., Siour, G., and Turquety, S. (2019). Implementation of Aerosol-Cloud Interaction within WRF-CHIMERE Online Coupled Model: Evaluation and Investigation of the Indirect Radiative Effect from Anthropogenic Emission Reduction on the Benelux Union. *Atmosphere*, 10(1), 20, https://doi.org/10.3390/atmos10010020.

Tuccella, P., Curci, G., Pitari, G., Lee, S., and Jo, D. S. (2020). Direct radiative effect of absorbing aerosols: sensitivity to mixing state, brown carbon and dust refractive index and shape, *J. Geophys. Res.*, 125, e2019JD030967, https://doi.org/10.1029/2019JD030967.

Tuccella, P., Pitari, G., Colaiuda, V., Raparelli, E., and Curci, G. (2021). Present-day radiative effect from radiation-absorbing aerosols in snow, *Atmos. Chem. Phys*., 21, 6875–6893, https://doi.org/10.5194/acp-21-6875-2021.

Updyke, K. M., Nguyen, T. B., and Nizkorodov, S. A. (2012). Formation of brown carbon via reactions of ammonia with secondary organic aerosols from biogenic and anthropogenic precursors, *Atmos. Env*, 63, 22–31, https://doi.org/10.1016/j.atmosenv.2012.09.012.

van Bellen S., Garneau, M., and Bergeron, Y. (2010). Impact of Climate Change on Forest Fire Severity and Consequences for Carbon Stocks in Boreal Forest Stands of Quebec, Canada: a Synthesis. *Fire Ecol*., 6, 16-44, https://doi.org/10.4996/fireecology.0603016.

Veira, A., Kloster, S., Wilkenskjeld, S., and Remy, S. (2015). Fire emission heights in the climate system – Part 1: Global plume height patterns simulated by ECHAM6-HAM2, *Atmos. Chem. Phys.*, 15, 7155–7171, https://doi.org/10.5194/acp-15-7155-2015.

Veraverbeke, S. et al. (2017). Lightning as a major driver of recent large fire years in North American boreal forests. *Nature Climate Change*, 7 (7), 529–534, doi:10.1038/nclimate3329.

Walker J.X., Rogers, B. M., Baltzer, J. L., Cumming, S. G., Day, N. J., Goetz, S. J., Johnstone, J. F., Schuur, E. A. G., Turetsky, M. R., and Mack M. C. (2018). Cross-scale controls on carbon emissions from boreal forest megafires, *Glob. Change. Biol*., 24(9), 4251-4265, https://doi.org/10.1111/gcb.14287.

Wang, X., Heald, C. L., Ridley, D. A., Schwarz, J. P., Spackman, J. R., Perring, A. E., Coe, H., Liu, D., and Clarke, A. D. (2014). Exploiting simultaneous observational constraints on mass and absorption to estimate the global direct radiative forcing of black carbon and brown carbon, *Atmos. Chem. Phys*., 14, 10989–11010, https://doi.org/10.5194/acp-14-10989-2014.

Wang, X., Zhang, L., and Moran, M. D. (2014). Development of a new semi-empirical parameterization for below-cloud scavenging of size-resolved aerosol particles by both rain and snow, *Geosci. Model Dev*., 7, 799–819, https://doi.org/10.5194/gmd-7-799-2014.

Wang, X., Heald, C. L., Sedlacek, A. J., de Sá, S. S., Martin, S. T., Alexander, M. L., Watson, T. B., Aiken, A. C., Springston, S. R., and Artaxo, P. (2016). Deriving brown carbon from multiwavelength absorption measurements: method and application to AERONET and Aethalometer observations, *Atmos. Chem. Phys*., 16, 12733–12752, https://doi.org/10.5194/acp-16-12733-2016.

Wang, X., Heald, C. L., Liu, J., Weber, R. J., Campuzano-Jost, P., Jimenez, J. L., Schwarz, J. P., and Perring, A. E. (2018). Exploring the observational constraints on the simulation of brown carbon, *Atmos. Chem. Phys*., 18, 635–653, https://doi.org/10.5194/acp-18-635-2018.

Wang, Y., Li, W., Huang, J., Liu, L., Pang, Y., He C., He, C., Liu, F., Liu, D., Bi, L., Zhang, X., and Shi, Z. (2021). Nonlinear enhancement of radiative absorption by black carbon in response to particle mixing structure. *Geophys. Res. Lett*., 48, e2021GL096437, https://doi.org/10.1029/2021GL096437.

Wang, J., Wang, J., Cai, R., Liu, C., Nie, W., Wang, J., Moteki, N., Zaveri, R. A., Huang, X., Ma, N., Chen, G., Wang, Z., Jin, Y., Cai, J., Zhang, Y., Chi, X., Holanda, B. A., Xing, J., Liu, T., Qi, X., Wang, Q., Pöhlker, C., Su, H., Cheng, Y., Wang, S., Hao, J., Andreae, M. O., and Ding, A. (2023). Unified theoretical framework for black carbon mixing state allows greater accuracy of climate effect estimation, N*at. Commun*., 14, 2703, , 2023.https://doi.org/10.1038/s41467-023-38330-x.

Wesely, M. (1989). Parameterization of Surface Resistances to Gaseous Dry Deposition in Regional-Scale Numerical Models, *Atmos. Environ*., 23, 1293–1304, https://doi.org/10.1016/0004-6981(89)90153-4.

Wild, O., Zhu, X., Prather, and Fast-J, M. J. (2000). Accurate Simulation of In- and Below-Cloud Photolysis in Tropospheric Chemical Models. *J. Atmos. Chem*., 37, 245–282, https://doi.org/10.1023/A:1006415919030.

Zeng, L., Tan, T., Zhao, G., Du, Z., Hu, S., Shang, D., and Hu, M. (2024). Overestimation of black carbon light absorption due to mixing state heterogeneity. *npj Clim. Atmos. Sci*., 7, 2, https://doi.org/10.1038/s41612-023-00535-8.

Zhang, L., Gong, S., Padro, J., and Barrie, L. (2001). A size-segregated particle dry deposition scheme for an atmospheric aerosol module. *Atmos. Environ*., 35(3), 549–560, https://doi.org/10.1016/S1352-2310(00)00326-5.

Zhang, Y., Forrister, H., Liu, J., Dibb, J., Anderson, B., Schwarz, J. P., Perring, A. E., Jimenez, J. L., Campuzano-Jost, P., Wang, Y., Nenes, A., and Weber R.W. (2017). Top-of-atmosphere radiative forcing affected by brown carbon in the upper troposphere. *Nat. Geosci*., 10, 486–489, https://doi.org/10.1038/ngeo2960, 2017.

Zhang, A., Wang, Y., Zhang, Y., Weber, R. J., Song, Y., Ke, Z., and Zou, Y. (2020). Modeling the global radiative effect of brown carbon: a potentially larger heating source in the tropical free troposphere than black carbon. *Atmos. Chem. Phys*., 20, 1901–1920, https://doi.org/10.5194/acp-20-1901-2020.

Zhao, R., Lee, A. K. Y., Huang, L., Li, X., Yang, F., and Abbatt, J. P. D. (2015). Photochemical processing of aqueous atmospheric brown carbon, *Atmos. Chem. Phys.*, 15, 6087–6100, https://doi.org/10.5194/acp-15-6087-2015.

Zhao, G., Tan, T., Zhu, Y., Hu, M., and Zhao, C. (2021). Method to quantify black carbon aerosol light absorption enhancement with a mixing state index. *Atmos. Chem. Phys*., 21, 18055–18063, https://doi.org/10.5194/acp-21-18055-2021.

Zhong, M., and Jang, M. (2014). Dynamic light absorption of biomass-burning organic carbon photochemically aged under natural sunlight. *Atmos. Chem. Phys*., 14, 1517–1525, https://doi.org/10.5194/acp-14-1517-2014.

Tables

Table 1. Summary of the numerical experiments.

Simulation	Description
CTRL	Control simulation. Default model.
BC_{Eabs}	Only BC absorption enhancement
BEST	BC absorption enhancement and BrC absorption
H-ABS	High absorption scenario: E_{absCS}=1.9, no BB-BrC ageing
L-ABS	Low absorption scenario: E_{absCS}=1.2, all BB-BrC is aged

Table 2. Statistical comparison of the predicted and observed AOD with MODIS at 550 nm, OMI at 354 nm, and AERONET stations at 440 nm.

Database	r	NMB (%)	RMSE	NSE	TS	STDE
MODIS[1]	0.77	-14	0.17	0.57	0.79	0.16
OMI[1]	0.65	-30	0.64	0.35	0.70	0.60
AERONET[2,3]	0.79	-23	0.22	0.58	0.88	0.21
AERONET-R1[2]	0.78	-35	0.47	0.56	0.81	0.44
AERONET-R2[2]	0.77	-20	0.27	0.54	0.88	0.26
AERONET-R3[2]	0.76	-16	0.14	0.54	0.86	0.13

[1]*The comparison is done with monthly average*

[2]*The comparison is done with daily data*

[3]*This comparison is done with all AERONET data*

Table 3. Statistical comparison of the predicted monthly AAOD at 354 nm in CTRL, BC_{Eabs}, and BEST simulations with that and observed by OMI.

Simulation	r	NMB (%)	RMSE	NSE	TS	STDE
CTRL	0.53	-78	0.059	-0.32	0.34	0.044
BC_{Eabs}	0.54	-75	0.058	-0.25	0.41	0.044
BEST	0.50	-55	0.055	-0.14	0.73	0.049

Table 4. Total aerosol and BB average AAOD at 550 nm for June 2023, calculated CTRL and BEST simulations.

	CTRL	BEST	UNCERTAINTY[1]
AAOD	0.0068	0.0089	0.0080/0.0110 (-10/+24%)
BB-AAOD	0.0047	0.0066	0.0057/0.0086 (-14/+30%)

[1]*The uncertainty has been assessed relative to BEST simulation, using L-ABS and H-ABS sensitivity tests.*

Table 5. June 2023 average clear-sky and all-sky TOA DRE (W/m2) of BB calculated from CTRL and BEST simulations.

	CTRL	BEST	UNCERTAINTY[1]
Clear-sky	-3.1	-2.8	-3.0/-2.6 (±7%)
All-sky	-2.1	-1.9	-2.0/-1.8 (±5%)

[1]*The uncertainty has been assessed relative to BEST simulation, using L-ABS and H-ABS sensitivity tests.*

Figures

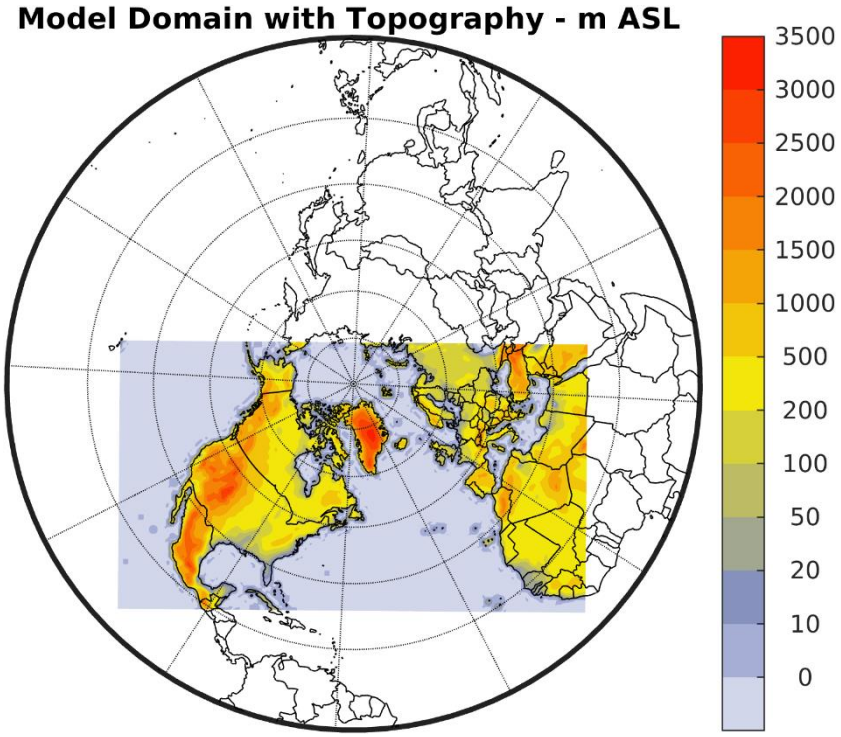

Figure 1: The domain used to run WRF-CHIMERE. The grid had horizontal resolution of 78 km with 189x109 grid points.

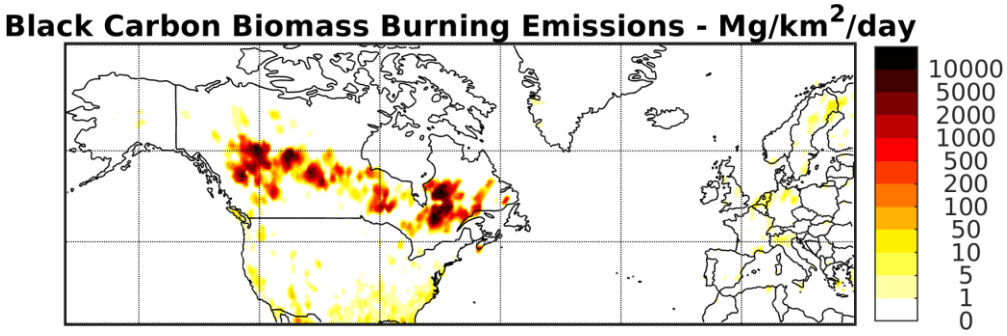

Figure 2: Biomass burning emission flux of black carbon during the month of June 2023 obtained from the CAMS database.

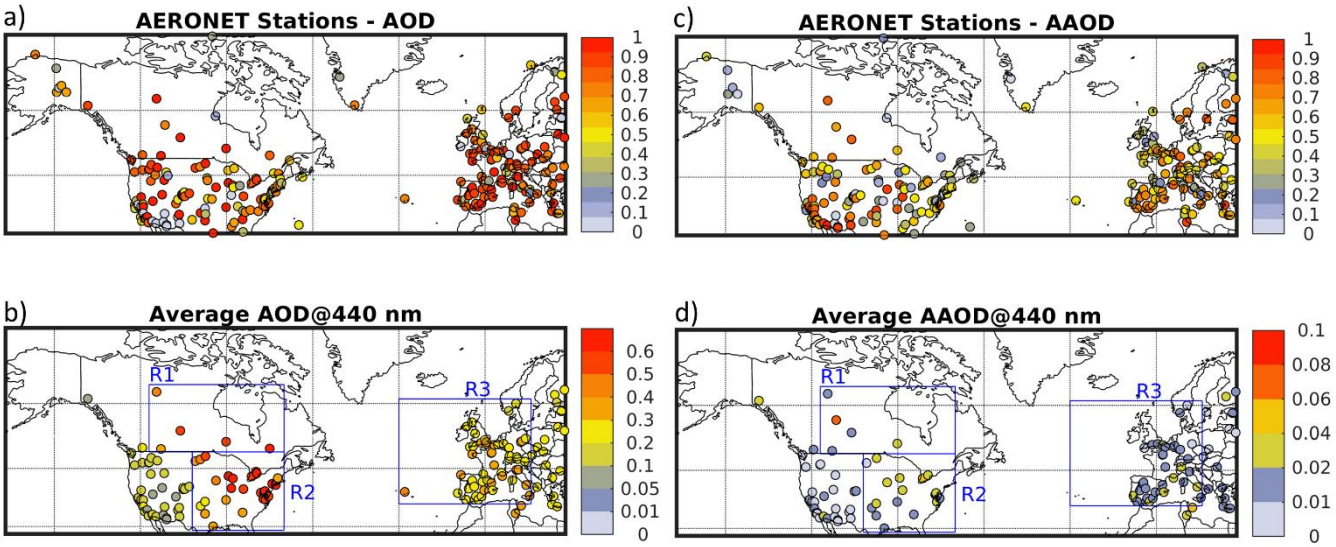

Figure 3: AERONET stations used to evaluate the model simulations. The colour scale represents the fraction of data coverage in June 2023 for the aerosol optical depth (AOD) (a) and the absorption aerosol optical depth (AAOD) (c), and the mean AOD (b) and AAOD (d) at 440 nm measured at AERONET sites. Average AOD is calculated at the stations with at least 75% of monthly data coverage, while monthly AAOD is calculated at sites with at least 55% of data coverage. The regions R1, R2, and R3 outlined by blue rectangles indicate the area most affected by Canadian boreal fires (see Section 2.5).

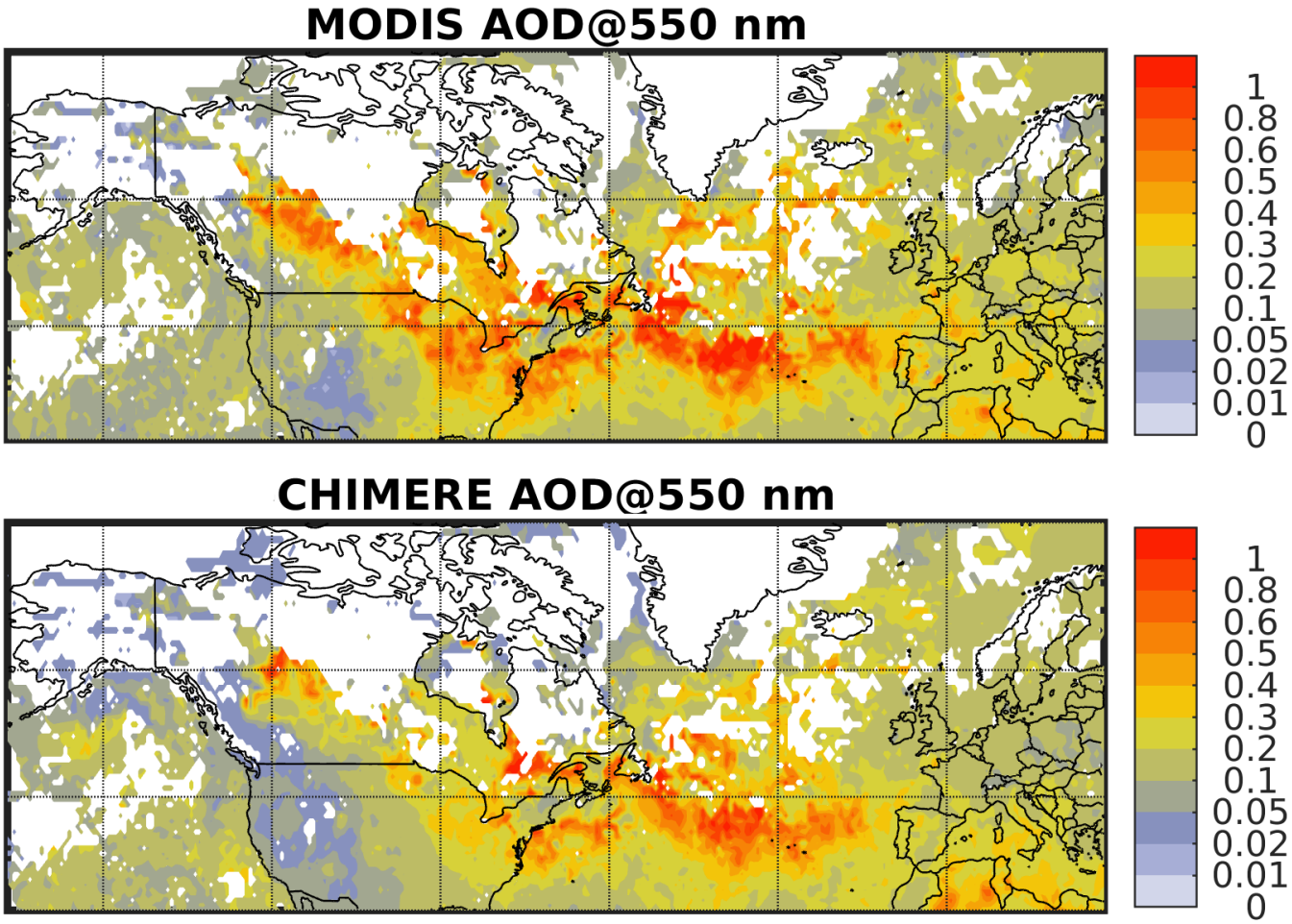

Figure 4: Aerosol optical depth (AOD) monthly average at 550 nm for June 2023, as measured by MODIS (upper panel) and modelled by CHIMERE (lower panel).

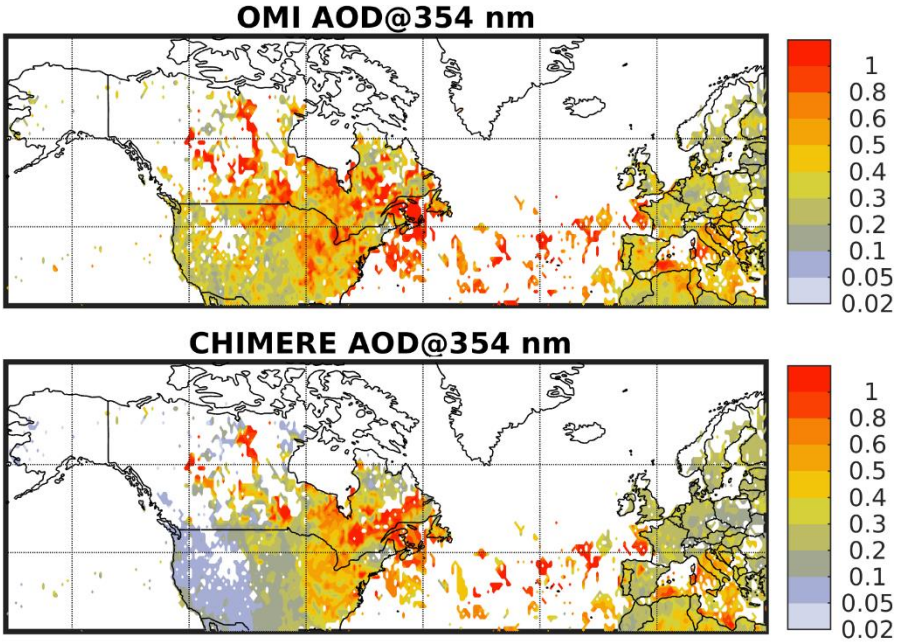

Figure 5: As in Figure 4, but for AOD at 354 nm measured by OMI.

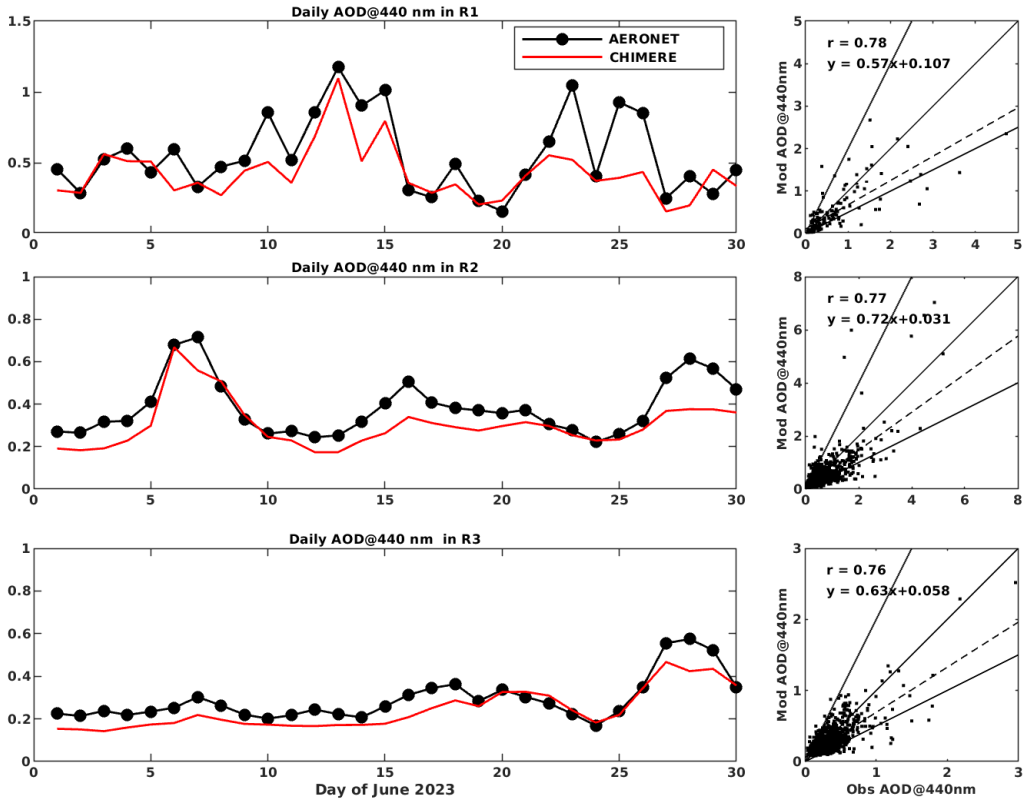

Figure 6. Comparison of modelled and observed aerosol optical depth (AOD) at 440 nm at AERONET sites. The left panels show the predicted and measured daily time series of AOD, averaged across all stations in regions R1, R2, and R3. The right panels present the scatter plots of observed versus predicted daily AOD in R1, R2, and R3. The lines 1:1, 2:1, and best least-squares linear fit shown for reference.

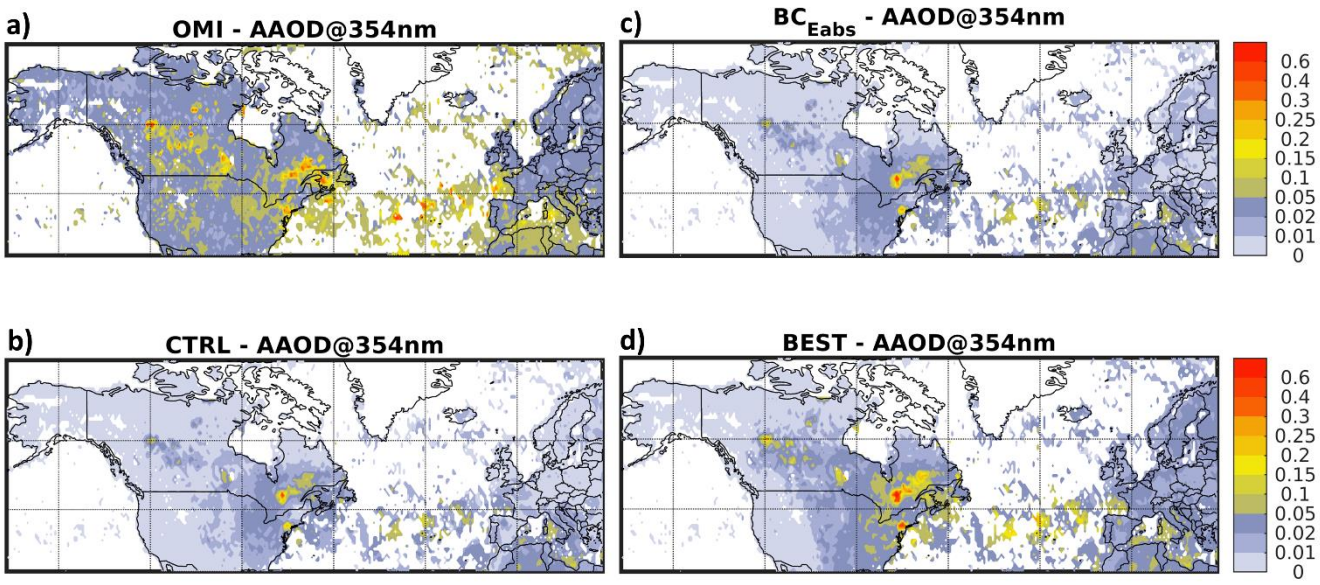

Figure 7: June 2023 monthly average absorption aerosol optical depth (AAOD) at 354 nm, a) as measured by OMI and modelled by CHIMERE in b) CTRL, c) BC_{Eabs}, and d) BEST simulations.

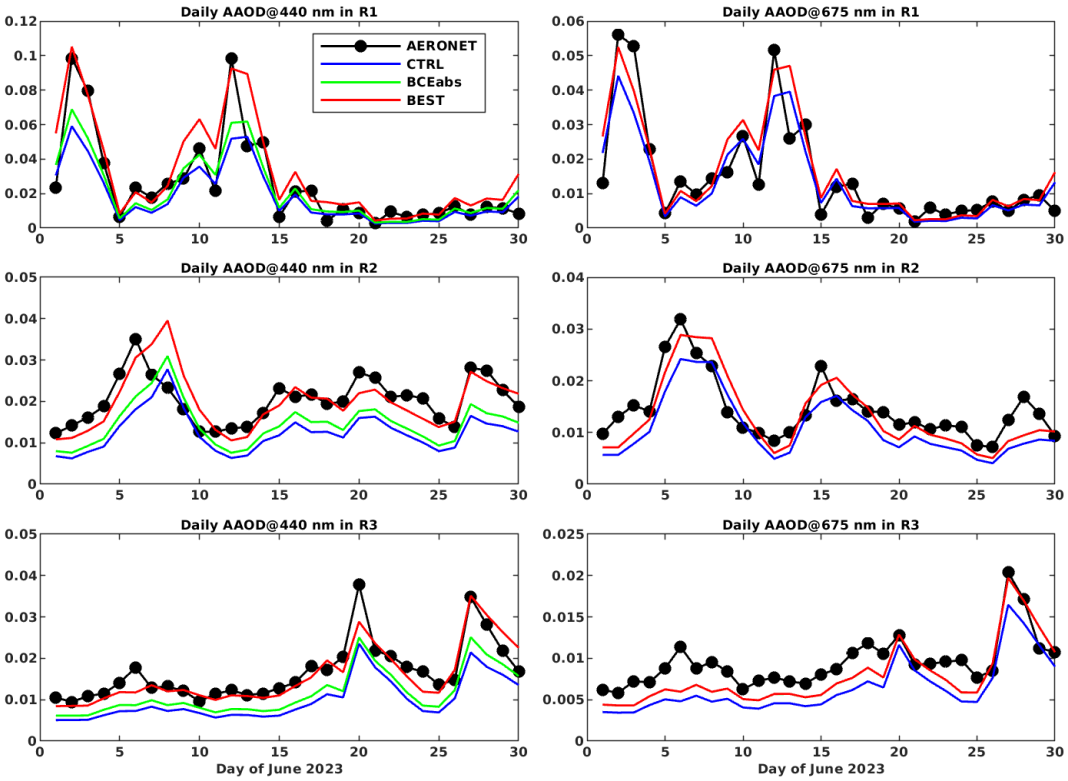

Figure 8. Comparison observed and modelled average time series of absorption aerosol optical depth (AAOD) at 440 (left panels) and 675 nm (right panels), for the CTRL (blue), BC_{Eabs} (green), and BEST (red) simulations at AERONET sites in regions R1, R2, and R3. Please, note that at 675 nm BC_{Eabs}, and BEST give the same results, since BrC is not absorbing at this wavelength.

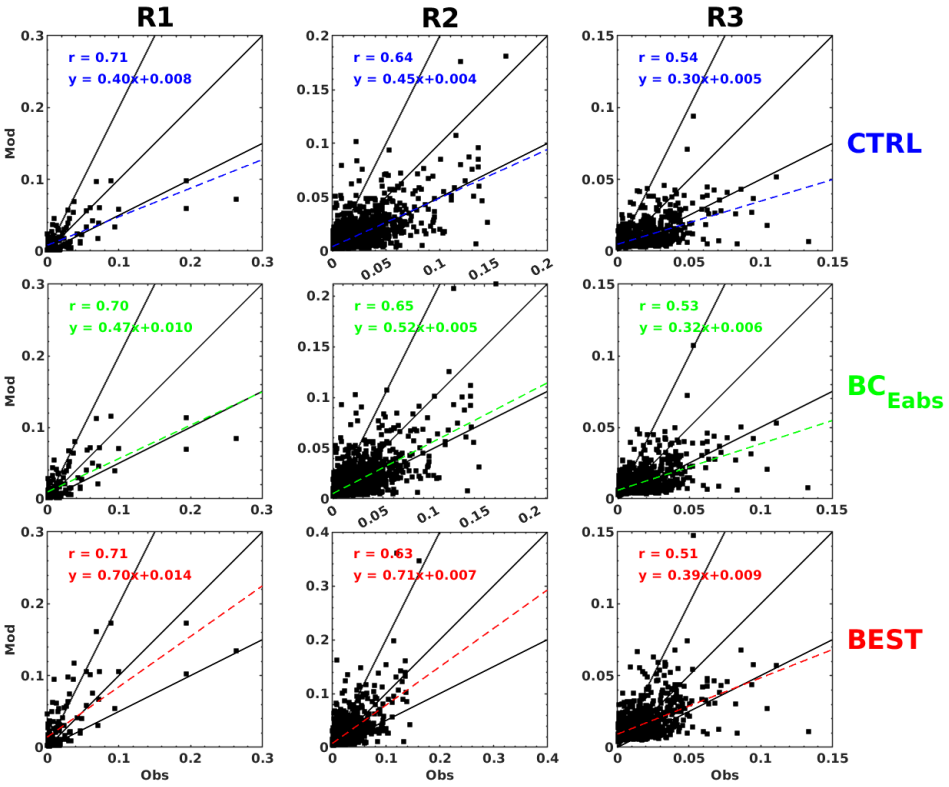

Figure 9. Scatter plots of observed and modelled daily absorption aerosol optical depth (AAOD) at 440 nm, for the CTRL, BC_{Eabs}, and BEST simulations at AERONET sites in regions R1, R2, and R3. The lines 1:1, 2:1, and best least-squares linear fit shown for reference.

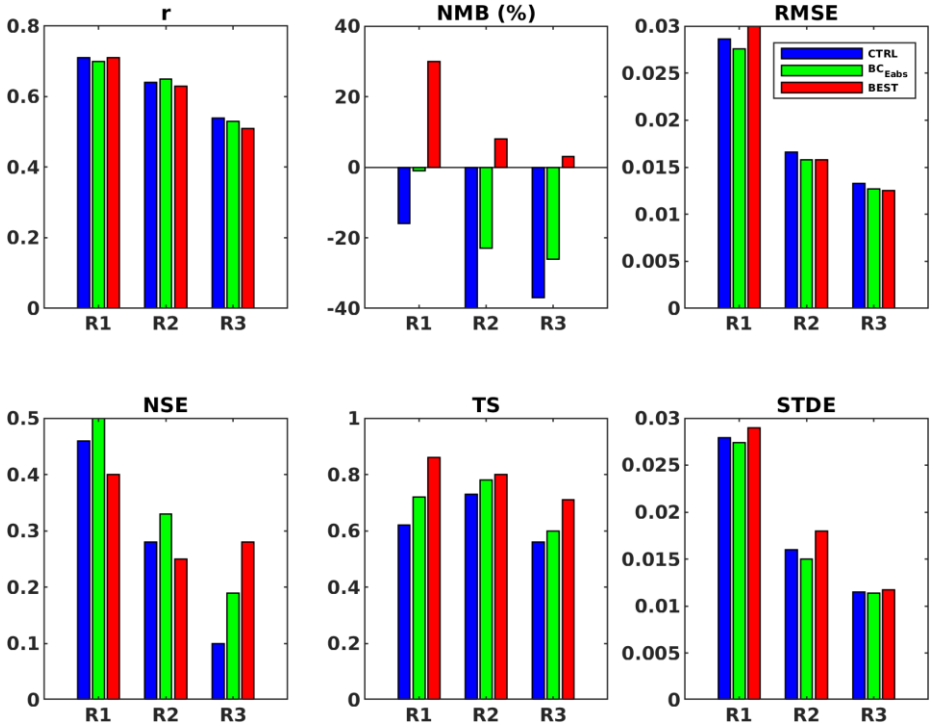

Figure 10. Statistical summary of the comparison of observed and modelled daily absorption aerosol optical depth (AAOD) at 440 nm, for the CTRL, BC_{Eabs}, and BEST simulations, at AERONET sites in regions R1, R2, and R3.

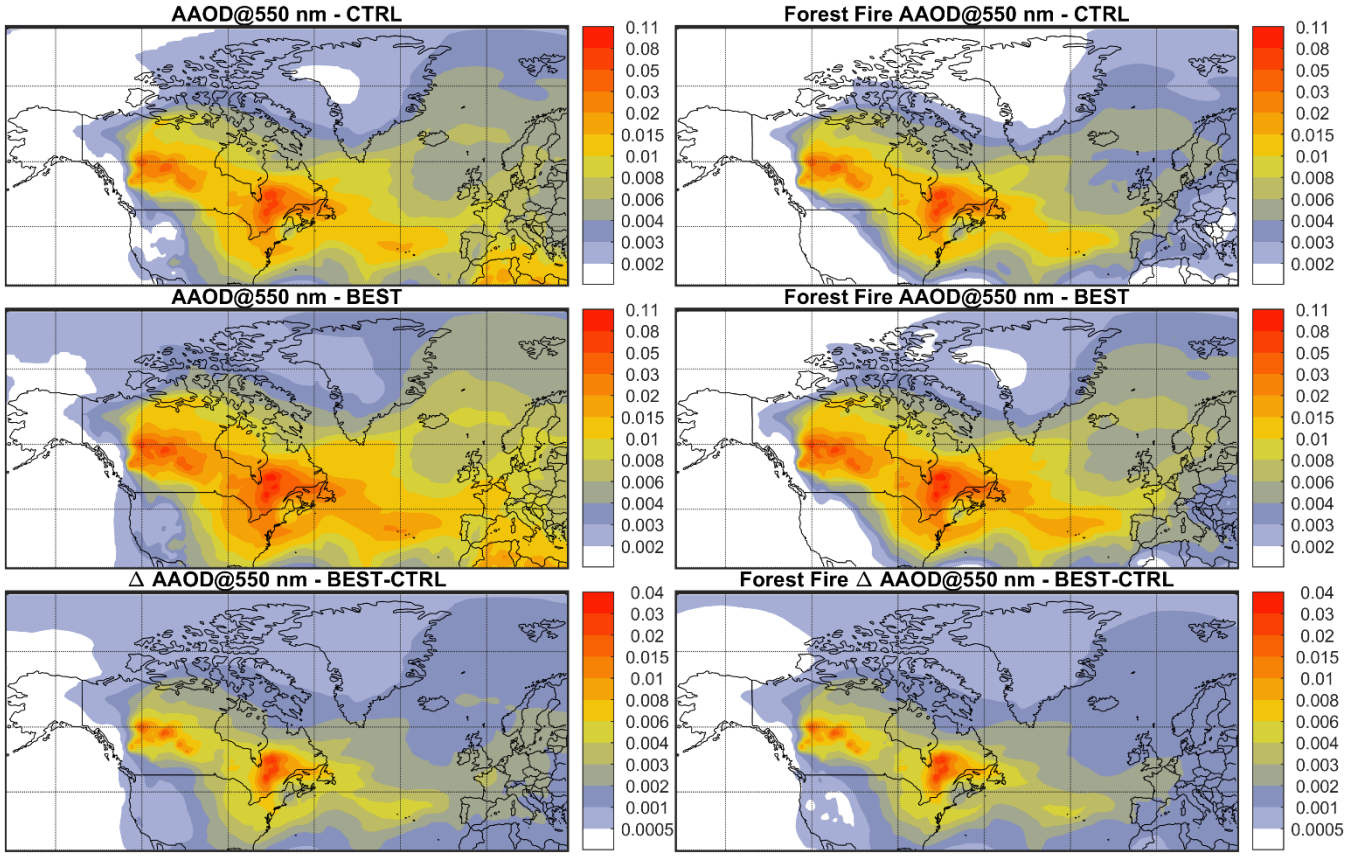

Figure 11. Mean total (left panels) and biomass burning (BB, right panels) absorption aerosol optical depth (AAOD) at 550 for June 2023, calculated by the CTRL (upper panels) and BEST (middle panels) models, and their difference (lower panels).

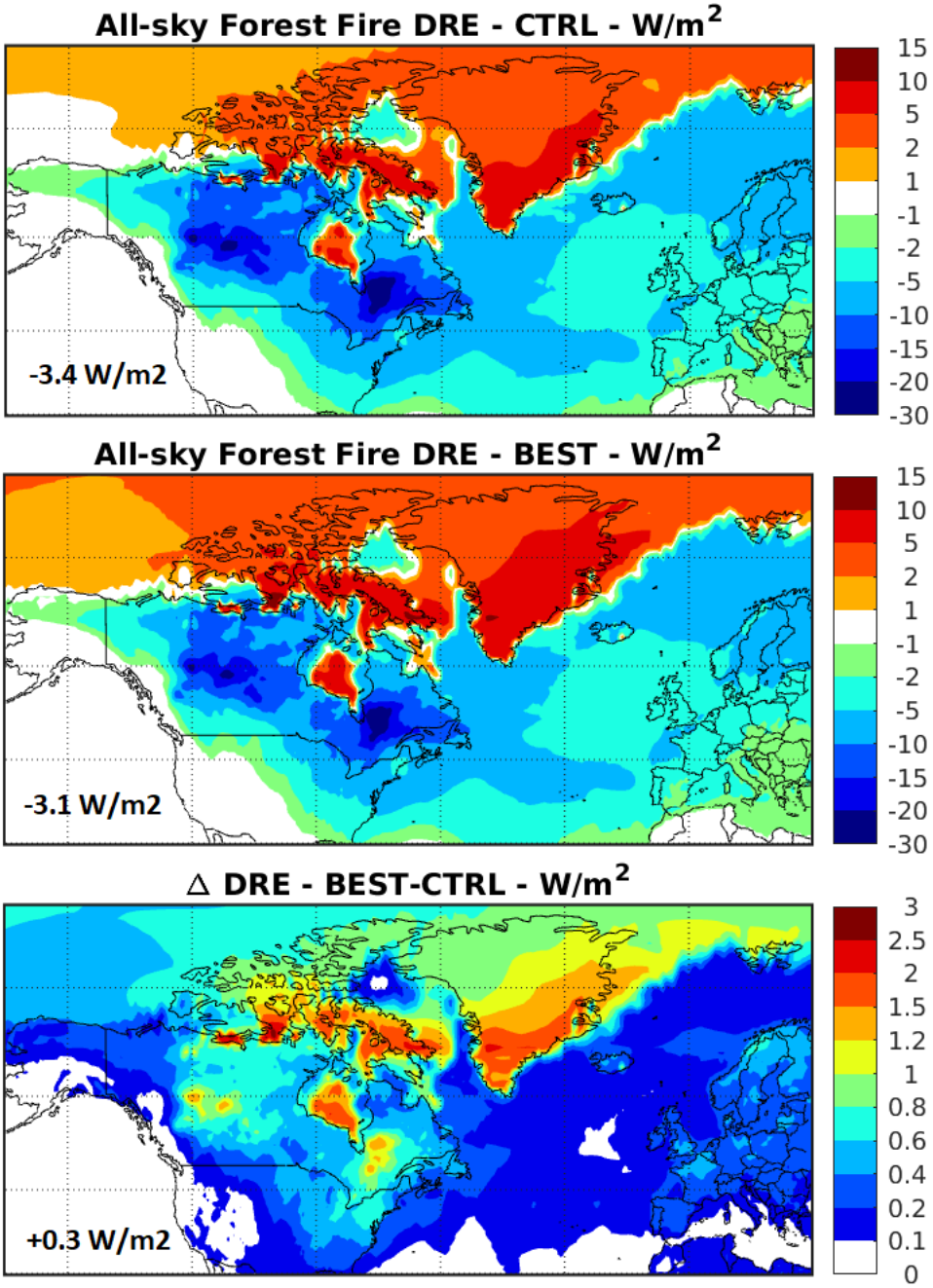

Figure 12. Mean all-sky DRE of biomass burning aerosols at top of the atmosphere (TOA) for June 2023, calculated by the CTRL (upper panel) and BEST (middle panel) models, and their difference (lower panel).

Modelling the black and brown carbon absorption and their radiative impact: the June 2023 intense Canadian boreal wildfires case study

Paolo Tuccella[1,2], Ludovico Di Antonio[3,4], Andrea Di Muzio[1], Valentina Colaiuda[5], Laurent Menut[6], Giovanni Pitari[1], Edoardo Raparelli[1,2]

[1]Departement of Physical and Chemical Sciences, University of L'Aquila, 67010 L'Aquila, Italy.
[2]Center of Excellence in Telesensing of Environment and Model Prediction of Severe Events (CETEMPS), University of L'Aquila, Italy.
[3]Univ. Paris Est Creteil, Université Paris Cité, CNRS, LISA, F-94010 Créteil, France.
[4]Laboratoire, Atmosphères, Observations Spatiales (LATMOS)/IPSL, Sorbonne Université, UVSQ, CNRS, Paris, France
[5]Abruzzo Region Civil Protection Agency, L'Aquila, Italy.
[6]LMD/IPSL, École Polytechnique, Institut Polytechnique de Paris, ENS, PSL Research University, Sorbonne Université, CNRS, Palaiseau, France

Correspondence to Paolo Tuccella: paolo.tuccella@univaq.it

Key Points

- Enhanced modelling of black and brown carbon improved the simulation of aerosol absorption during the 2023 Canadian wildfires.
- Advanced modelling of black and brown carbon reduced the direct radiative effect of the wildfires by 10%, from -2.1 to -1.9 W/m².
- Accurate aerosol absorption representation is crucial for predicting the regional climate impact of large-scale biomass burning events.

Abstract

Black carbon (BC) and brown carbon (BrC) are light-absorbing aerosols with significant climate impacts, but their absorption properties and direct radiative effect (DRE) remain uncertain. We simulated BC and BrC absorption during the intense Canadian boreal wildfires in June 2023 using an enhanced version of CHIMERE model. The study focused on a domain extending from North America to Eastern Europe, including a significant portion of the Arctic up to 85°N.

The enhanced model includes an updated treatment for the BC absorption enhancement and a BrC ageing scheme accounting for both browning and blanching through oxidation. When compared to observations, the updated model accurately captured aerosol optical depth (AOD) at multiple wavelengths, both near the wildfires and during transoceanic transport to Europe. Improvements were observed in the simulation of absorbing aerosol optical depth (AAOD) compared to the control model.

The all-sky regional direct radiative effect (DRE) for June 2023 attributed to the intense Canadian wildfires, was reduced from -2.1 W/m² in the control model to -1.9 W/m² (-2.0/-1.8 W/m², ±5%), in the enhanced model, indicating an additional warming effect of +0.2 W/m² (about +10%) due to advanced schemes used for the BC and BrC absorption.

The results indicate the importance of an accurate simulation of aerosol absorption in regional climate predictions, especially during large-scale biomass burning events. They also suggest that traditional models could overestimate the cooling effect of boreal wildfires, highlighting the need for improvement of aerosol parameterization to better predict the DRE and develop effective mitigation strategies.

Plain Language Summary

Black carbon (BC) and brown carbon (BrC) are atmospheric particles that absorb sunlight and contribute to climate warming. BC is emitted from the incomplete combustion of fossil fuels, biomass, and biofuels, while BrC is primarily produced by wood burning. However, their exact climate impact remains uncertain. In this study, we used an improved version of the CHIMERE model to simulate BC and BrC absorption during the intense Canadian wildfires in June 2023. The model covered a vast area from North America to Eastern Europe, including parts of the Arctic.

We refined the model to more accurately calculate the BC light absorption and the BrC absorption changes over time (either increasing or decreasing). Comparing the model results with satellite and ground-based data, we found that the updated model more precisely captured the absorption spatial variability, particularly in regions affected by wildfire smoke.

The study showed that models lacking proper BC and BrC treatment may overestimate the cooling effect of wildfires. Our improved model reduced the estimated cooling from the 2023 Canadian wildfires by about 10%, emphasizing the importance of accurate modelling to predict the climate impacts of these increasingly frequent events driven by global warming.

1 Introduction

Black carbon (BC) and brown carbon (BrC) are recognized by the scientific community as light-absorbing aerosol particles influencing the climate through the direct (Haywood and Boucher, 2000) and semidirect (Hansen et al., 1997) effects, by darkening the surface after their deposition on the snow/ice pack (Flanner et al., 2007; Bond et al., 2013, Lin et al., 2014; Tuccella et al., 2021; Brown et al., 2022), and acting as cloud condensation nuclei for clouds they may modify the cloud optical properties and precipitation pattern through the indirect aerosol effects (Andreae et al., 2008). The effects of BC and BrC on the global and regional climate are uncertain (IPCC, 2021).

BC is formed through the incomplete combustion of fossil fuels (FF), biomass (BB), and biofuels (BF) (Bond et al., 2013). Soot particles exhibit a strong capacity to absorb incoming solar radiation (Bond et al., 2013). Current estimates suggest BC as the third most important contributor to global warming after carbon dioxide (CO_2) and methane (CH_4) (Bond et al., 2013; Gustafsson and Ramanathan, 2016; IPCC, 2021).

BC absorption is influenced by its mixing state (Curci et al., 2019; Tuccella et al., 2020). Mixing state refers to the distribution of chemical and physical properties within an aerosol population (Riemer et al., 2019). In an externally mixed state, different aerosol components exist as separate particles with distinct compositions. Conversely, internally mixed particles within an aerosol population consist of a homogeneous mixture of chemical species. In the real atmosphere, purely internal or external mixing states are not common (Bondy et al., 2018) and the mixing state continuously evolves due to processes governing the aerosol lifecycle. Freshly emitted BC particles usually have a fractal structure and are externally mixed with non-BC species. After emission, ageing processes lead to the formation of internally mixed particles, characterized by a core-shell structure where the BC core is coated by a shell composed of organic and inorganic compounds. The presence of the shell increases amplifies the BC absorption through the so called “lensing effect” (Jacobson, 2000, 2001; Lesins et al., 2002).

The absorption enhancement (E_{abs}) of coated BC is typically calculated with a Mie code for the core-shell structure (e.g., Toon and Ackerman, 1981). Several studies have demonstrated that this model is an oversimplification, since it does not consider the complex morphology of BC particles, with implications for absorption calculation (Adachi et al., 2010; Wang et al., 2021; Romshoo et al., 2022). In particular, the core-shell model overestimates the BC absorption enhancement (Adachi et al., 2010; Liu et al., 2017; Fierce et al., 2020; Wang et al., 2023). While some studies have observed a substantial increase in light absorption, others have reported a considerably lower E_{abs} compared to laboratory and modeling simulations (Cappa et al., 2012; Lack et al., 2012; Liu et al., 2017). Liu et al. (2017) demonstrated that E_{abs} is influenced by the mass ratio of non-BC to BC. Specifically, BC emitted from urban traffic, characterized by lower non-BC to BC mass ratios, is often better represented as externally mixed with no absorption enhancement. Moreover, the discrepancies of between observed and modelled differences have been also attributed to the particle-to-particle heterogeneity in the environment (Fierce et al., 2020; Zhao et al., 2021; Zeng et al., 2024). This highlights the importance of incorporating mixing state-dependent absorption parameterizations in atmospheric models to accurately predict the radiative effects of BC.

Brown carbon (BrC) is defined as the subset of organic aerosol that exhibits strong absorption (OA) (Andreae et al., 2006; Laskin et al., 2015) of shortwave radiation with wavelengths less than 400 nm (Lukacs et al., 2007; Alexander et al., 2008; Chen et al., 2010; Arola et al., 2011; Kirchstetter et al., 2012, Moise et al. 2015). BrC is mainly produced by BF combustion, BB, and ageing of secondary organic aerosol (SOA) (Bones et al., 2010; Hecobian et al., 2010; Arola et al., 2011; Updyke et al., 2012; Lambe et al., 2013; Lee et al., 2014; Laskin et al., 2015; Guang et al., 2016), while other sources are related to cloud chemistry (Zhang et al., 2017). The representation of OA optical properties in climate models has evolved over the past decade. From being considered as scattering particles, the BrC absorption is now included in many global (Wang et al., 2014; Lin et al., 2014; Saleh et al., 2015; Jo et al., 2016; Wang et al., 2018; Brown et al., 2018; Tuccella et al., 2020, 2021; Zhang et al., 2020; Drugé et al., 2022; DeLessio et al., 2024) and regional modelling studies (Methymaki et al., 2023; Kononalov et al., 2024).

Primary BrC absorption is not constant over time but varies with ageing processes that OA undergoes. Experimental results have suggested that BrC optical properties may be modified through aqueous-phase photochemical reactions, potentially leading to both photo-enhancement and photobleaching (Zhao et al., 2015). The increase of BrC absorption is called "browning" and it is primarily driven by heterogeneous oxidation reactions with hydroxyl (OH) and nitrate (NO_3) radicals, as well as aqueous oxidation (Cheng et al., 2020; Schnitzler et al., 2020; Hems et al., 2020). Following browning, BrC undergoes bleaching, a process attributed to oxidation by OH and ozone (O_3) (Hems et al., 2021).

While photobleaching is frequently incorporated into models simulating brown carbon (Wang et al., 2018; Brown et al., 2018; Zhang et al., 2020; Drugé et al., 2022), browning is often overlooked. To our knowledge, only DeLessio et al. (2024) have accounted for photo-enhancement in their study. The same authors concluded that accurate representation of the diurnal variability in OA absorption necessitates the inclusion of the browning process in the atmospheric models.

Many studies have demonstrated that wildfires impact the climate system (Randerson et al., 2006; Li et al., 2017; Walker et al., 2018; Eckdahl et al., 2022; Linares and Ni-Meister, 2024). At the same time, the frequency of wildfire events is increasing due to climate warming. The relationship between climate change and wildfire frequency has been studied since the early 1990s (van Bellen et al., 2010). The Arctic is warming at more than twice the global average rate (Meredith et al., 2019), which contributes to the rise of wildfire activity in boreal regions of Alaska and western Canada (Gillett, 2004; Veraverbeke et al., 2017). Moreover, the Northern Hemisphere has experienced extreme wildfire seasons, as for example the 2023 Canadian events (Byrne et al., 2024), leading to significant aerosol emissions, with notable impacts on aerosol properties even in Europe (Filonchyk and Peterson, 2024). Additionally, in the future, anthropogenic aerosol mitigation could be a significant driver in enhancing boreal forest fires (Allen et al., 2024).

Boreal forest fires are important sources of BC and OA, which may exert significant regional climate feedback at regional scale (Konovalov et al., 2024a; 2024b). Accurate prediction of BC and OA absorption properties is essential for estimating the climatic impact of boreal wildfires.

This study provides a comprehensive assessment of BC and BrC absorption during the 2023 Canadian boreal wildfires using an enhanced parametrisation within the CHIMERE model. The results underscore the critical role of aerosol absorption modelling for an accurate prediction of the regional

direct radiative effect (DRE), associated to large-scale wildfire events. In Section 2, we detailed the model description and setup, where we included a treatment for improving the BC absorption and a treatment for BrC absorption, including an update parameterization for BC E_{abs} and a treatment for BrC absorption, accounting for both browning and blanching processes. In Section 3, the simulated optical properties have been evaluated against satellite and ground-based observations. Finally, in Section 4, we discussed the DRE of the June 2023 Canadian smoke aerosol.

2 Methods

2.1 CHIMERE model description and setup

In this study, we have used the 2021 version of the CHIMERE model (Menut et al., 2021) to simulate the absorption of BC and BrC, coupled online with the meteorological Weather Research and Forecasting (WRF) model. This online configuration is capable to simulate both direct (Briant et al., 2017) and indirect aerosol effects (Tuccella et al., 2019). The WRF model is a mesoscale meteorological model including several parameterizations for atmospheric processes (https://www.mmm.ucar.edu/models/wrf, last access: 09 October 2024). CHIMERE is a chemical and transport model suitable for studies ranging from hemispheric to urban scales (Mailler et al., 2017). It contains multiple numerical schemes for simulating the gas-phase and aerosol processes. WRF and CHIMERE are coupled with the external coupler OASIS3-MCT (Craig et al., 2017). The information between models is exchanged with a regular frequency defined by the user (Briant et al., 2017).

We simulated the entire month of June 2023, after a one-month of spin-up for chemistry. WRF-CHIMERE was configured on the domain shown in Figure 1. This domains spans from North America to Eastern Europe, in latitude it extends from Tropics up to North Pole. The horizontal resolution was of 78 km, with 190 x 127 grid points. We used 33 vertical levels extending from surface up to 50 hPa for WRF, and 30 levels up to 200 hPa for CHIMERE. The coupling time (i.e., exchange frequency) between WRF and CHIMERE was fixed at 20 minutes.

Main parameterizations adopted for WRF are the YSU for planetary boundary layer (Hong et al.,2006), NOAH as land surface model (Chen and Dudhia, 2001), RRTMG for shortwave and longwave radiation (Iacono et al., 2008), Thompson for cloud microphysics (Thompson et al., 2008), and Grell-Freitas scheme for cumulus convection (Grell and Freitas, 2014). In CHIMERE, gas-phase reactions were calculated with the MELCHIOR2 model (Derognat et al., 2003), which includes 40 gaseous species and 120 photochemical reactions. Photolytic rates were parameterized with the FAST-JX model (Wild et al., 2000), as detailed in Mailler et al. (2016, 2017). Aerosol treatment is based on a sectional approach (Bessagnet et al., 2008; Mailler et al., 2017). Herein, we have used 10 dimensional bins ranging from 0.01 up to 40 µm. Aerosol model includes the main inorganic species (sulphate, nitrate, ammonium), water, black carbon, primary organic matter (OM), unspeciated particles, secondary organic aerosols (SOA), sea salt, and soil dust. We simulated anthropogenic and biogenic SOA with a single-step oxidation scheme, according to Bessagnet et al. (2008). Thermodynamic equilibrium of inorganic aerosols was simulated by using the ISORROPIA model (Nenen, 1998). Dry deposition of gases and aerosols were calculated with the schemes proposed by Wesely (1989) and Zhang et al. (2001), respectively. Wet deposition calculation followed the methods of Wang et al. (2014), as detailed in Mailler et al. (2017).

Aerosol optical properties in CHIMERE are calculated under the assumption of external mixing state, as outlined in Mailler et al. (2017), at 200, 400, 600, and 999 nm. Extinction efficiency, single scattering albedo (SSA), and asymmetry parameter are initially determined for each aerosol particles across each dimensional bin, and then are summed. These optical parameters are calculated assuming the aerosol particles as spherical using the Mie theory (Mie, 1908), solved through the spher.f code (Mischenko et al., 2002). Most of the aerosol complex refractive indices adopted in CHIMERE are based

on the ADIENT project (Mailler et al., 2016), with exception of BrC and BC. These latter are discussed in Section 2.2 and 2.3.

Anthropogenic emissions of trace gases and particles were taken from global inventory CAMS (Soulie et al., 2024) for the year 2022. Biomass burning emission fluxes were obtained from the CAMS dataset as described by Kaiser et al. (2012). Both inventories are at horizontal resolution of 0.1° x 0.1° and were re-gridded onto model grid according to Menut et al. (2021). Forest fire emissions from CAMS relative to June 2023 are displayed in Figure 2. Vertical injection profile of fire emissions adopted in CHIMERE is described in Menut et al. (2018). The injection height is calculated as in Sofiev et al. (2012) and corrected according to Veira et al. (2015), in case of huge fire. After the estimation of injection height, the shape of injection profile was calculated with the so called $2K_z$-like shape, where the emissions profile presents two maxima, one close to surface and one around injection height. Soil dust emissions were computed by using the scheme developed by Alfaro and Gomes (2001), with optimizations introduced by Menut et al. (2005). Sea salt emissions were estimated in accordance with Monahan (1986). NO_x emissions by lightning were included using the scheme of Price and Rind (1993), as detailed by Menut et al. (2020). Biogenic emissions were considered in our simulations employing the MEGAN model (Guenther et al., 2012).

Initial and boundary conditions for WRF were obtained from 6-hourly NCEP operational analyses at resolution a of 1° x 1°. Grid nudging toward NCEP analysis data of wind, temperature, and water vapor was applied in WRF on the model vertical levels above the planetary boundary layer. Sea ice extent and sea surface temperature were taken from NCEP data and were updated every six hours. CHIMERE was driven by the boundary conditions derived from the 2010-2017 gas and aerosol climatology based on the LMDZ-INCA global model (Folberth et al., 2006).

2.2 BC treatment

Within CHIMERE, the aerosol optical properties are calculated assuming an external mixing approach, which does not account for the BC absorption enhancement due to the lensing effect associated with the core-shell morphology of coated BC. Consequently, we have implemented within CHIMERE a scheme to account for this effect, drawing on the work of Liu et al. (2017). The authors demonstrated that E_{abs} depends on the mass ratio (M_r) of BC, given by ratio between the mass of non-BC aerosols and mass of soot particles. When $M_r<1$, BC is external mixed and absorption enhancement is not observed ($E_{abs}=1$), whereas for $M_r>3$, BC is internally mixed, and absorption is correctly calculated by core-shell model. When M_r is between 1 and 3, BC a transitional regime is observed, being neither external nor internal mixed. Therefore, for small M_r typical of fresh traffic sources (less than 1.5), E_{abs} is small (Schwarz et al., 2008). In fact, an E_{abs} of 1.1 has been reported in urban regions of California (Cappa et al., 2012) and China (Lan et al., 2013). When M_r is larger (greater than 3), as for example in biomass burning emissions, E_{abs} is in the range of 1.3-1.9 (Lack et al., 2012; Rathod et al., 2021; Kompalli et al., 2023).

Therefore, E_{abs} has been parameterized with a hybrid optical model, where no E_{abs} occurs when $M_r<1$ and is linearly interpolated to the upper threshold of $M_r=3$, where E_{abs} is accurately predicted by core-shell model (Liu et al., 2017):

$$E_{abs} = E_{abs_{cs}} F_{in} + (1 - F_{in})$$

$$F_{in} = 0.57 M_r - 074 \quad \text{for} \quad 1 < M_r < 3$$

where $E_{abs_{cs}}$ is the absorption enhancement calculated by core-shell model and F_{in} is the internally mixed fraction of BC. F_{in} is equal to 0 for M_r<1 and 1 for M_r>3. $E_{abs_{cs}}$ should be estimated with a core-shell algorithm; however, in this study, we used a constant value of 1.5. We have chosen this value because it is representative of the mean of E_{abs} estimations (Kong et al., 2024), which coincides with the average value recommended by Bond and Bergstrom (2006). It should be noted that the 90% confidence interval of E_{abs} distribution function reported by Kong et al. (2024) ranges from 1.15 (5%) to 2.18 (95%). This highlights that BC absorption simulation may depend on the value of $E_{abs_{cs}}$adopted. Finally, the refractive index assigned to BC was 1.95–0.79i, as recommended by Bond and Bergstrom (2006).

2.3 BrC treatment

The CHIMERE model treats OM as a scattering aerosol particle. Therefore, we have implemented a scheme to consider the BrC absorption within CHIMERE simulations. To our knowledge, currently there are not emission inventories of BrC. Previously, different methods have been employed to estimate the primary BrC emissions. For example, Jo et al. (2016) derived BrC emissions fluxes using a relationship between the modified combustion efficiency and absorbing Ångström exponent. Other studies, such as Feng et al. (2013) and Wang et al. (2014), have assumed that a fraction of emitted OA was BrC. Additionally, emissions have been also inferred from BC-to-OA ratio (Park et al., 2010; Saleh et al., 2015; Zhang et al., 2020). Alternatively, other researchers have treated all OA as radiation-absorbing particles, assigning to them specific optical properties (Wang et al., 2018). In our investigation, we have used this latter approach, as detailed below.

BB-BrC emissions were taken directly from BB-CAMS inventory (see Section 2.1). By contrast, BF-BrC anthropogenic emissions have been estimated from emission fluxes from domestic, industrial, waste management, and agricultural sectors. Specifically, a fraction of these emissions was considered as absorbing OA. This portion was derived based on the ratio of BF emissions to the total anthropogenic (FF+BF) OA emissions, as reported in the inventory of Bond et al. (2007), and then applied to OM emissions from CAMS, after being treated as described in Section 2.1.

In this investigation, we utilized the BrC optical properties as suggested by Wang et al. (2018), which were obtained constraining the MAC of biomass burning BrC with measurements from aircraft campaigns conducted in the continental United States. Additionally, the same authors demonstrated that their optical properties were applicable to reproduce the BB-BrC absorption observed over Europe. Consequently, we have adopted the MAC values from Wang et al. (2018), since our study is focusing on North America and Europe. Additionally, in our prior investigations, we were able to calculate BrC absorption at global scale in the atmosphere (Tuccella et al., 2020) and within snow (Tuccella et al., 2021),

using this set of optical properties. MACs at 365, 440, and 550 nm were 1.19, 0.76, and 0.39 m2/g for BF-BrC, and 1.33, 0.77, and 0.35 m2/g for freshly emitted BB-BrC, respectively.

Photochemical ageing of BB-OA is crucial in simulating BrC absorption, since it induces blanching of BrC through photochemistry processes. Several methodologies have been adopted to simulate the BB-BrC ageing. One of these consists in the passage from hydrophobic to hydrophilic, with hydrophilic component exhibiting a lower absorption compared to its hydrophobic counterpart (e.g., Tuccella et al., 2020; Zhang et al., 2020; Brugé et al., 2022). The transition is usually done with a characteristic time scale. Alternatively, some studies have adopted a blanching scheme wherein the absorption was tracked and attenuated based on OH concentration and a characteristic half-life time scale (Wang et al., 2018; Brown et al., 2018). However, the most recent advancement in BB-BrC ageing modelling has been introduced by DeLessio et al. (2024). This consists in considering the heterogeneous oxidation of BB-BrC by hydroxyl radical (OH), nitrate radical (NO3), and ozone (O3), according to the results of Hems et al. (2021). This innovative approach has been adopted and integrated in our investigation.

Specifically, following DeLessio et al. (2024), the ageing processes was divided in two distinct steps. In the first, freshly emitted BB-BrC undergoes an absorption enhancement, a phenomenon known as “browning”. In the second phase, the “browner” BrC is subjected to blanching process, during which the absorption is lower than that of freshly emitted BrC. Transfer mass from freshly emitted BrC to more absorbing BrC is succeeded by whitening, involving mass transfer from browner to less absorbing BrC. The mass transfer was quantified with second order rate constant for each reaction of BB-BrC with OH, NO3, and O3. During the nighttime, freshly emitted BB-BrC is oxidized by NO3 to form more absorbing OA, which then becomes less absorbing through subsequent oxidation with O3. During daylight hours, freshly BB-BrC is oxidized by OH to form more absorbing brown carbon. This browner BrC is then blanched through oxidation with OH and O3. Rate constants used were the same of DeLessio et al. (2024), derived from the initial first reaction rate for BrC processing defined by Hems et al. (2021), with oxidant concentrations assumed by same authors.

The MACs at 365, 440, and 550 nm of less absorbing BB-BrC were set at 0.37, 0.23, and 0.10 m2/g, respectively (Wang et al., 2018). These values reflect the average absorption of biomass burning BrC and are recommended for applications in models where absorption is not tracked. They should be used to account for absorption reduction when the whitening is not explicitly simulated (Wang et al., 2018). We note that the MACs adopted for less absorbing BB-BrC were slightly less 30% of those of freshly emitted OA. However, this value is very close to the minimum threshold of ¼, imposed by the same authors (Wang et al., 2018), below which the absorption may not drop, when it is tracked to account for BrC blanching. In addition, this value is also close to threshold of 20% based on laboratory studies (Fleming et al., 2020; Hems et al., 2021). As in DeLessio et al. (2024), we assigned to browner biomass burning BrC a MAC that is 150% larger of that attributed to freshly emitted OA.

In this work, we have also assumed that both biogenic and anthropogenic SOA are absorbing. We attributed to SOA-BrC the same set of optical properties of Wang et al. (2014), that for a typical size distribution of organic aerosols result in a MAC of 0.3 m^2/g at 440 nm.

The approach for implementing the BrC in CHIMERE illustrated above presents some limitations. These are related to ageing processes that were missed in our implementation. First, our model does not account for the blanching effect due to in-cloud water processing, which should reduce the browner BrC lifetime of about 3 hours (Hems et al., 2021). Second, we have not included in the model the blanching that SOA-BrC could undergo with ageing (Lee et al., 2014; Liu et al., 2016; Kasthuriarachchi et al., 2020). Another source of uncertain is the absorption attributed to the browner BB-BrC, which was assumed to be 150% higher than that of fresh emitted BrC. It should be noted that this value represents the middle range of the values observed in laboratory studies (Zhong and Jang, 2014; Hems et al., 2021). Therefore, this assumption could affect the BrC absorption close to BB sources, where browner BrC is present. Additionally, we have assigned to SOA-BrC compounds the same value for the imaginary part of the refractive index. In fact, the absorption of secondary BrC could be dependent on the specific SOA species. For example, the absorption of SOAs formed from photochemical oxidation of toluene appears to strongly depend on initial NO_x concentration (Lin et al., 2015, Liu et al., 2015, Moise et al., 2015, Dingle et al., 2019).

2.4 Numerical simulations

We performed a series of model simulation to evaluate the model development described above. The list of our runs is reported in Table 1. The first simulation has been conducted with the default version of CHIMERE, which does not include the BC absorption enhancement and BrC effects. This reference simulation (control, CTRL) was used to evaluate the aerosol transport and basic skill of the model in reproducing the AOD distribution.

The second simulation included only the scheme for BC_{Eabs} and was aimed to evaluate how this parameterization improves the aerosol absorption simulation in CHIMERE (BC_{Eabs}). The third run was takes into account both black carbon E_{abs} and BrC absorption. This simulation was labelled as "BEST" as it includes all the parameterizations introduced to enhance CHIMERE and because it represents a central estimate of absorption compared to the perturbed runs described below.

Other two simulations have been conducted to estimate the sensitivity of BC and BrC absorption to aerosol optical properties uncertainties. Consequently, we created a high absorption scenario (H-ABS) and a low absorption scenario (L-ABS), perturbing the BEST run. In the first case, we have not considered the BB-BrC ageing assigning it the MAC of freshly emitted BB-OA. Furthermore, $E_{abs_{cs}}$ was set to 1.9, representing the 90th percentile of E_{abs} distribution (Kong et al., 2024). By contrast, in the L-ABS scenario, we assigned to BB-BrC the MAC of blanched OA and $E_{abs_{cs}}$ was set to the 10th percentile of E_{abs} distribution reported in Kong et al. (2024), which is equal to 1.2. Consequently, by considering these two extreme cases of absorption, we have evaluated the range error in simulating the carbonaceous aerosols absorption, associated to uncertainties of BC absorption enhancement and BrC ageing parameterizations.

All simulations were conducted without the direct and indirect aerosol effects, since they may introduce feedback mechanisms that could influence atmospheric dynamics and subsequently affect the evaluation of model updates. Furthermore, the primary objective of this study is to assess the direct radiative effect of the 2023 Canadian wildfire episode and to investigate the implications of model

development on its estimation. The activation of direct and indirect effects could further alter the radiation budget through modifications in cloud coverage and properties. However, this is a subject that deserves future investigation.

2.5 Evaluation strategy

Numerical simulations have been compared with aerosol optical properties retrieved from ground-based and satellite instruments. Before the comparison, the CHIMERE output was regridded onto a regular grid with a horizontal resolution of 0.7° x 0.7°. The regular domain is presented in Figure 3.

Ground-based observations were taken from the version 3 of Aerosol Robotic Network (AERONET) Sun photometers (Holben et al., 2001; Sinyuk et al., 2020). AERONET is a global network providing observations of spectral columnar aerosol optical properties, such as AOD, AAOD, and single scattering albedo (SSA), at 440, 675, 870, and 1020 nm. AERONET disseminates data according to different quality check criteria: the cloud-screened L1.5, and cloud-screened and quality-assured L2.0 (Dubovik et al., 2002). In the latter, SSA is provided only when AOD levels at 440 nm exceeds 0.4. Consequently, only 18% of L2.0 data available in June 2023 was AAOD. Thus, following the methodology used in our previous studies (Curci et al., 2019; Tuccella et al., 2020), based on the work of Wang et al. (2016), we have complemented the L2 AAOD data with the L1.5.

Figure 3 displays the AERONET sites available during our study period, along with the fraction of AOD data coverage for each site. For our analysis, we included only the stations with at least 75% of data availability. Figure 3 also illustrates the average AOD at 440 nm measured at these sites during June 2023. Based on these AOD values, we identified three regions that were most interested by Canadian forest fires, which are outlined with blue rectangles in Figure 3. The first region (R1) included the AERONET stations located in Canada, representative of the measurement sites directly affected by the boreal fire sources. The second region (R2) covered the Western USA, where the observation stations were affected by smoke transported downwind the fire sources. Finally, the third region (R3) was represented by Western Europe, where AERONET sun photometers were subjected to transoceanic transport of Canadian boreal wildfire aerosols. In these three regions, we conducted a thorough and detailed analysis of the model performances. The AERONET stations used for AAOD evaluation are also displayed in Figure 3. In our analysis, we included only the stations with at least 55% of data availability, due to the reduced availability of AAOD data compared to AOD.

The simulated monthly spatial AOD pattern at 550 nm was compared with the Moderate Resolution Imaging Spectroradiometer (MODIS) AQUA data (Levy et al. 2015). In this work, we used the “AOD_550_Dark_Target_Deep_Blue_Combined” merged product from the “MYD04_L2” Level 2 (at 10 km spatial resolution at nadir), which combines the Deep Blue (Hsu et al., 2004) and Dark Target (Remer et al., 2005; 2020) MODIS algorithms, to disseminate the AOD global coverage. This merged product provides only high quality-assured (QA) pixels. The QA flag in the MODIS product is defined as an integer number, which in the selected combined AOD product is represented by:

- QA>3 over land and QA>0 over ocean for the Dark Target
- QA 2 and 3 for the Deep Blue

The MODIS satellite data were resampled at the spatial resolution to match the spatial resolution of the CHIMERE regular grid. For each grid cell, observed AOD was calculated as a weighted average, considering the quality-assurance flags from the MODIS retrievals. A minimum threshold of 30% of data with a QA score greater than 3 was required for each regridded pixel. The same approach was applied to average the satellite overpass times, extracting the nearest hour to align with the numerical simulation.

The simulated monthly spatial AOD and AAOD patterns at 354 nm were also compared with the Ozone Monitoring Instrument (OMI) Aura Near UV OMAERUV satellite product. Despite the coarse spatial resolution of 13x24 km^2 of the OMI satellite footprint, the OMAERUV algorithm provides aerosol spectral optical properties at 354 and 388 nm (Torres et al., 2007; 2013).

To compare the CHIMERE simulations with OMI data, only quality-assured data (i.e., quality flag = 0) were used, considering pixels with a solar zenith angle <70° and non-missing UV aerosol index values. The OMI satellite data were further resampled to match the spatial resolution of the CHIMERE regular grid. For each grid cell, the AOD/AAOD values were calculated as the average of all satellite pixels falling within the simulation grid.

Model accuracy in reproducing observations was evaluated using a set of statistical indices. These included the Pearson correlation coefficient, normalized mean bias (NMB), root mean square error (RMSE), Nash-Sutcliffe efficiency (NSE), Taylor score (TS), and standard deviation error (STDE). Definitions and explanations of these indices are reported in Section S1 of the Supplementary Material.

3 Model evaluation

3.1 Aerosol optical depth simulation

In this section, we assessed the model performance of the reference run (CTRL) in reproducing the AOD, since it is a key indicator of model skill in reproducing aerosol load, which in turn depends on different processes, such as emission, transport and deposition. Statistical indices obtained from the model comparison with observed AOD are reported in Table 2.

Figure 4 shows the comparison between monthly average of AOD at 550 nm predicted and observed from the MODIS satellite. CHIMERE satisfactorily reproduced the AOD patterns. In particular, the model captured the southeastern aerosol transport, downwind of the Canadian wildfires, toward East Coast of North America and the subsequent outflow on the Atlantic Ocean. The model successfully captured the eastward long-range transport across the ocean and the plume advection over Western Europe. However, the simulated AOD is generally underestimated compared to satellite observations. A more quantitative comparison indicates that CHIMERE reproduced the MODIS monthly data with a correlation of 0.77, an average NMB of –14%, NSE of 0.57, and TS of 0.79.

Figure 5 displays the comparison between monthly average AOD at 354 nm predicted by CHIMERE and observed by OMI. CHIMERE captured the AOD distribution retrieved by satellite, especially in Canada close to the boreal fire, Eastern North America, and Atlantic Ocean. The estimated correlation coefficient was 0.65, while the AOD was underpredicted by 30%. A closer inspection to Figure 5 reveals that this bias originates in Western USA, where the model underestimates the observations by a factor of 3-4. In general, the CHIMERE performance in reproducing OMI AOD appeared poorer compared to MODIS. The possible reason of this bias will be discussed later.

The comparison of the simulated daily AOD at 440 nm compared to the AERONET at all sites showed a NMB of -24%, while the correlation, NSE and TS were 0.55 and 0.88. Figure 6 depicts the comparison of modelled and observed daily averaged time series of AOD at 440 nm at the R1, R2, and R3 regions. Additionally, the figure also reports the scatter plots between predicted and observed daily AOD values. The model captured the mean daily observed AOD behaviour in R1, R2, and R3. The CHIMERE model was able to reproduce the AOD main peaks at the Canadian AERONET sites (R1) in the first half of June, although it did not accurately capture the peaks on June 23 and 25-26. At the same time, the peaks of early, mid, and end June on eastern USA downwind from Canadian sources (R2) were captured, as well as the late June peak on western Europe (R3) due to the long-range smoke transport from North America.

Furthermore, the correlation coefficient and TS exceeded 0.70 and 0.80 for all three regions, respectively. The NMB was about -20% in R2 and R3, while in R1, it was -35%. The largest bias in R1 could be mainly attributed to the model resolution used in this study that could affect the right position of the wildfire sources. The largest bias in R1 could be mainly attributed to the model resolution deployed in this study that could impact the right position of the wildfire sources. However, it should be noted that even at higher resolution, small errors in simulated wind speed and direction may significantly impact the plume position prediction downwind of the sources (Tuccella et al., 2017). Additionally, the assessment

of model performance in R1 may be affected by the limited number (see Figure 3) of AERONET stations available in this region.

The same analysis has been conducted for the comparison of modelled AOD at 675 nm with AERONET measurements. Figure S1 shows the daily averaged times series and daily scatter plots of predicted versus observed AOD at this wavelength. The statistical indices obtained from this comparison are presented in Table S1. At this wavelength, CHIMERE simulated the average time series of AOD in a similar way as well as discussed at 440 nm. The correlation coefficient with observed daily values was 0.78, 0.73 and 0.70 in R1, R2, and R3, respectively.

In summary, the outcomes of the statistical analysis obtained from the comparison of the simulated AOD with the AERONET and satellite data are comparable to that of current regional atmospheric models (Curci et al., 2015; Palacios-Peña et al., 2019). Overall, our model exhibited an underestimation of AOD, which was quantifiable in average between 15-30%. This bias has been found in other studies conducted with CHIMERE, even with finer resolutions with respect to the one used in this study (e.g., Menut et al., 2023). Several factors may contribute to a potential bias in the simulated AOD, among those the assumption on particle mixing state (Curci et al., 2015), the simulated aerosol size distribution (Esteve et al., 2014) and the aerosol chemical composition as well as the adopted schemes to represent the organic aerosol fraction (Balzarini et al., 2015). Regarding the dependency on the chemical composition, Konovalov et al. (2023) showed that the parameterization for the secondary organic aerosols used in this study tends to underestimate the SOA mass during wildfire episodes, with consequent bias on the aerosol load. This aspect could be improved by using more realistic SOA schemes available in CHIMERE (such as the Volatility Set Basis scheme), but these are computational expensive for the aim of this investigation, since they would have required many additional variables resulting from the splitting of primary OA sources for BrC simulation. Another important source of bias in this study is the uncertainty of BB emission inventories. Aerosol simulations and their climatic impact are sensitive to specific BB emission inventory (Liu et al., 2018; Ramnarine et al., 2019; Carter et al., 2020). This uncertainty may be larger at high latitudes, where the fire sources in this study are located, due to the increased cloud cover in these regions, which may decrease the accuracy of BB emission estimates (Hua et al., 2024).

Additionally, in this discussion, it is essential to consider the uncertainties in the AOD measurements, especially the error associated with satellite data. AERONET has an uncertainty of 0.01-0.02 (Holben et al., 2001), while the error of MODIS is $0.05 \pm 0.20 \cdot \mathrm{AOD}$ and $0.03 \pm 0.05 \cdot \mathrm{AOD}$ over land and ocean, respectively (Tanré et al., 1997; Kaufman et al., 1997). The average error expected in OMI AOD is of the order of 30% (Torres et al., 2002). We compared AOD retrieved by MODIS and OMI with AERONET data. The comparison of MODIS AOD is shown in Figure S2. The analysis indicates that MODIS tends to overestimate AOD at AERONET stations, with a monthly average bias of 18%. Figure S3 shows the comparison of OMI AOD with AERONET data, revealing that OMI overestimates AOD by 40%. This bias is particularly evident in the western United States, where we identified the most substantial discrepancies between CHIMERE and OMI data.

3.2 Aerosol absorption simulation

In this section, we evaluated the performance of the new absorption scheme implemented within the CHIMERE model and detailed in Sections 2.2 and 2.3. Indeed, we compared the simulated AAOD for the reference simulation (CTRL), the BC_{Eabs}, and the BEST simulations with the OMI and AERONET AAOD data.

Figure 7 shows the monthly average of AAOD at 354 nm for June 2023, as observed by OMI and predicted by the CHIMERE in the CTRL run, BC_{Eabs}, and BEST simulations. The statistical indices derived from this comparison are reported in Table 3. The correlation coefficient for all the three simulations ranged between 0.50 and 0.54. However, the default model (CTRL), which assumes an external mixing state, failed to reproduce the AAOD observed pattern, exhibiting a bias of -78%. The increase in absorption due to BC_{Eabs} was moderate and primarily localized near the biomass burning sources, where the mass ratio (M_r) reaches its highest values. The overall bias of BC_{Eabs} is reduced by 3% compared to CTRL. A significant improvement in aerosol absorption was observed in BEST simulations. The inclusion of the BrC treatment enabled the model to reproduce the spatial pattern of AAOD much more closely to that observed by OMI. This improvement was also reflected in the statistical indices with the Taylor score increasing more than twofold from CTRL (0.34) to BEST (0.73). Despite this progress, the mean bias still was -55%. The largest biases in BEST simulations were found in Western USA and North Africa. The latter could be related to the errors in simulating the aerosol dust absorption; however, uncertainties in OMI retrievals must also be considered. We will explore this issue in more detail at the end of this section.

Figure 8 shows the comparison of daily AAOD averaged time series at 440 and 675 nm simulated in the CTRL, BC_{Eabs}, and BEST against observations from AERONET sites in the R1, R2, and R3 regions. Generally, the AAOD simulated in CTRL was underestimated, particularly during peak events related to the Canadian forest fires across all three regions. Including the BC absorption enhancement (BC_{Eabs}), a moderate improvement in AAOD simulation was observed at 440 nm Conversely, at 675 nm, the inclusion of BC E_{abs} resulted in a more accurate prediction of AAOD peaks both near the fire sources (R1) and downwind (R2), as well as in late June over western Europe (R3), attributed to transoceanic smoke transport from North America. This improvement is attributable to the dominance of BC at this wavelength, since BrC primarily absorbs solar radiation in the UV range. Consequently, at 675 nm the BC_{Eabs} and BEST simulations were identical, and the results obtained at this wavelength may be considered an evaluation of BC E_{abs} parameterization.

Figure 9 displays the scatter plots of the daily AAOD at 440 nm simulated in CTRL, BC_{Eabs}, and BEST models with the AAOD measurements from the AERONET sites in R1, R2, and R3. The summary of the statistical indices is reported in Figure 10. In general, the correlation coefficient remained constant across the simulations (about 0.70, 0.64, and 0.53 in R1, R2, and R3, respectively). This indicates that all three the models were able to capture the temporal variations of absorption. It should be noted that correlation, as well as NSE and TS, decreased moving away from the fire sources, most likely because in R1 the AAOD simulation was most affected by BB emissions, while far from boreal wildfires the mixing with other sources may alter the relative contribution of the absorbing and scattering aerosols, lowering the performance indices. At the same time, RMSE and STDE decreased moving downwind of the fires.

The bias represented the most varying metric. The CTRL simulation underpredicted the AAOD by 18% in R1, while it became negligible after including BC enhancement in the model. The addition of the BrC absorption (BEST), lead to a positive bias of +30%. This result could be attributed to the presence of "browner" BB-BrC, whose absorption could be overestimated, given the high uncertain of its MAC. Moreover, as highlighted also in Section 3.1 for the AOD, model evaluation in R1 may be affected by the limited number of AERONET observations available in this area. Similar results in terms of bias are obtained for the R2 and R3. The CTRL simulation underestimated the absorption by about 40%, while in BC_{Eabs} the bias was reduced to about -25%, becoming slightly positive in BEST.

The same analysis has been performed for AAOD at 675 nm. The results of the comparison are reported in Figures S4 and S5. As for AAOD at 440 nm, the correlation coefficient was constant across model simulations and decreased moving away from boreal wildfires. Its values were about 0.75, 0.65, and 0.45 in R1, R2, and R3 respectively. The same behavior was exhibited by NSE and TS. Conversely RMSE and STDE improved downwind the BB sources. Also in this case, the metric that showed the most variations among simulations was the bias. In R1, NMB was negligible in CTRL, but it increased at +25% in BC_{Eabs}. CTRL underestimated the AAOD at 675 nm by 18% and 26% in R2 and R3, respectively. Adding the BC absorption enhancement, the bias became negligible in R2 and reduced to -9% in R3.

In summary, the evaluation demonstrated that the new absorption scheme implemented in CHIMERE overall enhances the model skill in reproducing the observed AAOD patterns. The uncertainties of absorption treatment used in this work are mostly related to the missing of some blanching effects due to in-cloud processes of primary BrC and SOA ageing. Additionally, assumptions regarding the MAC of browner BB-BrC could introduce further uncertainty. Furthermore, the uncertainties could also arise from the simplified parameterization of E_{abs}. In our model, the absorption enhancement predicted by core-shell model ($E_{abs_{cs}}$) is maintained at the fixed value of 1.5, which may not accurately capture the variability observed under different atmospheric conditions.

Moreover, uncertainties associated with AERONET and OMI data could affect the model comparison with observations. In our analysis, we complemented the L2.0 of AERONET for AAOD with L1.5 measurements, as AAOD in the L2 dataset was provided only for AOD at 440 nm larger than 0.4. The uncertainty of single scattering albedo (SSA), used to derive AAOD, is site dependent. Generally, the uncertainty related to SSA retrieval varies with AOD, ranging from approximately ±0.03 for AOD at 440 nm greater than 0.5 to ±0.05–0.07 for AOD less than 0.2 (Sinyuk et al., 2020). Furthermore, this uncertainty increases with larger wavelengths. Concerning the uncertainty of OMI retrieval, the comparison of OMI AAOD with AERONET data is displayed in Figure S6. OMI shows an average positive bias of 66% with respect to AERONET. The most considerable discrepancies between AERONET and OMI data are found in the western United States, where we noted the most important error in CHIMERE AAOD prediction with respect to OMI data.

4 Direct radiative effect

In this section, we have assessed the impact of new treatment of BC and OA absorption on the AAOD simulation and its implication for the DRE. This analysis was conducted over the regular CHIMERE domain.

Figure 11 shows the total and BB aerosols average AAOD at 550 nm for June 2023, as calculated in CTRL and BEST simulations. The domain averages of AAOD are reported in Table 4. The total average AAOD was 0.0068 in CTRL simulation, while in the enhanced model (BEST) it increased to 0.0089 (+31%). In the Canadian wildfire source regions, AAOD in the BEST simulation increased by 35-40% relative to the CTRL run, with some areas showing a rise of up to 45% (Figure S7). The relative increase in AAOD could reach up to 50% in regions where BB aerosols are mixed with BF sources, such as in the southeastern USA. Over the Atlantic Ocean and the Arctic, the relative increase was 30-35%. A 35-40% increase was also observed over Eastern Europe, largely due to BF emissions of OA. AAOD due to BB was 0.0047 in the CTRL run and increased to 0.0066 (+40%) in BEST simulation. According to our model, BB contributes approximately 74% to the total aerosol absorption within the considered domain. The maximum uncertainty in domain-average AAOD from the enhanced model was evaluated by comparing the BEST run with extreme absorption scenarios (L-ABS and H-ABS tests), resulting in an uncertainty range of -10/+24% for total AAOD and -14/+30% for BB AAOD.

DRE at the top of the atmosphere (TOA) has been calculated offline with a simplified formalization provided by Seinfeld and Pandis (2016). The details of this formulation are reported in Section S2 of the Supplementary Material.

Figure 12 displays the average BB all-sky DRE for June 2023, as calculated in CTRL and BEST simulations. Table 5 reports the domain averages of clear and all-sky top of the atmosphere (TOA) DRE. The uncertainty associated with the DRE from the enhanced model was evaluated using the same approach as for AAOD.

In the default model, the all-sky DRE related to the intense Canadian wildfire event was -2.1 W/m², with the strongest cooling effects observed over oceans and land, reaching -30/-20 W/m² near the BB sources in Canada. By contrast, warming effects were observed over snow-covered land and sea ice, with a warming of up to 10-15 W/m² in Arctic regions downwind of the BB sources.

In the BEST model, the all-sky DRE was reduced to -1.9 W/m² (-2.0/-1.8 W/m², ±5%), indicating an additional monthly average warming of +0.2 W/m² (+10%) in the enhanced model simulation of the Canadian wildfire climatic impact. This supplemental warming was most pronounced over snow/ice-covered regions, with a DRE reduction up to 2.5-3.0 W/m² in North America downwind of the fires and up to 2.0-2.5 W/m² in southern Greenland. The cooling effect in BEST was also reduced by up to 1.5 W/m² in Canada near the source regions and by few tens of W/m² over the Atlantic Ocean and Europe.

Finally, it is insightful to examine the variation in DRE between the default and enhanced models, normalized to the change in AAOD at 550 nm between the two simulations. The resulting normalized BB all-sky ΔDRE was 105 W/m^2/AAOD. This value suggests a significant DRE sensitivity to AAOD change in the model.

These results emphasize that accurate prediction of BC and BrC sunlight absorption is crucial for understanding the impact of intense boreal wildfires on regional climate. Our findings suggest that models lacking proper treatment of carbonaceous aerosol absorption may overestimate the cooling effect of boreal wildfires. Therefore, improving aerosol absorption parameterizations is crucial, along with incorporating the feedback between climate and aerosol smoke from boreal fires, both in near-future climate predictions and the development of effective mitigation strategies. Recent study of Allen et al. (2024) suggest that anthropogenic aerosol mitigation strategies will likely increase boreal forest fires, but the full impact of resulting emissions on the climate system remains uncertain. Without adequate treatment of BC and BrC absorption, the climatic effect of these emissions could be significantly misrepresented.

5 Conclusions

Black carbon (BC) and brown carbon (BrC) are light-absorbing aerosols which play a key role in the climatic system. Boreal wildfires are significant sources of these particles. Boreal wildfire events are increasing due to climate change. Accurate modelling of BC and BrC absorption is essential for predicting the direct radiative effect (DRE) of these events. In this study, we modelled the BC and BrC absorption during the severe Canadian wildfires of June 2023 using an enhanced CHIMERE model and assessed the impact of these improvements on the DRE of the wildfires.

The CHIMERE model was configured on a large domain spanning from North America to Eastern Europe, including the high latitude up to 75°N. We implemented in the model a parameterization for BC absorption enhancement (E_{abs}), which depends on the mixing state of BC particles, through the mass ratio of non-BC to BC aerosols, according to the work of Liu et al. (2017). We also implemented an advanced scheme for BrC absorption, which accounts for "browning" and "blanching" processes due to photochemical ageing, following the approach of DeLessio et al. (2024). A series of simulations were conducted to assess the impact of BC E_{abs} and BrC on aerosol absorption prediction. Model performance was evaluated through a statistical comparison with aerosol optical depth (AOD) and absorbing aerosol optical depth (AAOD) data from satellite instruments (MODIS and OMI) and ground-based AERONET stations, focusing on regions impacted by Canadian wildfires.

The model captured the spatial patterns of AOD, particularly the long-range transport of aerosols from Canadian wildfires toward the East Coast of North America and across the Atlantic to Europe. The model generally underestimated AOD compared to satellite observations, with biases ranging from 15-30%. Correlation coefficients for the comparison with MODIS and OMI AOD were 0.77 and 0.65, respectively, while comparisons with AERONET showed a correlation of 0.79 and a bias of -24%.

The default model (CTRL) underestimated AAOD retrieved by OMI, particularly near biomass burning sources, with a bias of up to -78%. A moderate improvement was observed by including in model the BC absorption enhancement (BC_{Eabs}), but the most substantial advancements were achieved in the BEST simulations, which included both E_{abs} and BrC treatment, improving spatial patterns and statistical indices. The model comparison with AAOD measurements at 440 and 675 nm from AERONET exhibited a correlation of about 0.75 near the wildfire sources, which tends to decrease moving downwind from these sources. In general, the CTRL run underestimated the observed AAOD, while a significant improvement of the model was obtained in the BEST simulation.

The enhanced model (BEST) increased the monthly domain average AAOD at 550 nm by 31% compared to the CTRL, with the most significant changes observed near the Canadian wildfires and areas where biomass burning aerosols mixed with fossil fuel sources. Canadian smoke aerosols contributed approximately to 74% of total aerosol absorption.

The all-sky TOA DRE associated with the Canadian wildfires of June 2023 was estimated to be -2.1 W/m² in the CTRL run. In the best simulation, this value was reduced to -1.9 W/m², indicating an additional warming of +0.2 W/m² (+10%), attributable to the enhanced treatment of BC and BrC absorption. The increased in DRE calculated in BEST was more pronounced in the regions covered by snow and ice, such as the Arctic and Southern Greenland. Furthermore, the normalized all-sky DRE

change resulting from the increase in AAOD obtained in BEST simulation was +105 W/m²/AAOD, highlighting the critical role of aerosol absorption in radiative balance during the intense boreal wildfire events.

The main uncertainties in this study are linked to the absorption scheme implemented in CHIMERE, which does not account for the blanching due to in cloud-processes of primary BrC and SOA ageing. Moreover, the complex part of refractive index adopted for browner BrC could introduce an additional uncertainty factor. Another source of uncertainty is related to the assumption of a constant E_{abs} resulting from the core-shell morphology of BC. To evaluate the impact of these uncertainties, we perturbed the BEST simulation with low and high absorption scenarios. The results indicate an error of ±5% in the DRE estimate attributed to Canadian wildfires.

Overall, the findings of this investigation demonstrate the importance of an accurate simulation of BC and BrC absorption to properly assess the regional climatic impact of intense boreal wildfire. The lack of this factor in the models may results in an overestimation of the radiative cooling effect of boreal fires. Consequently, improving the parameterizations of carbonaceous aerosol absorption is essential for reliable near-future climatic predictions and effectively evaluation of the efficiency of the aerosol mitigation strategies.

Code/Data availability: CHIMERE simulations and model code are available at this link https://osf.io/dnygq/. This is a temporary link for peer review only and will be made public at acceptance. AERONET data are freely available at the following website https://aeronet.gsfc.nasa.gov/new_web/data.html. MODIS and OMI data may be downloaded at https://disc.gsfc.nasa.gov/.

Author Contributions: PT and LDA conceptualized the study and developed the methodology. PT and LM developed the model. PT performed the model simulations with contribution from LDA. PT, LDA and ADM performed the formal analysis. PT, LDA and VC prepared and wrote the original draft. PT, LDA, ADM, VC, LM, ER, and GP reviewed the original draft.

Competing interests: The authors declare that they have no conflict of interest.

Funding: This work was not supported by any external funding.

References

Adachi, K., Chung, S. H., and Buseck. P. R. (2010). Shapes of soot aerosol particles and implications for their effects on climate. *J. Geophys. Res.*, 115, D15206, https//doi.org/10.1029/2009JD012868.

Akagi, S. K., Craven, J. S., Taylor, J. W., McMeeking, G. R., Yokelson, R. J., Burling, I. R., Urbanski, S. P., Wold, C. E., Seinfeld, J. H., Coe, H., Alvarado, M. J., and Weise, D. R. (2012). Evolution of trace gases and particles emitted by a chaparral fire in California. *Atmos. Chem. Phys.*, 12, 1397–1421, https//doi.org/10.5194/acp-12-1397-2012.

Alfaro, S. C., and Gomes, L. (2001). Modeling mineral aerosol production by wind erosion: Emission intensities and aerosol size distribution in source areas. *J. Geophys. Res*., 106, 18075–18084, https//doi.org/10.1029/2000JD900339.

Alexander, D. T. L., Crozier, P. A., and Anderson, J. R. (2008). Brown carbon spheres in East Asian outflow and their optical properties. *J. Geophys. Res.*, 321, 833–836, https//doi.org/10.1126/science.1155296.

Allen, R. J., et al. (2024). Are Northern Hemisphere boreal forest fires more sensitive to future aerosol mitigation than to greenhouse gas–driven warming?. *Sci. Adv*., 10, DOI:10.1126/sciadv.adl4007.

Andreae, M. O., and Gelencsér, A. (2006). Black carbon or brown carbon? The nature of light-absorbing carbonaceous aerosols. *Atmos. Chem. Phys.*, 6, 3131–3148, https//doi.org/10.5194/acp-6-3131-2006.

Arola, A., Stu G., Kazadzis, S., Dey, S., and Tripathi, S. N. (2011). Inferring absorbing organic carbon content from AERONET data. *Atmos. Chem. Phys.*, 11, 215–225, https//doi.org/10.5194/acp-11-215-2011.

Balzarini, A., Pirovano, G., Honzak, L., Žabkar, R., Curci, G., Forkel, R., Hirtl, M., San José, R., Tuccella, P., and Grell, G.A. (2015). WRF-Chem model sensitivity to chemical mechanisms choice in reconstructing aerosol optical properties. *Atmos. Environ.*, 115, 604-619, https//doi.org/10.1016/j.atmosenv.2014.12.033.

Bessagnet, B., Hodzic, A., Vautard, R., Beekmann, M., Cheinet, S., Honoré, C., Liousse, C., and Rouil, L. (2004). Aerosol modeling with CHIMERE—Preliminary evaluation at the continental scale. *Atmos. Environ.*, 38, 2803–2817, https//doi.org/10.1016/j.atmosenv.2004.02.034.

Bessagnet, B., Menut, L., Curci, G., Hodzic, A., Guillaume, C., Liousse, C., Moukhtar, S., Pun, B., Seigneur, C., and Schulz, M. (2008). Regional modeling of carbonaceous aerosols over Europe-Focus on secondary organic aerosols. *J. Atmos. Chem.*, 61, 175–202, https//doi.org/10.1007/s10874-009-9129-2.

Bond, T. C., and Bergstrom R. W. (2006). Light absorption by carbonaceous particles: an investigative review. *Aerosol. Sci. Tech.*, 40, 27–67, https//doi.org/10.1080/02786820500421521.

Bond, T. C., Bhardwaj, E., Dong, R., Jogani, R., Jung, S. K., Roden, C., Streets, D. G., and Trautmann, D. G. (2007). Historical emissions of black and organic carbon aerosol from energy-related combustion, *Global Biogeochem.*, 21, 1850–2000, https//doi.org/10.1029/2006GB002840.

Bond, T. C., Doherty, S. J., Fahey, D. W., Forster, P. M., Berntsen, T., De Angelo B. J., Flanner, M.G., Ghan, S., Kärcher, B., Koch, D., Kinne, S., Kondo, Y., Quinn, P. K., Sarofim, M. C., Schultz, M. C., Schulz, M., Venkataraman, C., Zhang, H., Zhang, S., Bellouin, N., Guttikunda, S. K., Hopke, P. K., Jacobson, M. Z., Kaiser, J. W., Klimont, Z., Lohmann, U., Schwarz, J. P., Shindell, D., Storelvmo, D., Warren, S. G., and Zender, C. S. (2013). Bounding the role of black carbon in the climate system: A scientific assessment. *J. Geophys. Res.-Atmos.*, 118, 5380–5552, https//doi.org/10.1002/jgrd.50171.

Bondy, A., Bonanno, D., Moffet, R., Wang, B., Laskin, A., and Ault, A. (2018). The diverse chemical mixing state of aerosol 430 particles in the southeastern United States. *Atmospheric Chemistry and Physics*, 18, 12595-12612, 10.5194/acp-18- 12595-2018.

Bones, D. L., Henricksen, D. K., Mang, S. A., Gonsior, M., Bateman, A. P., Nguyen, T. B., Cooper, W. J., and Nizkorodov, S. A. (2010). Appearance of strong absorbers and fluorophores in limonene-O3 secondary organic aerosol due to NH4+ mediated chemical aging over long time scales. *J. Geophys. Res.*, 115, https//doi.org/10.1029/2009JD012864.

Briant, R., Tuccella, P., Deroubaix, A., Khvorostyanov, D., Menut, L., Mailler, S., and Turquety, S. (2017). Aerosol–radiation interaction modelling using online coupling between the WRF 3.7.1 meteorological model and the CHIMERE 2016 chemistry-transport model, through the OASIS3-MCT coupler. *Geosci. Model Dev*., 10, 927–944, https//doi.org/10.5194/gmd-10-927-2017.

Brown, H., Liu, X., Feng, Y., Jiang, Y., Wu, M., Lu, Z., Wu, C., Murphy, S., and Pokhrel, R. (2018). Radiative effect and climate impacts of brown carbon with the Community Atmosphere Model (CAM5), *Atmos. Chem. Phys.*, 18, 17745–17768, https//doi.org/10.5194/acp-18-17745-2018.

Brown, H., Wang, H., Flanner, M., Liu, X., Singh, B., Zhang, R., Yang, Y., and Wu M. (2022). Brown carbon fuel and emission source attributions to global snow darkening effect. J. Adv. *Model Earth Sy.*, 14, e2021MS002768, https//doi.org/10.1029/2021MS002768.

Byrne, B., Liu, J., Bowman, K.W. et al. (2024). Carbon emissions from the 2023 Canadian wildfires. *Nature*, https://doi.org/10.1038/s41586-024-07878-z.

Cappa, C. D., Onasch, T. B., Massoli, P., Worsnop D. R., Bates, T. S., Cross, E. S., Davidovits, P., Hakala, J., and Hayden, K. L. (2012). Radiative Absorption Enhancements Due to the Mixing State of Atmospheric Black Carbon, *Science*, 337, 1078–1081, https//doi.org/10.1126/science.1223447.

Carter, T. S., Heald, C. L., Jimenez, J. L., Campuzano-Jost, P., Kondo, Y., Moteki, N., Schwarz, J. P., Wiedinmyer, C., Darmenov, A. S., and da Silva, A. M. (2020). How emissions uncertainty influences the distribution and radiative impacts of smoke from fires in North America. *Atmos. Chem. Phys.*, 20, 2073-2097, https//doi.org/10.5194/acp-20-2073-2020.

Chen, F., and Dudhia, J. (2001). Coupling an Advanced Land Surface-Hydrology Model with the Penn State-NCAR MM5, Modeling System. Part I: Model Implementation and Sensitivity. *Mon. Weather Rev*., 129, 569–585, https//doi.org/10.1175/1520-0493(2001)129<0569:CAALSH>2.0.CO;2.

Chen, Y., and Bond, T. C. (2010). Light absorption by organic carbon from wood combustion. *Atmos. Chem. Phys.*, 10, 1773–1787, https//doi.org/10.5194/acp-10-1773-2010.

Cheng, Z., Atwi, K. M., Yu, Z., Avery, A., Fortner, E. C., Williams, L., Majluf, F., Krechmer, J. E., Lambe, A. T., and Saleh, R. (2020). Evolution of the light-absorption properties of combustion brown carbon aerosols following reaction with nitrate radicals, *Aerosol Sci. Tech.*, 54, 849–863, https://doi.org/10.1080/02786826.2020.1726867.

Clarke, A. D., Shinozuka, Y., Kapustin, V. N., Howell, S., Huebert, B., Doherty, S., Anderson, T., Covert, D., Anderson, J., Hua, X., Moore II, K. G., McNaughton, R., Carmichael, G., and Weber, R. (2004). Size distributions and mixtures of dust and black carbon aerosol in Asian outflow: physiochemistry and optical properties. *J. Geophys. Res*., 109, D15S09, https//doi.org/10.1029/2003JD004378.

Craig, A., Valcke, S., and Coquart, L. (2017). Development and performance of a new version of the OASIS coupler, OASIS3-MCT_3.0, *Geosci. Model Dev.*, 10, 3297–3308, https//doi.org/10.5194/gmd-10-3297-2017.

Curci, G., Hogrefe, C., Bianconi, R., Im, U., Balzarini, A., Baro, R., Brunner, D., Forkel, R., Giordano, L., Hirtl, M., Honzak, L., Jimenez-Guerrero, P., Knote, C., Langer, M., Makar, P. A., Pirovano, G., Perez, J. L., San Jose, R., Syrakov, D., Tuccella, P., Werhahn, J., Wolke, R., Zabkar, R., Zhang, J., and Galmarini, S. (2015). Uncertainties of simulated aerosol optical properties induced by assumptions on aerosol physical and chemical properties: an AQMEII-2 perspective. *Atmos. Environ.*, 115, 541–552, https//doi.org/10.1016/j.atmosenv.2014.09.009.

Curci, G., Alyuz, U., Barò, R., Bianconi, R., Bieser, J., Christensen, J. H., Colette, A., Farrow, A., Francis, X., Jiménez-Guerrero, P., Im, U., Liu, P., Manders, A., Palacios-Peña, L., Prank, M., Pozzoli, L., Sokhi, R., Solazzo, E., Tuccella, P., Unal, A., Vivanco, M. G., Hogrefe, C., and Galmarini, S. (2019). Modelling black carbon absorption of solar radiation: combining external and internal mixing assumptions, *Atmos. Chem. Phys.*, 19, 181–204, https//doi.org/10.5194/acp-19-181-2019.

DeLessio, M. A., Tsigaridis, K., Bauer, S. E., Chowdhary, J., and Schuster, G. L. (2024). Modeling atmospheric brown carbon in the GISS ModelE Earth system model, *Atmos. Chem. Phys*., 24, 6275–6304, https//doi.org/10.5194/acp-24-6275-2024.

Derognat, C., Beekmann, M., Baeumle, M., Martin, D., and Schmidt, H. (2003). Effect of biogenic volatile organic compound emissions on tropospheric chemistry during the Atmospheric Pollution Over the Paris Area (ESQUIF) campaign in the Ile-de-France region. *J. Geophys. Res.*, 108, https//doi.org/10.1029/2001JD001421.

Dingle, J. H., Zimmerman, S., Frie, A. L., Min, J., Jung, H., and Bahreini, R. (2019). Complex refractive index, single scattering albedo, and mass absorption coefficient of secondary organic aerosols generated from oxidation of biogenic and anthropogenic precursors. *Aerosol Sci. Technol.*, 53, 449–463, https://doi.org/10.1080/02786826.2019.1571680,.

Drugé, T., Nabat, P., Mallet, M., Michou, M., Rémy, S., and Dubovik, O. (2022). Modeling radiative and climatic effects of brown carbon aerosols with the ARPEGE-Climat global climate model. *Atmos. Chem. Phys.*, 22, 12167–12205, https//doi.org/10.5194/acp-22-12167-2022.

Dubovik, O., Holben, B., Eck, T. F., Smirnov, A., Kaufman, Y. J., and King, M. D. (2002). Variability of absorption and optical properties of key aerosol types observed in worldwide locations, *J. Atmos. Sci.*, 59, 590–608, doi:10.1175/1520-0469(2002)059<0590:VOAAOP>2.0.CO;2.

Esteve, A.R., Highwood, E. J., Morgan, W. T., Allen, G., Coe, H., Grainger, R. G., Brown, P., and Szpek, K. (2014). A study on the sensitivities of simulated aerosol optical properties to composition and size distribution using airborne measurements, *Atmos. Envir*on., 89, 517-524, https//doi.org/10.1016/j.atmosenv.2014.02.063.

Eckdahl, J. A., Kristensen, J. A., and Metcalfe, D. B. (2022). Climatic variation drives loss and restructuring of carbon and nitrogen in boreal forest wildfire. *Biogeoscie*nces, 19, 2487–2506, https://doi.org/10.5194/bg-19-2487-2022,.

Feng, Y., Ramanathan, V., Kotamarthi, V. R. (2013). Brown carbon: A significant atmospheric absorber of solar radiation? *Atmos. Chem. Phys.*, 13, 8607–8621, https//doi.org/10.5194/acp-13-8607-2013.

Fierce, L., Onasch, T. B., Cappa, D. C., Claudio, M., Swarup, C., Janarjan, B., Davidovits, P., Fischer, D. Al., Helgestad, T., Lambe, A. T., Sedlacek, A. J., Smith, G. D., and Wolff, L. (2020). Radiative absorption enhancements by black carbon controlled by particle-to-particle heterogeneity in composition. *P. Natl. Acad. Sci. USA*, 117(10), 5196-5203, https//doi.org/10.1073/pnas.1919723117.

Filonchyk, M. and Peterson, M. P. (2024). Changes in aerosol properties at the El Arenosillo site in Southern Europe as a result of the 2023 Canadian forest. *Environmental Research*, 260, https://doi.org/10.1016/j.envres.2024.119629.

Fleming, L. T., Lin, P., Roberts, J. M., Selimovic, V., Yokelson, R., Laskin, J., Laskin, A., and Nizkorodov, S. A. (2020). Molecular composition and photochemical lifetimes of brown carbon chromophores in biomass burning organic aerosol. *Atmos. Chem. Phys*., 20, 1105–1129, https//doi.org/10.5194/acp-20-1105-2020.

Flanner, M. G., Zender, C. S., Randerson, J. T., and Rasch, P. J. (2007). Present-day climate forcing and response from black carbon in snow. *J. Geophys. Res*., 112, D11202, https//doi.org/10.1029/2006JD008003.

Flanner, M. G., Zender, C. S., Hess, P. G., Mahowald, N. M., Painter, T. H., Ramanathan, V., and Rasch, P. J. (2009). Springtime warming and reduced snow cover from carbonaceous particles. *Atmos. Chem. Phys.*, 9, 2481–2497, https//doi.org/10.5194/acp-9-2481-2009.

Folberth, G. A., Hauglustaine, D. A., Lathière, J., and Brocheton, F. (2006). Interactive chemistry in the Laboratoire de Météorologie Dynamique general circulation model: model description and impact analysis of biogenic hydrocarbons on tropospheric chemistry, *Atmos. Chem. Phys.*, 6, 2273–2319, https//doi.org/10.5194/acp-6-2273-2006.

Forrister, H., Liu, J., Scheuer, E., Dibb, J., Ziemba, L., Thornhill, K. L., Anderson, B., Diskin, G., Perring, A. E., Schwarz J. P., Campuzano-Jost, P., Day, D. A., Palm, B. B., Jimenez J. L., Nenes, A., and Weber, J. (2015). Evolution of brown carbon in wildfire plumes. *Geophys. Res. Lett.*, 42, https//doi.org/10.1002/2015GL063897.

Gillett, N.P. (2004). Detecting the effect of climate change on Canadian forest fires. *Geophysical Research Letters*, 31 (18), doi:10.1029/2004gl020876.

Grell, G. A. and Freitas, S. R.: A scale and aerosol aware stochastic convective parameterization for weather and air quality modeling, Atmos. Chem. Phys., 14, 5233–5250, https//doi.org/10.5194/acp-14- 5233-2014, 2014.

Guenther, A., Karl, T., Harley, P., Wiedinmyer, C., Palmer, P. I., and Geron, C. (2006). Estimates of global terrestrial isoprene emissions using MEGAN (Model of Emissions of Gases and Aerosols from Nature), *Atmos. Chem. Phys.*, 6, 3181–3210, https//doi.org/10.5194/acp-6-3181-2006.

Guenther, A. B., Jiang, X., Heald, C. L., Sakulyanontvittaya, T., Duhl, T., Emmons, L. K., and Wang, X. (2012). The Model of Emissions of Gases and Aerosols from Nature version 2.1 (MEGAN2.1): an extended and updated framework for modeling biogenic emissions. *Geosci. Model Dev*., 5, 1471–1492, https//doi.org/10.5194/gmd-5-1471-2012.

Gustafsson, O., and Ramanathan, V. (2016). Convergence on climate warming by black carbon aerosols. *P. Natl. Acad. S*ci. *USA*, 113, 4243–4245, https//doi.org/10.1073/pnas.1603570113.

Hansen, J., and Nazarenko, L. (2004). Soot climate forcing via snow and ice albedos. *PNAS*, 101 (2), 423-428, https//doi.org/10.1073/pnas.2237157100.

Hua, W., Lou, S., Huang, X., Xue, L., Ding, K., Wang, Z., and Ding, A. (2024). Diagnosing uncertainties in global biomass burning emission inventories and their impact on modeled air pollutants, *Atmos. Chem. Phys.*, https//doi.org/10.5194/acp-24-6787-2024.

Hecobian, A., Zhang, X., Zheng, M., Frank, N., Edgerton, E. S., and Weber, R. J. (2010). Water-Soluble Organic Aerosol material and the light-absorption characteristics of aqueous extracts measured over the Southeastern United States. Atmos. *Chem. Phys*., 10, 5965–5977, https//doi.org/10.5194/acp-10-5965-2010.

Hems, R. F., Schnitzler, E. G., Bastawrous, M., Soong, R., Simpson, A. J., and Abbatt, J. P. D. (2020). Aqueous Photoreactions of Wood Smoke Brown Carbon. *ACS Earth Space Chem.*, 4, 1149–1160, https://doi.org/10.1021/acsearthspacechem.0c00117.

Hems, R. F., Schnitzler, E. G., Liu-Kang, C., Cappa, C. D., and Abbatt, J. P. D. (2021). Aging of Atmospheric Brown Carbon Aerosol. *ACS Earth Space Chem*., 5, 722–748, https//doi.org/10.1021/acsearthspacechem.0c00346e.

Holben, B. N., Tanré, D., Smirnov, A., Eck, T. F., Slutsker, I., Abuhassan, N., Newcomb, W. W., Schafer, J. S., Chatenet, B., Lavenu, F., Kaufman, Y. J., Vande Castle, J., Setzer, A., Markham, B., Clark, D., Frouin, R., Halthore, R., Karneli, A., O'Neill N. T., Pietras, C., Pinker, R. T., Voss, K., and Zibordi, G. (2001). An emerging ground-based aerosol climatology: Aerosol Optical Depth from AERONET. *J. Geophys. Res*., 106(D11), 12067–12097. https//doi.org/10.1029/2001JD900014.

Hong, S.-Y., Noh, S.-Y., and Dudhia, J. (2006). A new vertical diffusion package with an explicit treatment of entrainment processes. *Mon. Weather Rev*., 134, 2318–2341, https//doi.org/10.1175/MWR3199.1.

Iacono, M. J., Delamere, J. S., Mlawer, E. J., Shephard, W., Clough, S. A., and Collins, W. D. (2008). Radiative forcing by long-lived greenhouse gases: Calculations with the AER radiative transfer models, *J. Geophys. Res.*, 113, https//doi.org/10.1029/2008JD009944.

IPCC (2021). *Climate Change 2021. Physical Science Basis. Contribution of Working Group I to the Sixth Assessment Report of the Intergovernmental Panel on Climate Change*, Cambridge UK and New York, NY, USA: Cambridge University Press.

Jacobson, M. Z. (2000). A physically-based treatment of elemental carbon optics: Implications for global direct forcing of aerosols. *Geophysical Research Letters*, 27, 217–220. https://doi.org/10.1029/1999GL010968

Jacobson, M. Z. (2001). Global direct radiative forcing due to multicomponent anthropogenic and natural aerosols. *Journal of Geophysical Research*, 106, 1551–1568.

Jo, D. S., Park, R. J., Lee, S., Kim, S.-W., and Zhang, X. (2016). A global simulation of brown carbon: implications for photochemistry and direct radiative effect, *Atmos. Chem. Phys.*, 16, 3413–3432, https//doi.org/10.5194/acp-16-3413-2016.

Kaiser, J. W., Heil, A., Andreae, M. O., Benedetti, A., Chubarova, N., Jones, L., Morcrette, J.-J., Razinger, M., Schultz, M. G., Suttie, M., and van der Werf, G. R. (2012). Biomass burning emissions estimated with a global fire assimilation system based on observed fire radiative power. *Biogeosciences*, 9, 527–554, https//doi.org/10.5194/bg-9-527-2012.

Kasthuriarachchi, N. Y., Rivellini, L.-H., Adam, M. G., and Lee, A. K. Y. (2020). Light Absorbing Properties of Primary and Secondary Brown Carbon in a Tropical Urban Environment. *Envir. Sci. Tech*., 54(17), 10808-10819, https//doi.org/10.1021/acs.est.0c02414.

Kaufman, Y. J., Tanré, D., Remer, L. A., Vermote, E. F., Chu, A., and Holben, B. N. (1997). Operational remote sensing of tropospheric aerosol over land from EOS moderate resolution imaging spectroradiometer. *J. Geophys. Res*., 102(D14), 17051–17067, https//doi.org/10.1029/96JD03988.

Kirchstetter, T. W., and Thatcher, T. L. (2012). Contribution of organic carbon to wood smoke particulate matter absorption of solar radiation, *Atmos. Chem. Phys.*, 12, 6067–6072, https//doi.org/10.5194/acp-12-6067-2012.

Kompalli, S. K., Babu, S. S., Ajith, T.C., Moorthy, K. K., Satheesh, S. K., Boopathy, R., Das, T., Liu, D., Allan, J., and Coe, H. (2023). Aging of biomass burning emissions in the Indo-Gangetic Plain outflow: Implications for black carbon light-absorption enhancement, *Atmos. Res*., 294, 106949, https//doi.org/10.1016/j.atmosres.2023.106949.

Kong, Y., Zhi, G., Jin, W., Zhang, Y., Shen, Y., Li, Z., Sun, J., and Ren, Y. (2024). A review of quantification methods for light absorption enhancement of black carbon aerosol, *Sci. Tot. Env.*, 924, 171539, https//doi.org/10.1016/j.scitotenv.2024.171539.

Konovalov, I. B., Golovushkin, N. A., Beekmann, M., Siour, G., Zhuravleva, T. B., Nasrtdinov, I. M., and Kuznetsova, I. N. (2023). On the importance of the model representation of organic aerosol in simulations of the direct radiative effect of Siberian biomass burning aerosol in the eastern Arctic, *Atmos. Envir.*, 309, 119910, https//doi.org/10.1016/j.atmosenv.2023.119910.

Konovalov, I. B., Golovushkin, N. A., and Beekmann, M. (2024a). Wildfire-smoke-precipitation interactions in Siberia: Insights from a regional model study. *Sci. Tot. Env.*, 951, 175518, https//doi.org/10.1016/j.scitotenv.2024.175518.

Konovalov, I.B., Golovushkin, N. A. (2024b). Model Analysis of Origination of Semidirect Radiative Effect of Siberian Biomass Burning Aerosol in the Arctic. *Atmos. Ocean. Opt.,* 37, 382–393, https://doi.org/10.1134/S1024856024700477

Kuhns, H., Knipping, E. M., and Vukovich, J. M. (2005). Development of a United States–Mexico Emissions Inventory for the Big Bend Regional Aerosol and Visibility Observational (BRAVO) Study, *J. Air Waste Manage. Assoc.*, 55, 677–692, https//doi.org/10.1080/10473289.2005.10464648.

Lack, D. A., Langridge, J. M., Bahreini, R., Cappa, C. D., Middlebrook, A. M., and Schwarz, J. P. (2012). Brown carbon and internal mixing in biomass burning particles. *P. Natl. Acad. Sci. USA*, 109, 14802–14807, https//doi.org/10.1073/pnas.1206575109.

Lambe, A. T., Cappa, C. D., Massoli, P., Onasch, T. B., Forestieri, S. D.. Martin, A. T., Cummings, M. J., Croasdale, D. R., Brune, W. H., Worshop, D. R., and Davidovits, P. (2013). Relationship between oxidation level and optical properties of secondary organic aerosol, *Environ. Sci. Technol*., 47, 6349–6357, https//doi.org/10.1021/es401043j.

Lan, Z. J., Huang, X. F., Yu, K.Y., Sun, T.L., Zeng, L.W., Hu, M. (2013). Light absorption of black carbon aerosol and its enhancement by mixing state in an urban atmosphere in South China. *Atmos. Environ.*, 69, 118-123, doi.org/10.1016/j.atmosenv.2012.12.009.

Laskin, A., Laskin, J., and Nizkorodov, S. A. (2015). Chemistry of Atmospheric Brown Carbon, *Chem. Rev.*, 115, 4335–4382, https//doi.org/10.1021/cr5006167.

Lee, H. J., Aiona, P. K., Laskin, A., Laskin, J., and Nizkorodov, S. A. (2014). Effect of Solar Radiation on the Optical Properties and Molecular Composition of Laboratory Proxies of Atmospheric Brown Carbon, *Envir. Scie. Tech.*, 48, 10217-10226, https//doi.org/10.1021/es502515r.

Lesins, G., Chylek, P., and Lohmann, U. (2002). A study of internal and external mixing scenarios and its effect on aerosol optical properties and direct radiative forcing, *J. Geophys. Res*., 107, 4094, https//doi.org/10.1029/2001JD000973.

Levy, R., Hsu, C., et al. (2015). MODIS Atmosphere L2 Aerosol Product. NASA MODIS Adaptive Processing System, Goddard Space Flight Center, USA: doi:10.5067/MODIS/MYD04_L2.061.

Li, F., Lawrence, D. M., and Bond-Lamberty, B. (2017). Impact of fire on global land surface air temperature and energy budget for the 20th century due to changes within ecosystems. *Environ. Res. Lett.*, 12, 044014, https//doi.org/:10.1088/1748-9326/aa6685.

Lin, G., Penner, J. E., Flanner, M. G., Sillman, S., Xu, L., and Zhou, C. (2014). Radiative forcing of organic aerosol in the atmosphere and on snow: Effects of SOA and brown carbon, J. *Geophys. Res.*, 119, 7453–7476, https//doi.org/10.1002/2013JD021186.

Lin, P., Liu, J., Shilling, J. E., Kathmann, S. M., Laskin, J., and Laskin, A. (2015). Molecular characterization of brown carbon (BrC) chromophores in secondary organic aerosol generated from photo-oxidation of toluene, *Phys. Chem. Chem. Phys*., 17, 23312-23325, https//doi.org/10.1039/C5CP02563J.

Linares, M., and Ni-Meister, W. (2024). Impact of Wildfires on Land Surface Cold Season Climate in the Northern High-Latitudes: A Study on Changes in Vegetation, Snow Dynamics, Albedo, and Radiative Forcing. *Remote Sens.*, 16, 1461, https://doi.org/10.3390/rs16081461.

Liu, P. F., Abdelmalki, N., Hung, H.-M., Wang, Y., Brune, W. H., and Martin, S. T. (2015). Ultraviolet and visible complex refractive indices of secondary organic material produced by photooxidation of the aromatic compounds toluene and m-xylene, *Atmospheric Chem. Phys.*, 15, 1435–1446, https://doi.org/10.5194/acp-15-1435-2015.

Liu, J., Lin, P., Laskin, A., Laskin, J., Kathmann, S. M., Wise, M., Caylor, R., Imholt, F., Selimovic, V., and Shilling, J. E. (2016). Optical properties and aging of light-absorbing secondary organic aerosol, *Atmos. Chem. Phys*., 16, 12815–12827, https//doi.org/10.5194/acp-16-12815-2016.

Liu, D., Whitehead, J., Alfarra, M., reyes-Villegas, E., Spracklen, D. V., Reddington, C. L., Kong, S., Williams, P. I., Ting Y.-C., Haslett, S., Taylor, J. W., Flynn, M. J., Morgan, W. T., McFiggans, G., Coe, H, and Allan, J. D. (2017). Black-carbon absorption enhancement in the atmosphere determined by particle mixing state, *Nature Geosci.*, 10, 184–188, https//doi.org/10.1038/ngeo2901.

Liu, Y., Zhang, K., Qian, Y., Wang, Y., Zou, Y., Song, Y., Wan, H., Liu, X., and Yang, X.-Q. (2018). Investigation of short-term effective radiative forcing of fire aerosols over North America using nudged hindcast ensembles, *Atmos. Chem. Phys*., 18, 31-47, https//doi.org/10.5194/acp-18-31-2018

Lukács, H., Gelencsér, A., Hammer, S., Puxbaum, H., Pio, C., Legrand, M., Kasper-Giebl, A., Handler, M., Limbeck, A., and Simpson, A. (2007). Seasonal trends and possible sources of brown carbon based on 2-year aerosol measurements at six sites in Europe, *J. Geophys. Res*., 112, D23S18, https//doi.org/10.1029/2006JD008151, 2007.

Mailler, S., Menut, L., di Sarra, A. G., Becagli, S., Di Iorio, T., Bessagnet, B., Briant, R., Formenti, P., Doussin, J.-F., Gómez-Amo, J. L., Mallet, M., Rea, G., Siour, G., Sferlazzo, D. M., Traversi, R., Udisti, R., and

Turquety, S. (2016). On the radiative impact of aerosols on photolysis rates: comparison of simulations and observations in the Lampedusa island during the ChArMEx/ADRIMED campaign, *Atmos. Chem. Phys*., 16, 1219–1244, https//doi.org/10.5194/acp-16-1219-2016.

Mailler, S., Menut, L., Khvorostyanov, D., Valari, M., Couvidat, F., Siour, G., Turquety, S., Briant, R., Tuccella, P., Bessagnet, B., Colette, A., Létinois, L., Markakis, K., and Meleux, F. (2017). CHIMERE-2017: from urban to hemispheric chemistry-transport modeling, *Geosci. Model Dev.*, 10, 2397–2423, https//doi.org/10.5194/gmd-10-2397-2017.

Menut, L., Schmechtig, C., and Marticorena, B. (2005). Sensitivity of the sandblasting fluxes calculations to the soil size distribution accuracy, *J. Atmos. Ocean. Technol.*, 22, 1875–1884, https//doi.org/10.1175/JTECH1825.1.

Menut, L., Flamant, C., Turquety, S., Deroubaix, A., Chazette, P., and Meynadier, R. (2018). Impact of biomass burning on pollutant surface concentrations in megacities of the Gulf of Guinea, *Atmos. Chem. Phys.*, 18, 2687–2707, https//doi.org/10.5194/acp18-2687-2018.

Menut L., Bessagnet, B., Mailler, S., Pennel, R., Siour, G. (2020). Impact of lightning NOx emissions on atmospheric composition and meteorology in Africa and Europe, *Atmospheres*, 11, 1128; https//doi.org/10.3390/atmos11101128.

Menut, L., Bessagnet, B., Briant, R., Cholakian, A., Couvidat, F., Mailler, S., Pennel, R., Siour, G., Tuccella, P., Turquety, S., and Valari, M. (2021). The CHIMERE v2020r1 online chemistry-transport model, *Geosci. Model Dev*., 14, 6781–6811, doi:10.5194/gmd-14-6781-2021.

Menut, L., Cholakian, A., Siour, G., Lapere, R., Pennel, R., Mailler, S., and Bessagnet, B. (2023). Impact of Landes forest fires on air quality in France during the 2022 summer, *Atmos. Chem. Phys*., 23, 7281–7296, https//doi.org/10.5194/acp-23-7281-2023.

Meredith, M., et al. (2019). Polar Regions. In: *IPCC Special Report on the Ocean and Cryosphere in a Changing Climate* [H.-O. Pörtner, D.C. Roberts, V. Masson-Delmotte, P. Zhai, M. Tignor, E. Poloczanska, K. Mintenbeck, A. Alegría, M. Nicolai, A. Okem, J. Petzold, B. Rama, N.M. Weye.

Methymaki, G., Bossioli, E., Boucouvala, D., Nenes, A., and Tombrou, M. (2023). Brown carbon absorption in the Mediterranean basin from local and long-range transported biomass burning air masses. *Atmos. Environ*., 306, 119822, https//doi.org/10.1016/j.atmosenv.2023.119822.

Mie, G. (1908). Beiträge zur Optik trüber Medien, speziell kolloidaler Metallösungen, *Ann. Phys*., 330, 377–445, https://doi.org/10.1002/andp.19083300302.

Mischenko, M., Travis, L. D., and Lacis, A. A. (2002). *Scattering, absorption and emission of light by small particles*, Cambridge, UK: Cambridge University Press.

Nenes, A., Pilinis, C., and Pandis, S. (1998). ISORROPIA: A new thermodynamic model for inorganic multicomponent atmospheric aerosols, *Aquatic Geochem*., 4, 123–152, https//doi.org/10.1023/A:1009604003981.

Moise, T., Flores, J. M., and Rudich, Y. (2025). Optical Properties of Secondary Organic Aerosols and Their Changes by Chemical Processes, *Chem. Rev.*, 115, 4400–4439, https://doi.org/10.1021/cr5005259.

Park, R. J., Jacob, D. J., Chin, M., and Martin, R. V. (2003). Sources of carbonaceous aerosols over the United States and implications for natural visibility, *J. Geophys. Res*., 108, 4355, https://doi.org/10.1029/2002JD003190.

Palacios-Peña, L., Jiménez-Guerrero, P., Baró, R., Balzarini, A., Bianconi, R., Curci, G., Landi, T. C., Pirovano, G., Prank, M., Riccio, A., Tuccella, P., and Galmarini, S. (2019). Aerosol optical properties over Europe: an evaluation of the AQMEII Phase 3 simulations against satellite observations, *Atmos. Chem. Phys.*, 19, 2965–2990, https://doi.org/10.5194/acp-19-2965-2019.

Potter, S., Copperdock, S., Veraverbeke, S., Walker, X., Mack, M.C., Goetz, S. J., Baltzer, J., Bourgeau-Chevez, L., Burrel, A., Dieleman, C., French, N., Hantson, S., Hoy, E. E., Jenkins, L., Johnstone, J. F., Kane, E. S., Natali, S. M., Randerson, J. T., Turetsky, M. R., Whitman, E. Wiggins, E., and Rogers, B. M. (2023). Burned area and carbon emissions across northwestern boreal North America from 2001–2019. *Biogeosciences*, 20(13), 2785-2804, https://doi.org/:10.5194/bg-20-2785-2023.

Price, C., and Rind, D. (1993). What determines the cloud-to-ground lightning fraction in thunderstorms?, *Geophys. Res. Lett.*, 20, 463– 466, https://doi.org/10.1029/93GL00226.

Park, R. J., Kim, M. J., Jeong, J. I, Youn, D., and Kim, S. (2010). A contribution of brown carbon aerosol to the aerosol light absorption and its radiative forcing in East Asia. *Atmos. Environ*., 44, 1414–1421, https://doi.org/10.1016/j.atmosenv.2010.01.042.

Ramnarine, E., Kodros, J. K., Hodshire, A. L., Lonsdale, C. R., Alvarado, M. J., and Pierce, J. R. (2019). Effects of near-source coagulation of biomass burning aerosols on global predictions of aerosol size distributions and implications for aerosol radiative effects. *Atmos. Chem. Phys*., 19, 6561-6577, https://doi.org/10.5194/acp-19-6561-2019.

Randerson, J. T. et al. (2006). The Impact of Boreal Forest Fire on Climate Warming. *Science*, 314, 1130-1132, DOI:10.1126/science.1132075.

Rathod, T. D., Sahu, S. K., Tiwari, M., Bhangare, R.C., and Ajmal, P.Y. (2021). Light absorption enhancement due to mixing in black carbon and organic carbon generated during biomass burning. *Atmos. Pollut. Res*., 12, 101236, https://doi.org/10.1016/j.apr.2021.101236.

Riemer, N., Ault, A. P., West, M., Craig, R. L., & Curtis, J. H. (2019). Aerosol mixing state: Measurements, modeling, and impacts. *Reviews of Geophysics*, 57, 187–249. https://doi.org/10.1029/2018RG000615.

Romshoo, B., Pöhlker, M., Wiedensohler, A., Pfeifer, S., Saturno, J., Nowak, A., Ciupek, K., Quincey, P., Vasilatou, K., Ess, M. N., Gini, M., Eleftheriadis, K., Robins, C., Gaie-Levrel, F., and Müller, T. (2022). Importance of size representation and morphology in modelling optical properties of black carbon: comparison between laboratory measurements and model simulations, *Atmos. Meas. Tech*., 15, 6965–6989, https://doi.org/10.5194/amt-15-6965-2022.

Saleh, R., Robinson, E. S., Tkacik, D. S., Ahern, A. T., Liu, S., Aiken, A. C., Sullivan, R., C., Presto, A. A., Dubey, M. K., Yokelson, R. J., Donahue, N. M., and Robinson, A. L. (2014). Brownness of organics in aerosols from biomass burning linked to their black carbon content, *Nat. Geosci.*, 7, 647–650, https://doi.org/10.1038/ngeo2220.

Saleh, R., Marks, M., Heo, J., Adams, P. J., Donahue, N. M., and Robinson, A. L. (2015). Contribution of brown carbon and lensing to the direct radiative effect of carbonaceous aerosols from biomass and biofuel burning emissions, *J. Geophys. Res.-Atmos*., 120, 10285–10296, https://doi.org/10.1002/2015JD023697.

Schnitzler, E. G., Liu, T., Hems, R. F., and Abbatt, J. P. D. (2020). Emerging investigator series: heterogeneous OH oxidation of primary brown carbon aerosol: effects of relative humidity and volatility. *Environ. Sci.-Proc. Imp.*, 22, 2162–2171, https://doi.org/10.1039/D0EM00311E.

Schwarz, J. P., Gao, R. S., Spackman, J. R., Watts, L. A., Thomson, D. S., Fahey, D. W., Ryerson, T. B., Peischl, J., Holloway, J. S., Trainer, M., Frost, G. J., Baynard, T., Lack, D. A., de Gouw, J. A., Warneke, C., and Del Negro, L. A. (2008). Measurement of the mixing state, mass, and optical size of individual black carbon particles in urban and biomass burning emissions, *Geophys. Res. Lett.*, 35, L13810, https://doi.org/10.1029/2008GL033968.

Seinfeld, J. N., and Pandis, S. N. (2016). *Atmospheric Chemistry and Physics: From Air Pollution to Climate Change*. 3th Edition, New York, US: John Wiley & Sons.

Sinyuk, A., Holben, B. N., Eck, T. F., Giles, D. M., Slutsker, I., Korkin, S., Schafer, J. S., Smirnov, A., Sorokin, M., and Lyapustin, A. (2020). The AERONET Version 3 aerosol retrieval algorithm, associated uncertainties and comparisons to Version 2, *Atmos. Meas. Tech.*, 13, 3375–3411, https://doi.org/10.5194/amt-13-3375-2020.

Sofiev, M., Ermakova, T., and Vankevich, R. (2012). Evaluation of the smoke-injection height from wild-land fires using remote-sensing data. *Atmos. Chem. Phys.*, 12, 1995–2006, https://doi.org/10.5194/acp-12-1995-2012.

Soulie, A., Granier, C., Darras, S., Zilbermann, N., Doumbia, T., Guevara, M., Jalkanen, J.-P., Keita, S., Liousse, C., Crippa, M., Guizzardi, D., Hoesly, R., and Smith, S. J. (2024). Global anthropogenic emissions (CAMS-GLOB-ANT) for the Copernicus Atmosphere Monitoring Service simulations of air quality forecasts and reanalyses, *Earth Syst. Sci. Data*, 16, 2261–2279, https://doi.org/10.5194/essd-16-2261-2024.

Tanré, D., Kaufman, Y. J., Herman, M., and Mattoo, S. (1997). Remote sensing of aerosol properties over oceans using the MODIS/EOS spectral radiances. *J. Geophys. Res*., 102(D14), 16971–16988, https://doi.org/10.1029/96JD03437.

Thompson, G., Field, P. R., Rasmussen, R. M., and Hall, W. D. (2008). Explicit Forecasts of Winter Precipitation Using an Improved Bulk Microphysics Scheme. Part II: Implementation of a New Snow Parameterization. *Mon. Weather Rev.*, 136(12), 5095-5115, https://doi.org/10.1175/2008MWR2387.1.

Toon, O. B., and Ackerman, T. P. (1981) Algorithms for the calculation of scattering by stratified spheres. *Appl. Opt*., 20, 3657–3660, https://doi.org/10.1364/AO.20.003657.

Torres, O., Decae, R., Veefkind, J. P., and de Leeuw, G. (2002). *OMI aerosol retrieval algorithm, in OMI Algorithm Theoretical Basis Document: Clouds, Aerosols, and Surface UV Irradiance, vol. 3, version 2* (ATBD-OMI-03, pp. 47–71) NASA Goddard Space Flight Cent., Greenbelt, Md. (Available at https://eospso.nasa.gov/sites/default/files/atbd/ATBD-OMI-03.pdf)

Torres, O., A. Tanskanen, B. Veihelmann, C. Ahn, R. Braak, P. K. Bhartia, P. Veefkind, and P. Levelt (2007). Aerosols and surface UV products from Ozone Monitoring Instrument observations: An overview. *J. Geophys. Res.*, 112, D24S47, doi:10.1029/2007JD008809.

Torres, O., Ahn, C., and Chen, Z. (2013). Improvements to the OMI near-UV aerosol algorithm using A-train CALIOP and AIRS observations, *Atmos. Meas. Tech.*, 6, 3257–3270, https://doi.org/10.5194/amt-6-3257-2013.

Tuccella, P., Thomas, J. L., Law, K. S., Raut, J.-C., Marelle, L., Roiger, A., Weinzierl, B., Denier van der Gon, H. A. C., Schlager, H., and Onishi, T. (2017). Air pollution impacts due to petroleum extraction in the Norwegian Sea during the ACCESS aircraft campaign, *Elem. Sci. Anth.*, 5, 25, https://doi.org/10.1525/elementa.124.

Tuccella, P., Menut, L., Briant, R., Deroubaix, A., Khvorostyanov, D., Mailler, S., Siour, G., and Turquety, S. (2019). Implementation of Aerosol-Cloud Interaction within WRF-CHIMERE Online Coupled Model: Evaluation and Investigation of the Indirect Radiative Effect from Anthropogenic Emission Reduction on the Benelux Union. *Atmosphere*, 10(1), 20, https://doi.org/10.3390/atmos10010020.

Tuccella, P., Curci, G., Pitari, G., Lee, S., and Jo, D. S. (2020). Direct radiative effect of absorbing aerosols: sensitivity to mixing state, brown carbon and dust refractive index and shape, *J. Geophys. Res.*, 125, e2019JD030967, https://doi.org/10.1029/2019JD030967.

Tuccella, P., Pitari, G., Colaiuda, V., Raparelli, E., and Curci, G. (2021). Present-day radiative effect from radiation-absorbing aerosols in snow, *Atmos. Chem. Phys*., 21, 6875–6893, https://doi.org/10.5194/acp-21-6875-2021.

Updyke, K. M., Nguyen, T. B., and Nizkorodov, S. A. (2012). Formation of brown carbon via reactions of ammonia with secondary organic aerosols from biogenic and anthropogenic precursors, *Atmos. Env*, 63, 22–31, https://doi.org/10.1016/j.atmosenv.2012.09.012.

van Bellen S., Garneau, M., and Bergeron, Y. (2010). Impact of Climate Change on Forest Fire Severity and Consequences for Carbon Stocks in Boreal Forest Stands of Quebec, Canada: a Synthesis. *Fire Ecol*., 6, 16-44, https://doi.org/10.4996/fireecology.0603016.

Veira, A., Kloster, S., Wilkenskjeld, S., and Remy, S. (2015). Fire emission heights in the climate system – Part 1: Global plume height patterns simulated by ECHAM6-HAM2, *Atmos. Chem. Phys.*, 15, 7155–7171, https://doi.org/10.5194/acp-15-7155-2015.

Veraverbeke, S. et al. (2017). Lightning as a major driver of recent large fire years in North American boreal forests. *Nature Climate Change*, 7 (7), 529–534, doi:10.1038/nclimate3329.

Walker J.X., Rogers, B. M., Baltzer, J. L., Cumming, S. G., Day, N. J., Goetz, S. J., Johnstone, J. F., Schuur, E. A. G., Turetsky, M. R., and Mack M. C. (2018). Cross-scale controls on carbon emissions from boreal forest megafires, *Glob. Change. Biol*., 24(9), 4251-4265, https://doi.org/10.1111/gcb.14287.

Wang, X., Heald, C. L., Ridley, D. A., Schwarz, J. P., Spackman, J. R., Perring, A. E., Coe, H., Liu, D., and Clarke, A. D. (2014). Exploiting simultaneous observational constraints on mass and absorption to estimate the global direct radiative forcing of black carbon and brown carbon, *Atmos. Chem. Phys*., 14, 10989–11010, https://doi.org/10.5194/acp-14-10989-2014.

Wang, X., Zhang, L., and Moran, M. D. (2014). Development of a new semi-empirical parameterization for below-cloud scavenging of size-resolved aerosol particles by both rain and snow, *Geosci. Model Dev*., 7, 799–819, https://doi.org/10.5194/gmd-7-799-2014.

Wang, X., Heald, C. L., Sedlacek, A. J., de Sá, S. S., Martin, S. T., Alexander, M. L., Watson, T. B., Aiken, A. C., Springston, S. R., and Artaxo, P. (2016). Deriving brown carbon from multiwavelength absorption measurements: method and application to AERONET and Aethalometer observations, *Atmos. Chem. Phys*., 16, 12733–12752, https://doi.org/10.5194/acp-16-12733-2016.

Wang, X., Heald, C. L., Liu, J., Weber, R. J., Campuzano-Jost, P., Jimenez, J. L., Schwarz, J. P., and Perring, A. E. (2018). Exploring the observational constraints on the simulation of brown carbon, *Atmos. Chem. Phys*., 18, 635–653, https://doi.org/10.5194/acp-18-635-2018.

Wang, Y., Li, W., Huang, J., Liu, L., Pang, Y., He C., He, C., Liu, F., Liu, D., Bi, L., Zhang, X., and Shi, Z. (2021). Nonlinear enhancement of radiative absorption by black carbon in response to particle mixing structure. *Geophys. Res. Lett*., 48, e2021GL096437, https://doi.org/10.1029/2021GL096437.

Wang, J., Wang, J., Cai, R., Liu, C., Nie, W., Wang, J., Moteki, N., Zaveri, R. A., Huang, X., Ma, N., Chen, G., Wang, Z., Jin, Y., Cai, J., Zhang, Y., Chi, X., Holanda, B. A., Xing, J., Liu, T., Qi, X., Wang, Q., Pöhlker, C., Su, H., Cheng, Y., Wang, S., Hao, J., Andreae, M. O., and Ding, A. (2023). Unified theoretical framework for black carbon mixing state allows greater accuracy of climate effect estimation, N*at. Commun*., 14, 2703, , 2023.https://doi.org/10.1038/s41467-023-38330-x.

Wesely, M. (1989). Parameterization of Surface Resistances to Gaseous Dry Deposition in Regional-Scale Numerical Models, *Atmos. Environ*., 23, 1293–1304, https://doi.org/10.1016/0004-6981(89)90153-4.

Wild, O., Zhu, X., Prather, and Fast-J, M. J. (2000). Accurate Simulation of In- and Below-Cloud Photolysis in Tropospheric Chemical Models. *J. Atmos. Chem*., 37, 245–282, https://doi.org/10.1023/A:1006415919030.

Zeng, L., Tan, T., Zhao, G., Du, Z., Hu, S., Shang, D., and Hu, M. (2024). Overestimation of black carbon light absorption due to mixing state heterogeneity. *npj Clim. Atmos. Sci*., 7, 2, https://doi.org/10.1038/s41612-023-00535-8.

Zhang, L., Gong, S., Padro, J., and Barrie, L. (2001). A size-segregated particle dry deposition scheme for an atmospheric aerosol module. *Atmos. Environ*., 35(3), 549–560, https://doi.org/10.1016/S1352-2310(00)00326-5.

Zhang, Y., Forrister, H., Liu, J., Dibb, J., Anderson, B., Schwarz, J. P., Perring, A. E., Jimenez, J. L., Campuzano-Jost, P., Wang, Y., Nenes, A., and Weber R.W. (2017). Top-of-atmosphere radiative forcing affected by brown carbon in the upper troposphere. *Nat. Geosci*., 10, 486–489, https://doi.org/10.1038/ngeo2960, 2017.

Zhang, A., Wang, Y., Zhang, Y., Weber, R. J., Song, Y., Ke, Z., and Zou, Y. (2020). Modeling the global radiative effect of brown carbon: a potentially larger heating source in the tropical free troposphere than black carbon. *Atmos. Chem. Phys*., 20, 1901–1920, https://doi.org/10.5194/acp-20-1901-2020.

Zhao, R., Lee, A. K. Y., Huang, L., Li, X., Yang, F., and Abbatt, J. P. D. (2015). Photochemical processing of aqueous atmospheric brown carbon, *Atmos. Chem. Phys.*, 15, 6087–6100, https://doi.org/10.5194/acp-15-6087-2015.

Zhao, G., Tan, T., Zhu, Y., Hu, M., and Zhao, C. (2021). Method to quantify black carbon aerosol light absorption enhancement with a mixing state index. *Atmos. Chem. Phys*., 21, 18055–18063, https://doi.org/10.5194/acp-21-18055-2021.

Zhong, M., and Jang, M. (2014). Dynamic light absorption of biomass-burning organic carbon photochemically aged under natural sunlight. *Atmos. Chem. Phys*., 14, 1517–1525, https://doi.org/10.5194/acp-14-1517-2014.

Tables

Table 1. Summary of the numerical experiments.

Simulation	Description
CTRL	Control simulation. Default model.
BC_{Eabs}	Only BC absorption enhancement
BEST	BC absorption enhancement and BrC absorption
H-ABS	High absorption scenario: E_{absCS}=1.9, no BB-BrC ageing
L-ABS	Low absorption scenario: E_{absCS}=1.2, all BB-BrC is aged

Table 2. Statistical comparison of the predicted and observed AOD with MODIS at 550 nm, OMI at 354 nm, and AERONET stations at 440 nm.

Database	r	NMB (%)	RMSE	NSE	TS	STDE
MODIS[1]	0.77	-14	0.17	0.57	0.79	0.16
OMI[1]	0.65	-30	0.64	0.35	0.70	0.60
AERONET[2,3]	0.79	-23	0.22	0.58	0.88	0.21
AERONET-R1[2]	0.78	-35	0.47	0.56	0.81	0.44
AERONET-R2[2]	0.77	-20	0.27	0.54	0.88	0.26
AERONET-R3[2]	0.76	-16	0.14	0.54	0.86	0.13

[1]*The comparison is done with monthly average*

[2]*The comparison is done with daily data*

[3]*This comparison is done with all AERONET data*

Table 3. Statistical comparison of the predicted monthly AAOD at 354 nm in CTRL, BC_{Eabs}, and BEST simulations with that and observed by OMI.

Simulation	r	NMB (%)	RMSE	NSE	TS	STDE
CTRL	0.53	-78	0.059	-0.32	0.34	0.044
BC_{Eabs}	0.54	-75	0.058	-0.25	0.41	0.044
BEST	0.50	-55	0.055	-0.14	0.73	0.049

Table 4. Total aerosol and BB average AAOD at 550 nm for June 2023, calculated CTRL and BEST simulations.

	CTRL	BEST	UNCERTAINTY[1]
AAOD	0.0068	0.0089	0.0080/0.0110 (-10/+24%)
BB-AAOD	0.0047	0.0066	0.0057/0.0086 (-14/+30%)

[1]*The uncertainty has been assessed relative to BEST simulation, using L-ABS and H-ABS sensitivity tests.*

Table 5. June 2023 average clear-sky and all-sky TOA DRE (W/m2) of BB calculated from CTRL and BEST simulations.

	CTRL	BEST	UNCERTAINTY[1]
Clear-sky	-3.1	-2.8	-3.0/-2.6 (±7%)
All-sky	-2.1	-1.9	-2.0/-1.8 (±5%)

[1]*The uncertainty has been assessed relative to BEST simulation, using L-ABS and H-ABS sensitivity tests.*

Figures

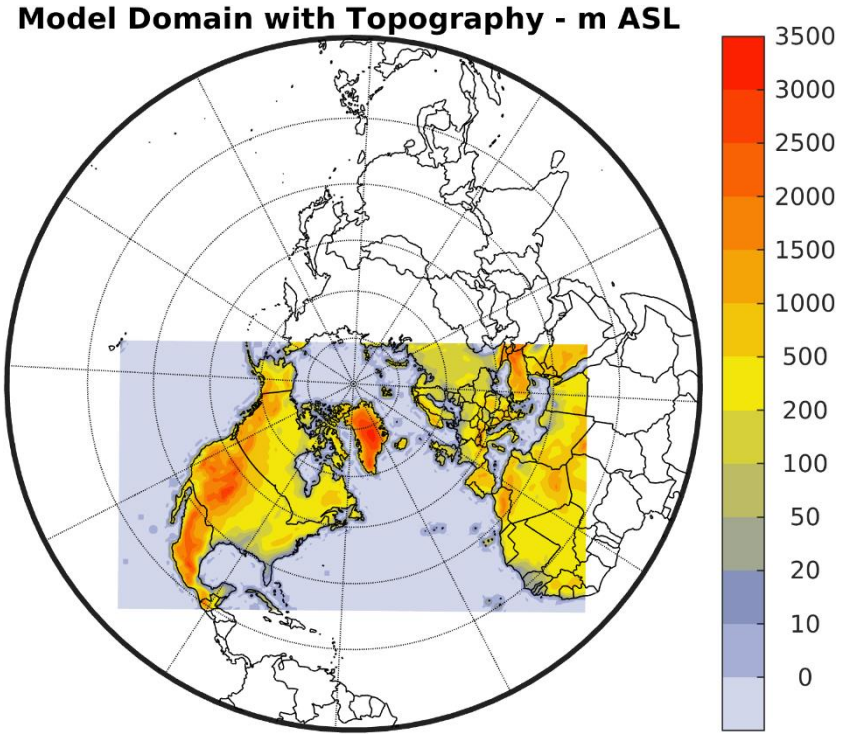

Figure 1: The domain used to run WRF-CHIMERE. The grid had horizontal resolution of 78 km with 189x109 grid points.

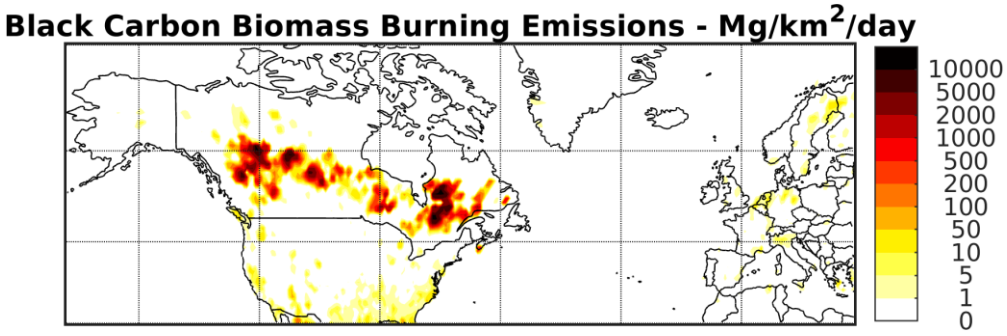

Figure 2: Biomass burning emission flux of black carbon during the month of June 2023 obtained from the CAMS database.

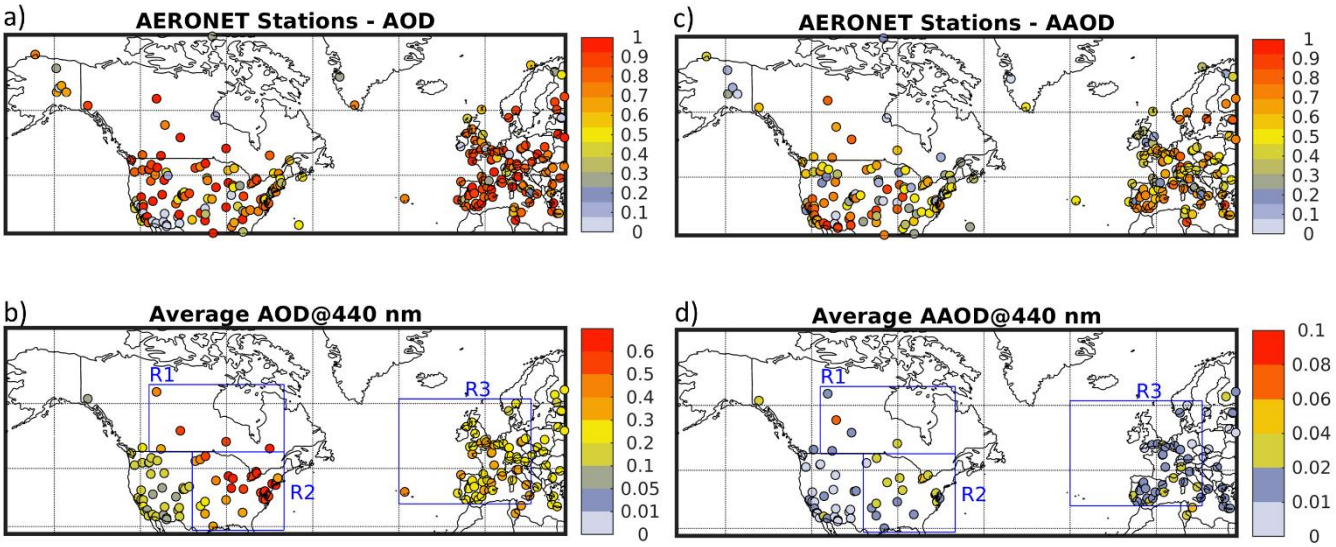

Figure 3: AERONET stations used to evaluate the model simulations. The colour scale represents the fraction of data coverage in June 2023 for the aerosol optical depth (AOD) (a) and the absorption aerosol optical depth (AAOD) (c), and the mean AOD (b) and AAOD (d) at 440 nm measured at AERONET sites. Average AOD is calculated at the stations with at least 75% of monthly data coverage, while monthly AAOD is calculated at sites with at least 55% of data coverage. The regions R1, R2, and R3 outlined by blue rectangles indicate the area most affected by Canadian boreal fires (see Section 2.5).

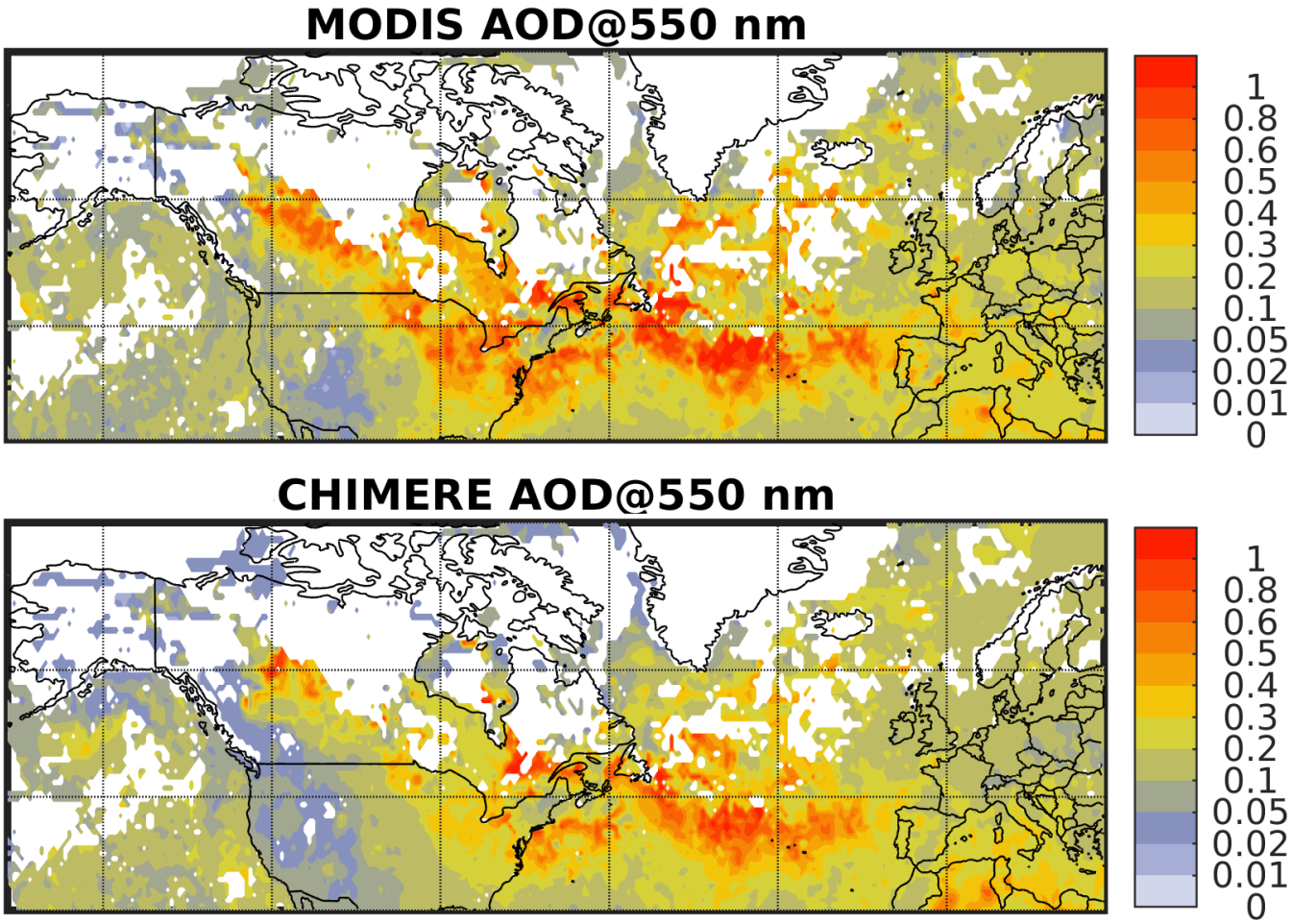

Figure 4: Aerosol optical depth (AOD) monthly average at 550 nm for June 2023, as measured by MODIS (upper panel) and modelled by CHIMERE (lower panel).

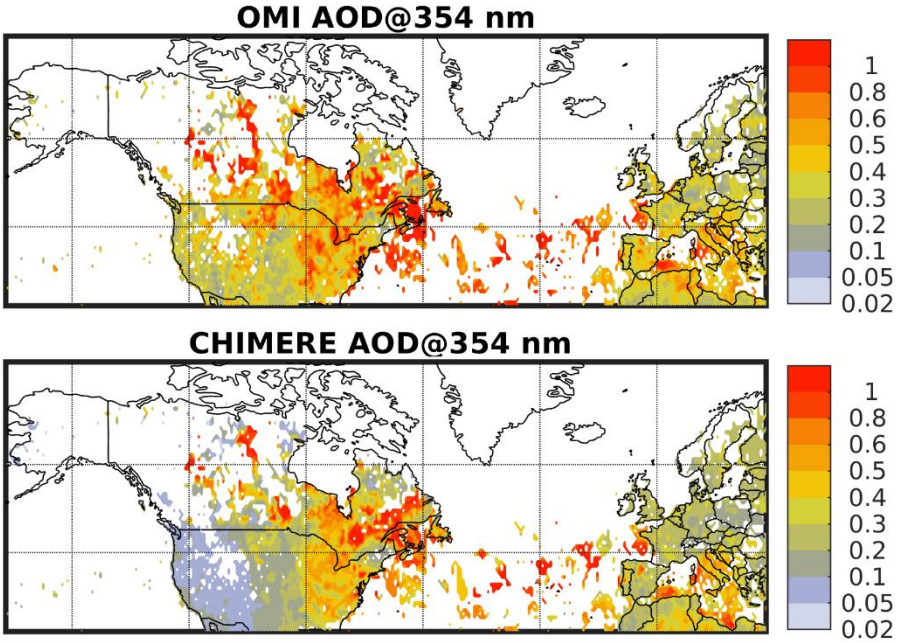

Figure 5: As in Figure 4, but for AOD at 354 nm measured by OMI.

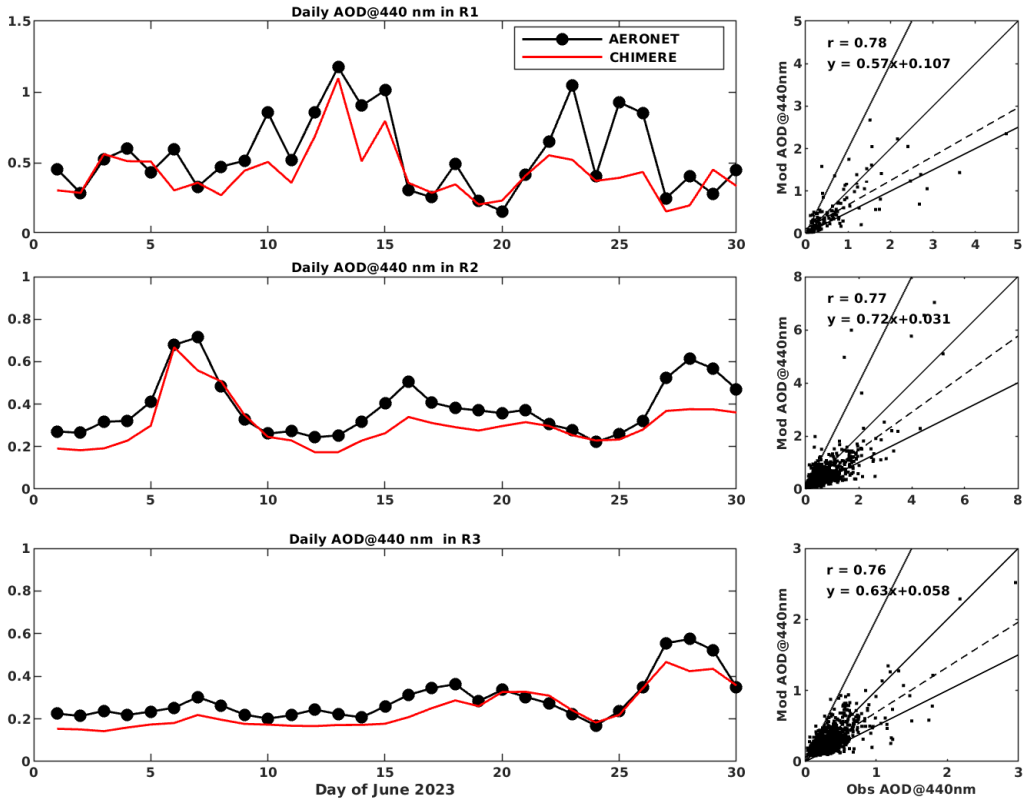

Figure 6. Comparison of modelled and observed aerosol optical depth (AOD) at 440 nm at AERONET sites. The left panels show the predicted and measured daily time series of AOD, averaged across all stations in regions R1, R2, and R3. The right panels present the scatter plots of observed versus predicted daily AOD in R1, R2, and R3. The lines 1:1, 2:1, and best least-squares linear fit shown for reference.

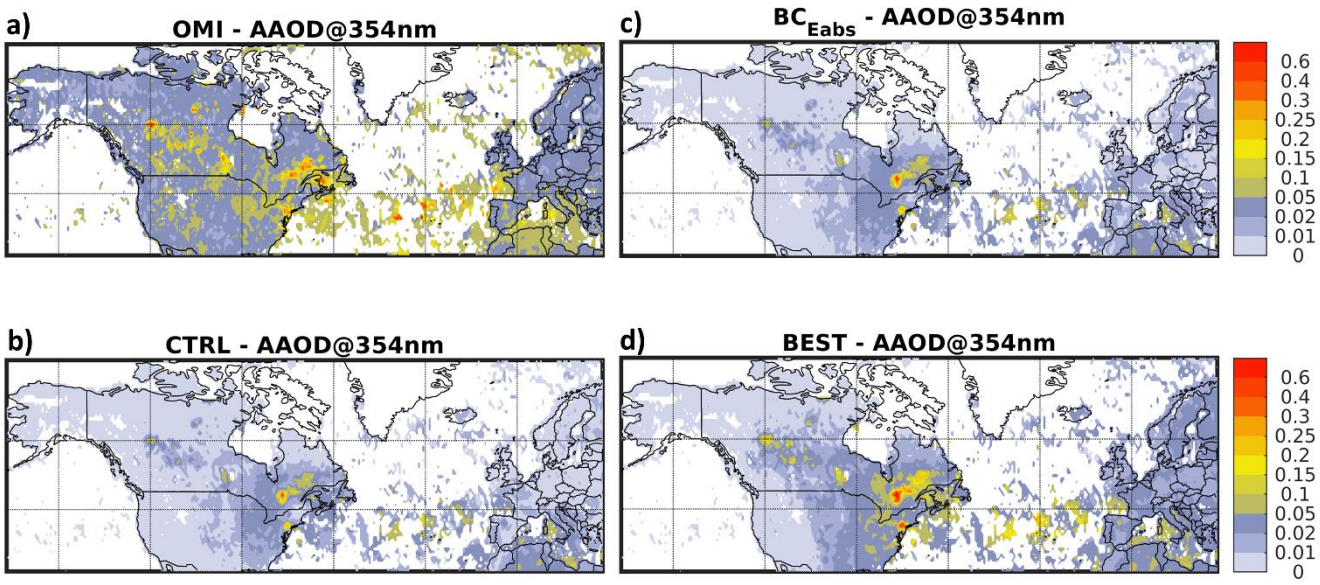

Figure 7: June 2023 monthly average absorption aerosol optical depth (AAOD) at 354 nm, a) as measured by OMI and modelled by CHIMERE in b) CTRL, c) BC_{Eabs}, and d) BEST simulations.

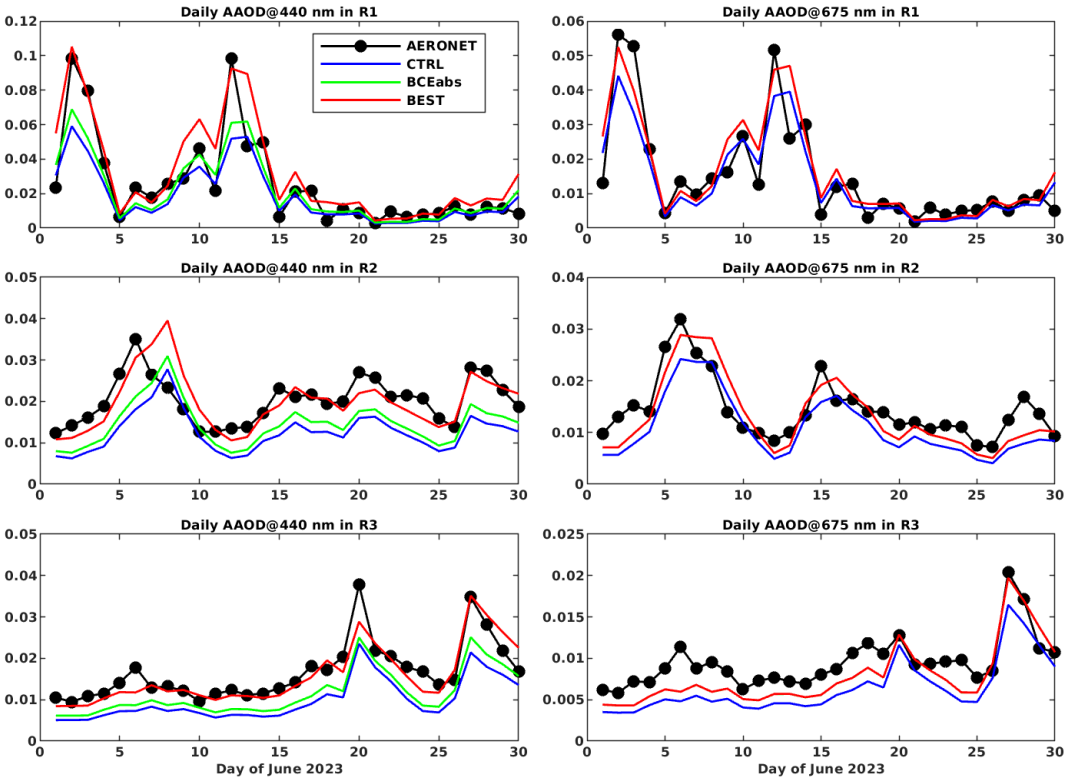

Figure 8. Comparison observed and modelled average time series of absorption aerosol optical depth (AAOD) at 440 (left panels) and 675 nm (right panels), for the CTRL (blue), BC_{Eabs} (green), and BEST (red) simulations at AERONET sites in regions R1, R2, and R3. Please, note that at 675 nm BC_{Eabs}, and BEST give the same results, since BrC is not absorbing at this wavelength.

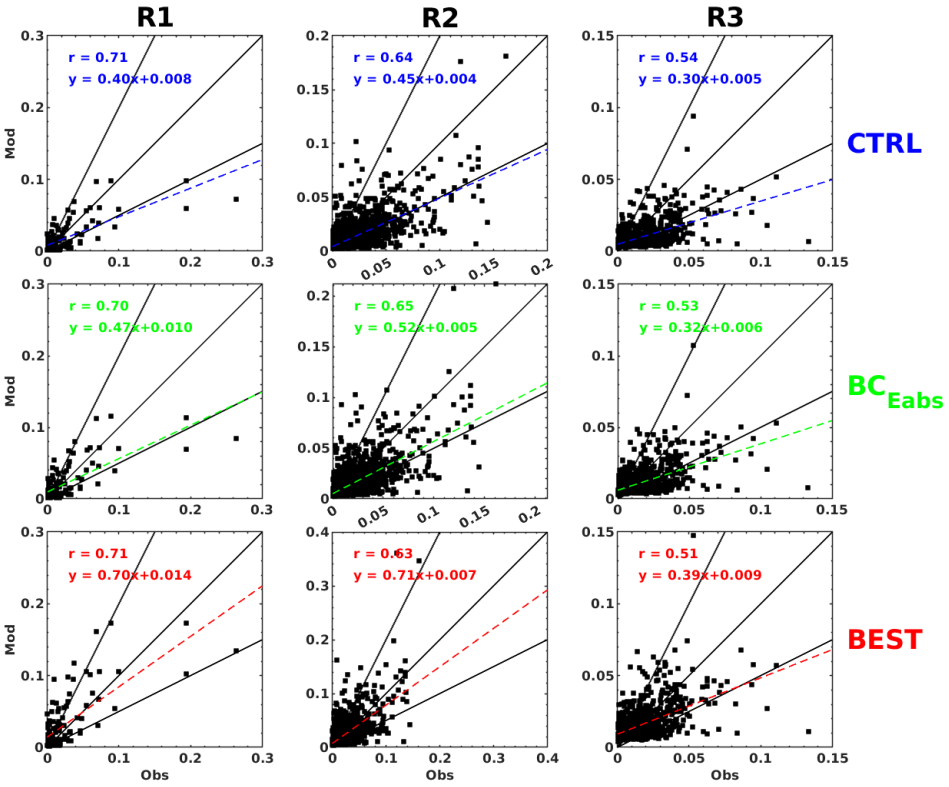

Figure 9. Scatter plots of observed and modelled daily absorption aerosol optical depth (AAOD) at 440 nm, for the CTRL, BC_{Eabs}, and BEST simulations at AERONET sites in regions R1, R2, and R3. The lines 1:1, 2:1, and best least-squares linear fit shown for reference.

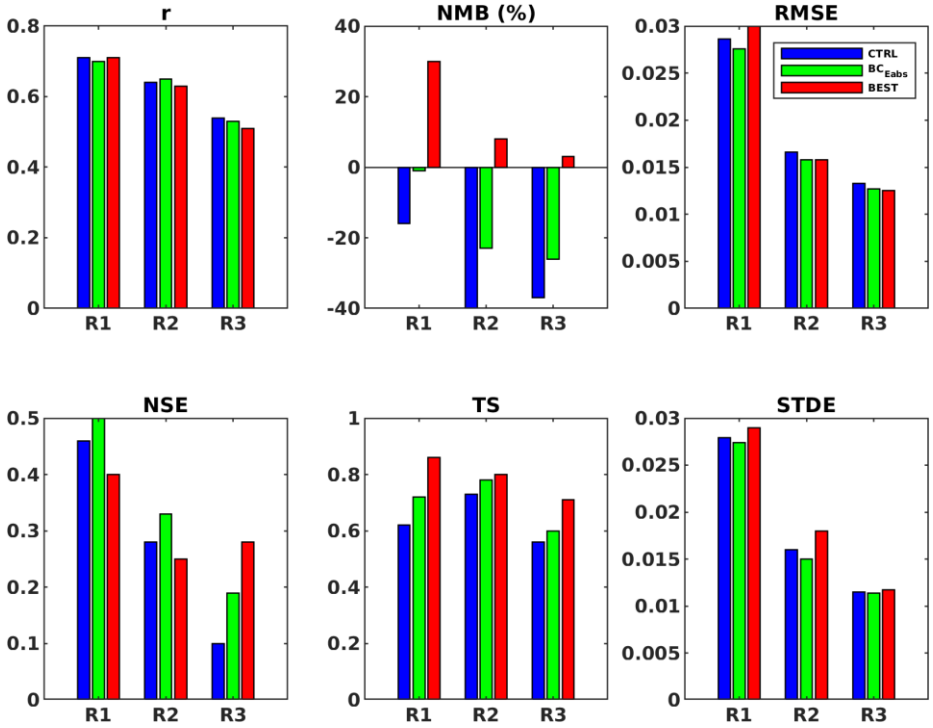

Figure 10. Statistical summary of the comparison of observed and modelled daily absorption aerosol optical depth (AAOD) at 440 nm, for the CTRL, BC_{Eabs}, and BEST simulations, at AERONET sites in regions R1, R2, and R3.

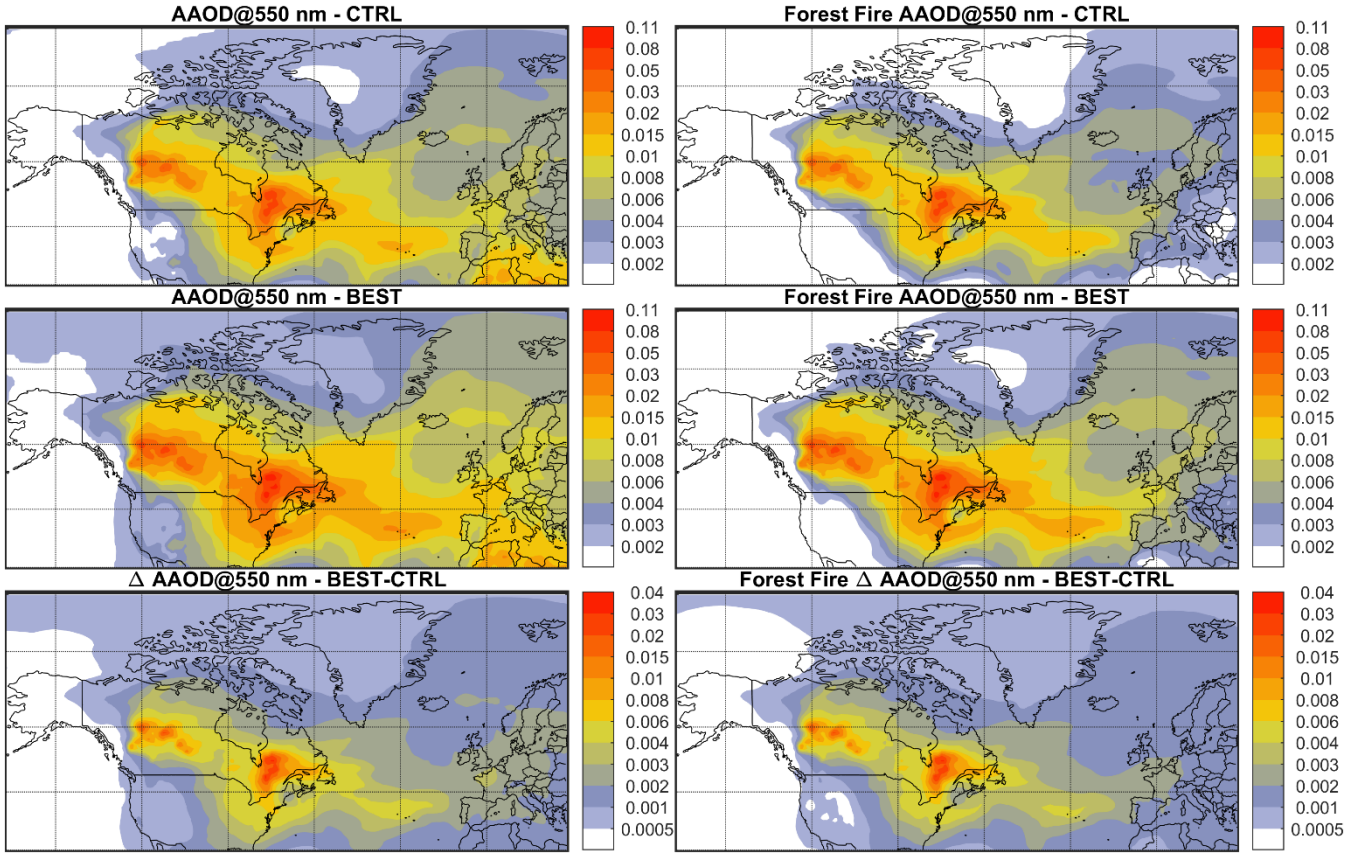

Figure 11. Mean total (left panels) and biomass burning (BB, right panels) absorption aerosol optical depth (AAOD) at 550 for June 2023, calculated by the CTRL (upper panels) and BEST (middle panels) models, and their difference (lower panels).

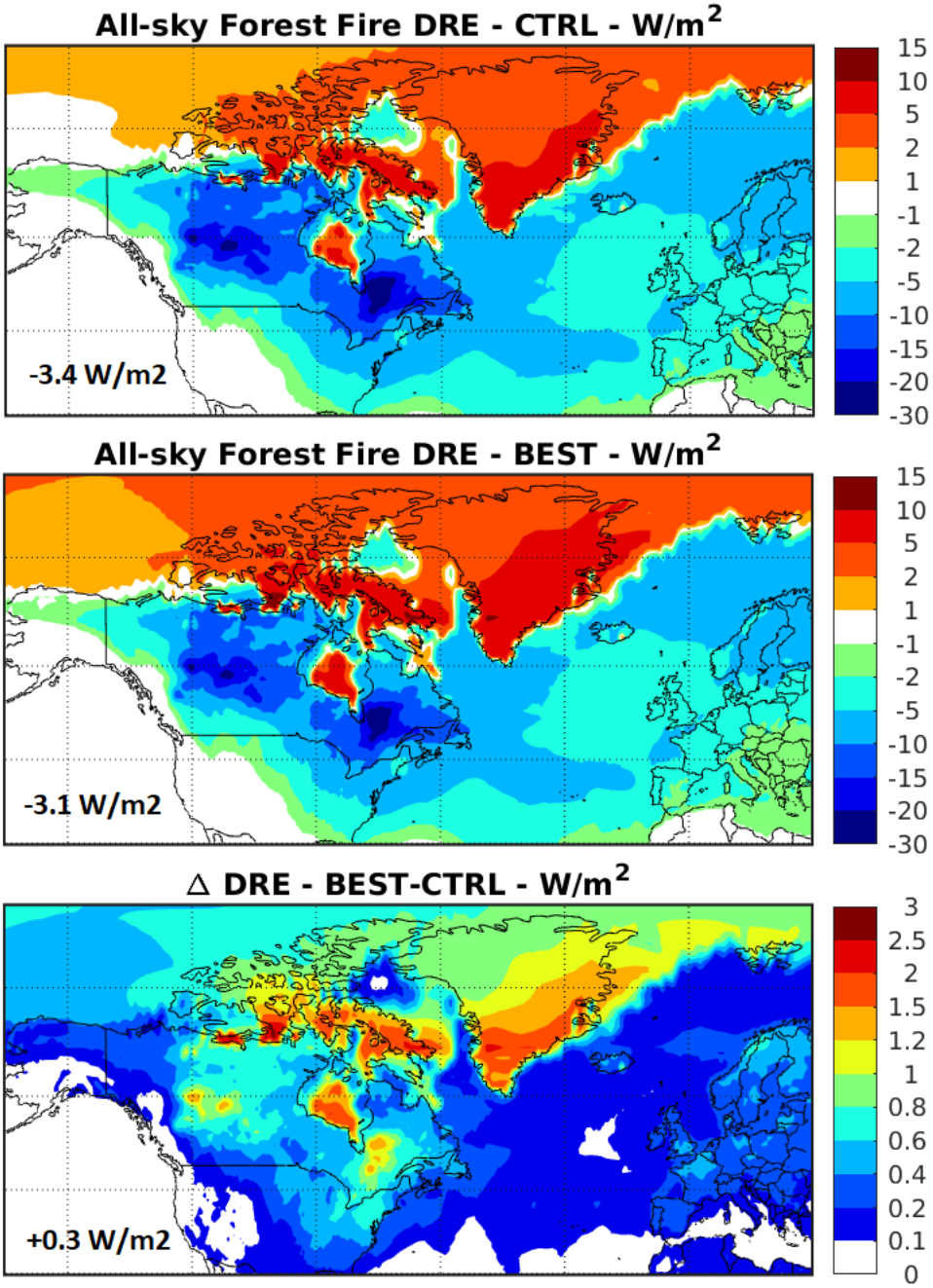

Figure 12. Mean all-sky DRE of biomass burning aerosols at top of the atmosphere (TOA) for June 2023, calculated by the CTRL (upper panel) and BEST (middle panel) models, and their difference (lower panel).

Journal of Geophysical Research

Supporting Information for

Modelling the black and brown carbon absorption and their radiative impact: the June 2023 intense Candian boreal wildfires case study

Paolo Tuccella[1,2], Ludovico Di Antonio[3,4], Andrea Di Muzio[1], Valentina Colaiuda[5], Laurent Menut6, Giovanni Pitari[1], Edoardo Raparelli[1,2]

[1]Departement of Physical and Chemical Sciences, University of L'Aquila, 67010 L'Aquila, Italy.

[2]Center of Excellence in Telesensing of Environment and Model Prediction of Severe Events (CETEMPS), University of L'Aquila, Italy.

[3]Univ. Paris Est Creteil, Université Paris Cité, CNRS, LISA, F-94010 Créteil, France.

[4]Laboratoire, Atmosphères, Observations Spatiales (LATMOS)/IPSL, Sorbonne Université, UVSQ, CNRS, Paris, France

[5]Abruzzo Region Civil Protection Agency, L'Aquila, Italy.

[6]LMD/IPSL, École Polytechnique, Institut Polytechnique de Paris, ENS, PSL Research University, Sorbonne Université, CNRS, Palaiseau, France

S.1 Statistical indices

The first index used is the Pearson correlation coefficient:

$$r = \frac{\sum_{i=1}^{n}(M_i-\bar{M})(O_i-\bar{O})}{\sqrt{\sum_{i=1}^{n}(M_i-\bar{M})^2(O_i-\bar{O})^2}} \qquad (6)$$

where M_i and O_i are the i-th modelled and observed value, respectively. $\bar{M}$ and $\bar{O}$ represent the mean of simulated and measured value, respectively. n is the total number of observations. In our evaluation, we also considered the Normalized Mean Bias:

$$NMB = \sum_{i=1}^{n}\frac{M_i-O_i}{O_i} \qquad (7)$$

In addition, we also employed the Root Mean Square Error:

$$RMSE = \sqrt{\frac{1}{n}\sum_{i=1}^{n}(M_i - O_i)^2} \qquad (8)$$

Nash-Sutcliffe Efficiency (NSE) is another metrics that we adopted to evaluate how well WRF-CHIMERE predicts the observations:

$$NSE = 1 - \frac{\sum_{i=1}^{n}(M_i-O_i)^2}{\sum_{i=1}^{n}(O_i-\bar{O})^2} \qquad (9)$$

NSE=1 indicates perfect correspondence between model and observations; NSE=0 indicates that model predictions are as accurate as the mean of the observed data; NSE<0 represents model predictions that are worse than using the mean of the observed data.

We also calculated the Taylor score (TS):

$$TS = \frac{4(1+r)}{\left(\frac{\sigma_o}{\sigma_M}+\frac{\sigma_M}{\sigma_o}\right)^2 (1+R_o)} \qquad (10)$$

where σ_M and σ_o are the standard deviation of modelled and observed value, respectively. R0 is the maximum obtainable correlation that we fixed at 1. The lower limit of TS is zero, larger values indicate higher model accuracy. The last metrics employed was the Standard Deviation Error (STDE):

$$STDE = \sqrt{\frac{1}{n}\sum_{i=1}^{n}(M_i - O_i)^2 - MB^2} \qquad (11)$$

where MB is the mean bias defined as

$$MB = \frac{1}{n}\sum_{i=1}^{n}(M_i - O_i)$$

S.2 DRE calculation

DRE has been calculated for a beam of solar light impinging an aerosol layer, with the following relationship:

$$DRE = F_0(1 - F_c)T_a^2\left[\left(r + \frac{t^2 R_s}{1 - rR_s}\right) - R_s\right]$$

where F_0 is the incident solar flux, F_c is the cloud fraction, T_a the atmospheric transmittance, r is the fraction of radiation reflected upward by aerosol layer, t is the fraction of radiation incident on the layer that is transmitted downward, and R_s is the surface albedo.

F_0 has been evaluated in each grid point for the analysed period, T_a was set 0.75, F_c and R_s were taken from WRF simulations. r and t were calculated as follows:

$$r = (1 - e^{-\tau})\omega\beta$$

$$t = e^{-\tau} + \omega(1 - \beta)(1 - e^{-\tau})$$

where τ is the AOD, ω the SSA, and β the upscatter fraction (the fraction of light that is scattered by a particle into the upward hemisphere). These parameters are optical averages, obtained averaging τ, ω, and β over a typical solar spectrum.

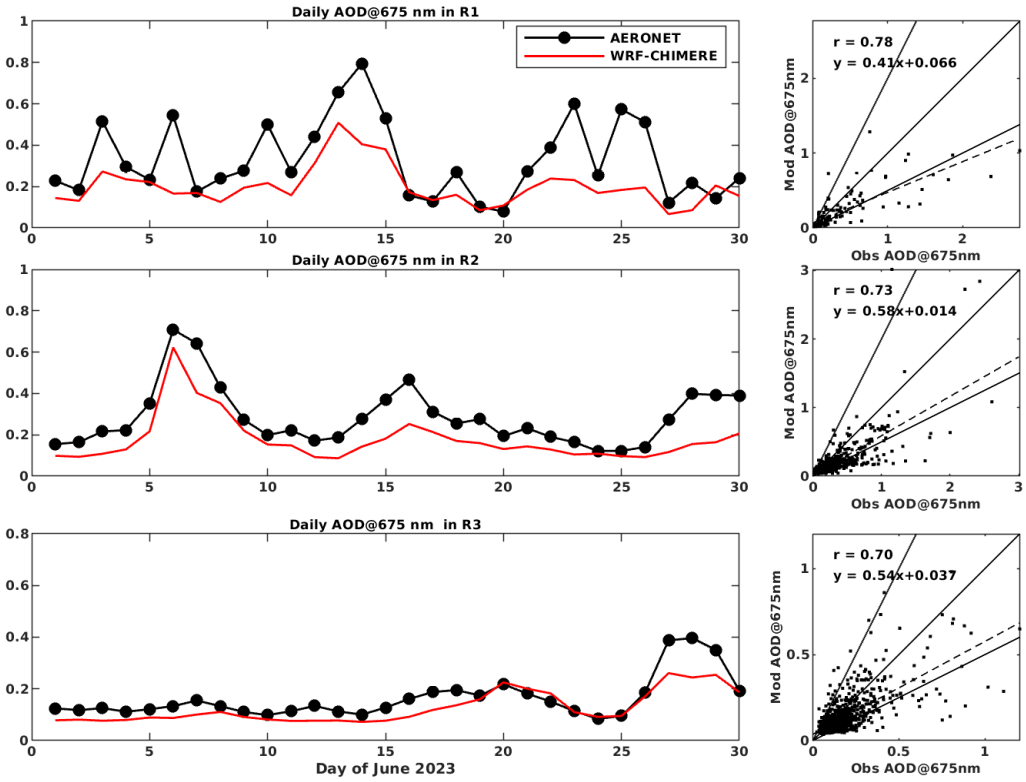

Figure S1: Comparison of modelled and observed AOD at 675 nm at AERONET sites. The left panels show the predicted and measured daily time series of AOD, averaged across all stations in regions R1, R2, and R3. The right panels present the scatter plots of observed versus predicted daily AOD in R1, R2, and R3. The lines 1:1, 2:1, and best least-squares linear fit shown for reference.

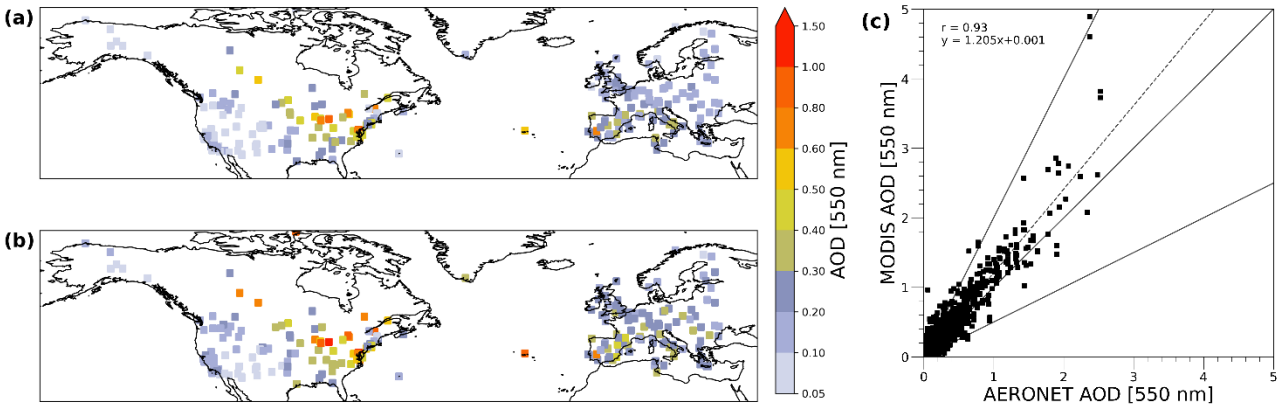

Figure S2: Comparison of AOD at 550 nm retrieved by MODIS with that measured at AERONET sites. a) June 2023 monthly average of AOD at AERONET sun photometers, b) June 2023 monthly average of AOD measured by MODIS at AERONET stations, c) scatter plot of MODIS AOD versus AERONET measurements. AERONET AOD at 550 nm have been obtained using the Angstrom exponent calculated between the AOD at 440 and 675 nm.

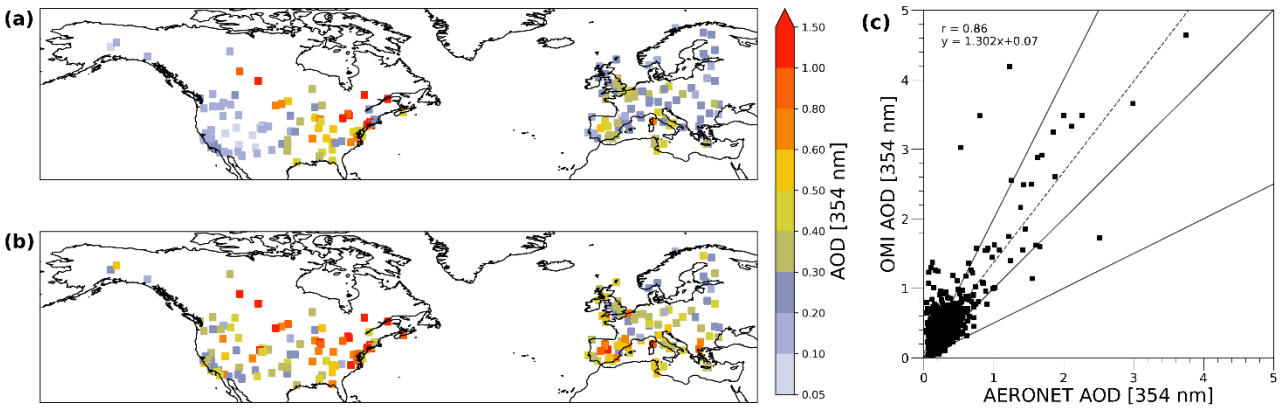

71

72 **Figure S3: As in Figure S2, but for AOD at 354 nm measured by OMI.**

73

74

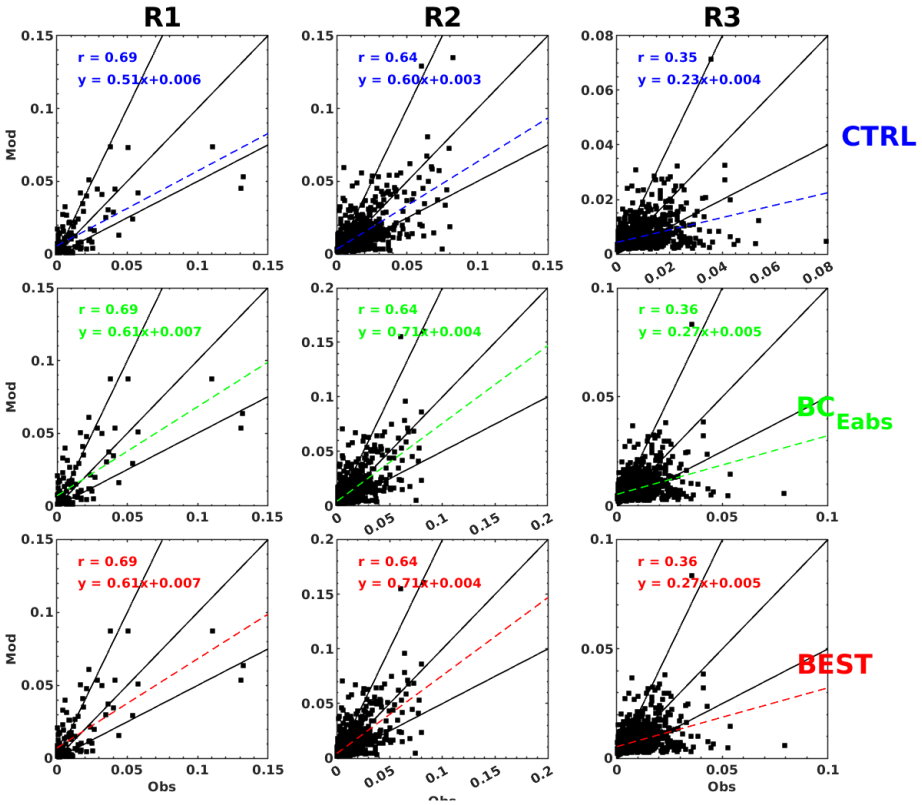

75

76 **Figure S4. Scatter plots of observed and modelled daily AAOD at 675 nm, for the CTRL, BC_{Eabs}, and**
77 **BEST simulations at AERONET sites in regions R1, R2, and R3. The lines 1:1, 2:1, and best least-**
78 **squares linear fit shown for reference.**

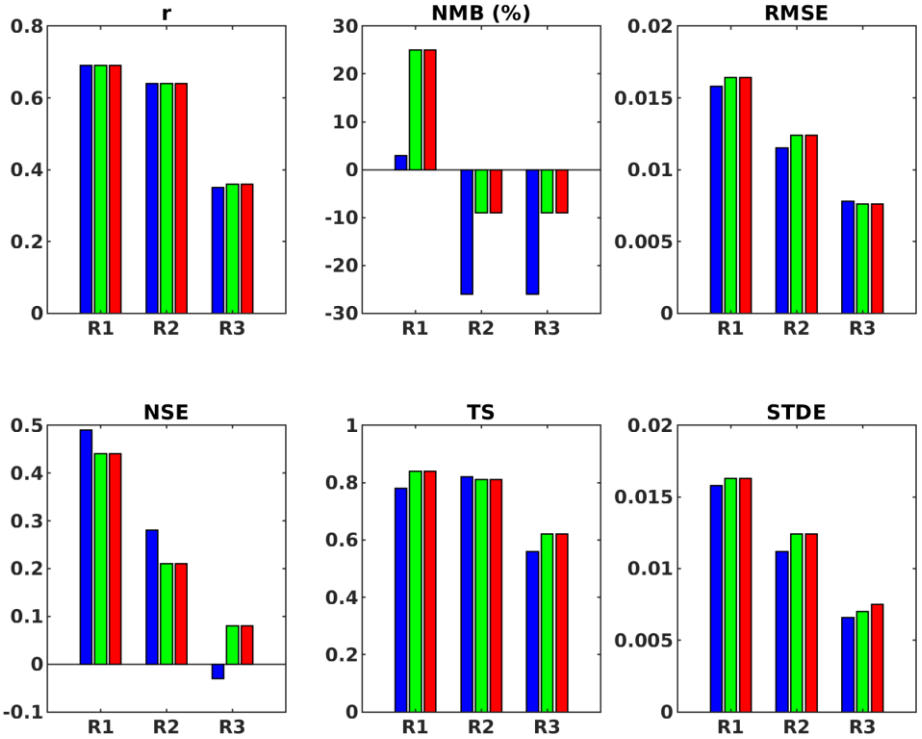

79

80 **Figure S5. Statistical summary of the comparison of observed and modelled daily AAOD at 440 nm,**
81 **for the CTRL, BC_{Eabs}, and BEST simulations, at AERONET sites in regions R1, R2, and R3.**

82

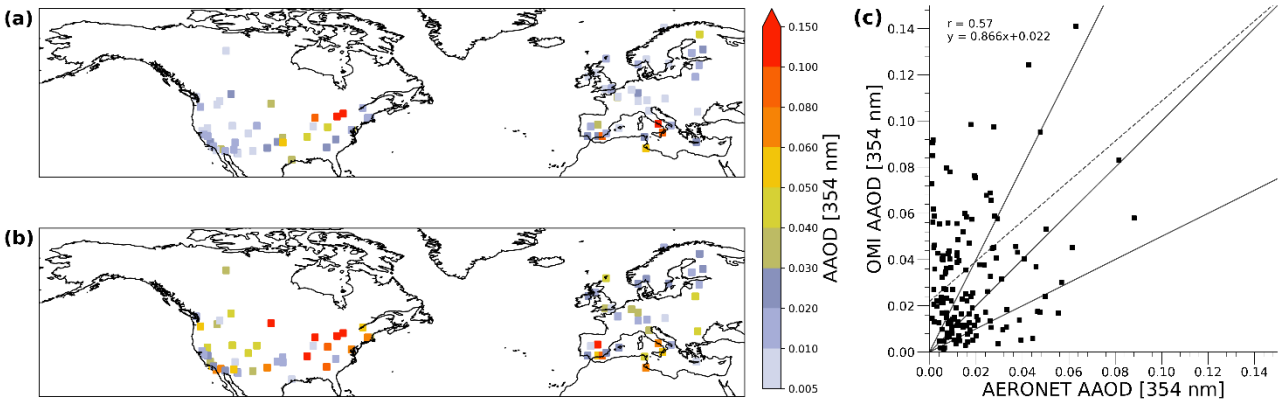

Figure S6: As in Figure S2, but for AAOD at 354 nm measured by OMI.

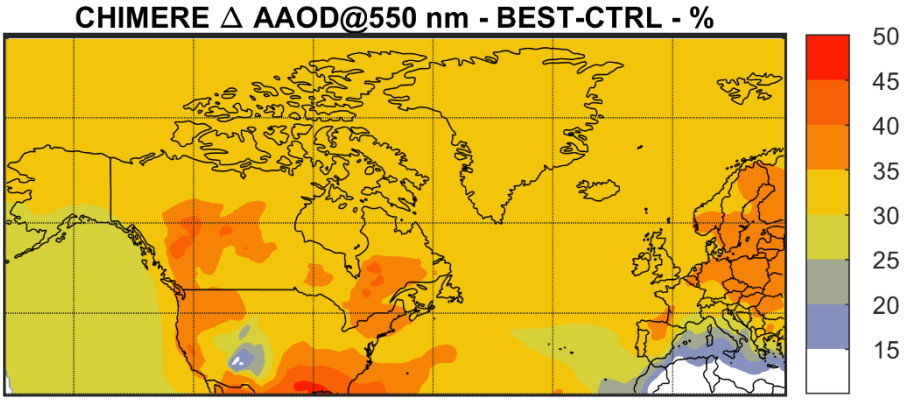

Figure S7: Relative AAOD at 550 nm changes between BEST and CTRL simulations.

Table S1. Statistical comparison of the predicted and observed AOD with AERONET stations at 675 nm.

Database	r	NMB (%)	RMSE	NSE	TS	STDE
AERONET[1,2]	0.75	-27	0.15	0.52	0.80	0.14
AERONET-R1[1]	0.77	-40	0.34	0.45	0.62	0.31
AERONET-R2[1]	0.76	-32	0.22	0.45	0.81	0.20
AERONET-R3[1]	0.69	-22	0.12	0.38	0.80	0.38

[1]The comparison is done with daily data
[2]This comparison is done with all AERONET data